OPTICAL CHARACTERISTICS OF GRAPHENE OXIDE FILM AND ITS APPLICATION IN PLANAR WAVEGUIDE DEVICES

LIM WENG HONG

FACULTY OF SCIENCE
UNIVERSITY OF MALAYA
KUALA LUMPUR

2016

OPTICAL CHARACTERISTICS OF GRAPHENE OXIDE FILM AND ITS APPLICATION IN PLANAR WAVEGUIDE DEVICES

LIM WENG HONG

THESIS SUBMITTED IN FULFILMENT OF THE REQUIREMENTS FOR THE DEGREE OF DOCTOR OF PHILOSOPHY

FACULTY OF SCIENCE
UNIVERSITY OF MALAYA
KUALA LUMPUR

2016

UNIVERSITY OF MALAYA

ORIGINAL LITERARY WORK DECLARATION

Name of Candidate: Lim Weng Hong

Registration/Matric No: SHC110016

Name of Degree: Doctor of Philosophy

Title of Thesis: Optical Characteristics of Graphene Oxide Film and Its Application in Planar Waveguide Devices

Field of Study:

I do solemnly and sincerely declare that:

(1) I am the sole author/writer of this Work;
(2) This Work is original;
(3) Any use of any work in which copyright exists was done by way of fair dealing and for permitted purposes and any excerpt or extract from, or reference to or reproduction of any copyright work has been disclosed expressly and sufficiently and the title of the Work and its authorship have been acknowledged in this Work;
(4) I do not have any actual knowledge nor do I ought reasonably to know that the making of this work constitutes an infringement of any copyright work;
(5) I hereby assign all and every rights in the copyright to this Work to the University of Malaya ("UM"), who henceforth shall be owner of the copyright in this Work and that any reproduction or use in any form or by any means whatsoever is prohibited without the written consent of UM having been first had and obtained;
(6) I am fully aware that if in the course of making this Work I have infringed any copyright whether intentionally or otherwise, I may be subject to legal action or any other action as may be determined by UM.

Candidate's Signature Date:

Subscribed and solemnly declared before,

Witness's Signature Date:

Name:

Designation:

ABSTRACT

Investigation of the optical characteristics of Graphene Oxide (GO) film was carried out. The GO film was fabricated by drop-casting of GO solution onto a planar substrate. The GO solution was prepared using improved Hummer's method. The optical conductivity of GO film for TE-polarised light (perpendicular to the stacking axis of GO layers) is in the magnitude of ~10^3 Sm^{-1}, which results in very high optical absorption. On the other hand, TM-polarised light will encounter relatively smaller absorption due to a much lower optical conductivity. It was also observed that the conductivity of the GO film is affected by the amount of water molecule present in the film. Water molecules are able to permeate in and out of the GO film freely due to the film natural properties. The permeated water molecules readily interact with the functional groups of each individual GO layer and this interaction reduces the film conductivity by further widening its bandgap. This process was reversible when the water content in the film was reduced. In addition, photothermal reduction through optical phonon relaxation of GO film using near infrared light source was studied. A numerical model of wave propagation in GO film was then developed followed by experimental verification of the model.

The GO film was then coated onto a planar optical waveguide. Strong polarisation effect was observed due to the large anisotropy complex dielectric function of GO film. The GO film functionalized waveguide polariser showed a broad band response over the visible and near infrared wavelength range with a maximum polarisation extinction ratio of more than 40 dB in the 1550 nm optical fibre communication window. The response of GO film to changing water content has also been applied in optical water detection and humidity sensing. Finally, by exploring the reversible photothermal reduction characteristics of GO film, an all-optical GO-based waveguide modulator with a modulation depth of 72% and response time of <100 μs was demonstrated.

ABSTRAK

Penyiasatan atas ciri-ciri optik filem Graphene Oksida (GO) telah dijalankan. Filem GO adalah dibuat dengan cara “drop-casting” dari penyelesaian GO ke atas substrat satah. Penyelesaian GO ini adalah disediakan dengan menggunakan kaedah Hummer. Kekonduksian optik filem GO untuk cahaya yang berpolarisasi TE (berserenjang dengan paksi menyusun lapisan GO) adalah dalam magnitud ~ 10^3 Sm^{-1}. Ini mengakibatkan penyerapan cahaya TE yang kuat. Sebaliknya, cahaya berpolarisasi TM akan mengalami penyerapan yang lebih kecil berbanding dengan cahaya berpolarisasi TE atas sebab kekonduksian optik yang lebih rendah. Selain itu turut diperhatikan, kekonduksian filem GO adalah dipengaruhi oleh jumlah kandungan molekul air yang hadir dalam filem itu. Molekul air dapat meresap ke dalam dan keluar dari filem GO dengan bebas atas sebab sifat semula jadi filem. Air yang diresap akan bertindak balas dengan kumpulan berfungsi masing-masing yang hadir di setiap lapisan GO dan tindak balas penurunan ini akan mengurangkan kekonduksian filem. Prosess ini boleh berbalik apabila kandungan air dalam filem dikurangkan. Selain itu, penurunan foto-haba memalui kelonggaran fonon optik bagi filem GO dengan menggunakan sumber cahaya inframerah turut dipelajari. Satu model berangka perambatan gelombang optik dalam filem GO telah dibangunkan dan disahkan melalui penyelidikan.

Filem GO kemudian disalut ke atas pandu gelombang optik yang bersatah. Kesan polarisasi cahaya yang kuat dapat diperhatikan atas sebab ciri ketidaksamaan dalam dielektrik filem GO. Penyaring polarisasi yang dicipta melalui cara ini mempunyai rangkaian yang luas dalam panjang gelombang inframerah dan cahaya yang boleh dilihat. Nisbah penyaring yang lebih daripada 40 dB dapat dicapai dalam panjang gelombang komunikasi 1550 nm. Ciri-ciri tindak balas filem GO keatas kandungan air juga telah digunakan dalam pengesanan air dan kelembapan diatas gentian optic bersatah. Akhir sekali, dengan penerokaan atas ciri-ciri berbalik pengurangan foto-haba filem GO, semua

optik pandu gelombang modulasi berasaskan GO telah ditunjukkan dengan mempunyai kedalaman modulasi 72% dan tempoh tindak balas <100 μs.

ACKNOWLEDGEMENTS

This dissertation would not have been possible without the help and support from a great number of people. First, I would like to express my gratitude to my advisor Professor Dr. Harith Ahmad for providing me the opportunity of conducting research within the Photonics Research Centre University of Malaya. My special gratitude should be directed to my Co-supervisor Dr. Chong Wuyi for supervising and guiding in my work. I also like to thank other lab members such as Professor Dr. Richard De La Rue, Dr. Pua Chang Hong, Dr. Richard Penny and Mr. Yup Yuen Kiat for their precious discussion and idea; Dr. Huang Nay Ming for material preparation; Mr. Chong Yew Ken, Mr. Lai Choon Kong, and Mr. Lee Say Hoe for their technical support. During my study, I would like to thank MyBrain15 for my scholarship and financial support. Last but not least my parents for their unconditional support and understanding.

TABLE OF CONTENTS

Abstract iii

Abstrak iv

Acknowledgements vi

Table of Contents vii

List of Figures xi

List of Tables xvi

List of Symbols and Abbreviations xvii

CHAPTER 1: INTRODUCTION 1

1.1 The Birth of Planar Lightwave Circuits 1

1.2 Planar Lightwave Circuits as Optical Waveguides 3

1.2.1 Planar Lightwave Circuits Technology 4

1.2.2 Polymer Based Waveguides 5

1.3 Graphene Photonics 6

1.4 Thesis Objective and Outline 8

CHAPTER 2: WAVEGUIDE THEORY AND SIMULATION 12

2.1 Waveguide Theory 12

2.1.1 Formation of Guided Modes in A Waveguide 12

2.1.2 Analytical and Numerical Approached 24

2.2 Optical Loss in A Medium 25

2.3 Simulation Method and Softwave 27

2.3.1 Finite Element Method 28

2.3.2 Finite Difference Method 34

CHAPTER 3: SAMPLE FABRICATION AND CHARACTERIZATION 38

3.1 Fabrication Environment 38

3.2 Choice of Waveguide, Substrate, and Overclad Materials 39

3.3 Substrate Preparation and Cleaning 45

3.4 Photolithography 46

3.4.1 Spin Coating 47

3.4.2 Control of SU-8 Thickness 48

3.4.3 Soft Bake 49

3.4.4 UV Expose and Patterning 50

3.4.5 Post Exposure Bake and Developing 51

3.5 Overcladding Coating 52

3.6 Hard Curing 53

3.7 Dicing and Polishing 53

3.8 SU-8 Film Characterization 54

3.9 Fibre Coupling and Optimization 59

3.10 Optical Characterization 62

3.11 Summary 65

CHAPTER 4: GRAPHENE, GRAPHENE OXIDE AND GRAPHENE OXIDE FILM 69

4.1 Introduction to Graphene 69

4.1.1 Form Graphene Oxide to Graphene Oxide Paper 71

4.1.2 Graphene Oxide Preparation 74

4.1.3 Characterization of Graphene Oxide and Graphene Oxide film 75

4.1.3.1 Atomic Force Microscopy 75

4.1.3.2 UV-Visible-Near Infrared Spectroscopy 76

4.1.3.3 Raman Spectroscopy 77

4.1.3.4 Fourier Transform Infrared Spectroscopy 79
4.1.3.5 X-Ray Diffraction Measurement 80
4.2 Other Unique Properties of Graphene Oxide Film 82
4.2.1 Anisotropic Dielectric Function 82
4.2.2 Graphene Oxide Bandgap and Conductivity 83
4.2.3 Hydrophilic and Water Permeation in Graphene Oxide Film 84
4.2.4 Reversible Phonon Reduction of Graphene Oxide 84
4.3 Drop-Casting of Graphene Oxide 85
4.3.1 Drying Mechanism and Creation of Wrinkle 86
4.3.2 Drop-Casting and Surface Morphology 87

CHAPTER 5: GRAPHENE OXIDE WAVEGUIDES POLARISER: MOTIVATION 98

5.1 Graphene Oxide Waveguide Polariser 100
5.1.1 Fabrication and Optical Characterization Setup 100
5.1.2 Results and Discussion 101
5.1.3 Simulation Model 105
5.1.3.1 Simulation Model Setup 105
5.1.3.2 Fitting of Simulation Model 109
5.1.3.3 Effect of Waveguide Dimension 115
5.2 Conclusion and Future Work 118

CHAPTER 6: GRAPHENE OXIDE BASED OPTICAL HUMIDITY AND WATER SENSOR: MOTIVATION 121

6.1 Anomalous Unimpeded Water Permeation Through Graphene Oxide Membrane 122
6.2 Water Dependent Dielectric Properties of Graphene Oxide 125

6.3 Graphene Oxide Based Optical Water Sensor: Motivation 126

6.3.1 Water Sensor Design and Experimental Setup 127

6.3.2 Performance of Proposed Water Sensors 129

6.3.3 Conclusion…… 133

6.4 Graphene Oxide Based Optical Humidity Sensor: Motivation 134

6.4.1 Humidity Sensor Design and Experimental Setup 135

6.4.2 Performance of Optical Humidity Sensors 136

6.4.3 Aging in Graphene Oxide 142

6.4.4 Conclusion…… 146

CHAPTER 7: GRAPHENE OXIDE BASED OPTICAL SWITCH: MOTIVATION … 150

7.1 Fabrication and Optical Characterization Setup 151

7.2 Performance of Proposed Optical Switch 153

7.3 Conclusion… 161

CHAPTER 8: THESIS CONCLUSION AND FUTURE WORK … 164

List of Publications and Papers Presented 168

Appendix A: Laser Direct Writing 169

LIST OF FIGURES

Figure 1.1: Types of waveguides structure with light propagation along z-axis 4

Figure 2.1: Geometrical structure of a slab waveguide..... 13

Figure 2.2: Light rays (with an angle ϕ) and their corresponding phase fronts (dotted line) in a slab waveguide with core size 2a 15

Figure 2.3: Refractive index distribution of the inhomogeneous slab optical waveguide 29

Figure 3.1: Transmission spectrum of SU–8 after cure 41

Figure 3.2: Screenshot of refractive index measurement of SU-8 at 1550 nm on CR-39 using Sairon SPA 4000 prism coupler 41

Figure 3.3: Screenshot of refractive index measurement of CR-39 using Sairon SPA 4000 prism coupler..... 43

Figure 3.4: Transmission spectrum of NOA 65 UV resin 45

Figure 3.5: Summary of waveguide fabrication process flow 46

Figure 3.6: SU-8 coating thickness with respect to amount of dilutor (Cyclopentanone) added 49

Figure 3.7: Microscope images of waveguide end facet after a) dicing, polished using b) 15 μm, c) 9 μm, and d) 0.3 μm polishing films 54

Figure 3.8: Operating principle of prism coupler..... 56

Figure 3.9: Screenshot of prism coupling spectrum measurement using Sairon SPA 4000 prism coupler and its corresponding refractive index of SU-8 - BCB dual layers on silicon substrate measured at 1550 nm 57

Figure 3.10: Screenshot of propagation loss measurement (blue line) of SU-8 – BCB dual layers film on silicon substrate 58

Figure 3.11: Waveguide optical alignment system..... 63

Figure 3.12: a) The top view of fibre to waveguide alignment setup using a red light source. The output of waveguide with b) red light source projected on to a white screen (for 1x4 splitter) and c) 1550 nm light source recorded with IR camera (for 1x8 splitter) 63

Figure 4.1: Microscope image of different number (ranging from 1 drop on the left to 3 drop) of drop-casted GO 72

Figure 4.2: FESEM image of cut edge of GOP 73

Figure 4.3: Summary of GOF fabrication from Graphite flakes 75

Figure 4.4: AFM image of spin-coated GO solution 76

Figure 4.5: UVVIS absorbance spectrum of GO Solution 77

Figure 4.6: Raman spectrum of GOF 78

Figure 4.7: Relation of ID/IG and bandgap, where reduction level in x-axis is just an arbitrary unit of time 78

Figure 4.8: FTIR-ATR absorption spectrum of GOF 79

Figure 4.9: XRD spectrum of a thick GOF 81

Figure 4.10: Model of the GOF cross section depicting water molecules intercalated between two Graphene Oxide layers 81

Figure 4.11: Schematic diagrams of a) ellipsoid particle solvent drying process, b) the solvent evaporating process, and c) the distribution of the ellipsoid lamellar cluster within the droplet during evaporation 87

Figure 4.12: Image capture of GO solution drying 87

Figure 4.13: Image capture of drop-casted GO with various drop-casted volume 88

Figure 4.14: Coating diameter against drop-casted volume 89

Figure 4.15: Image of drop-casted GOF with various GO concentrations (ranging from left 0.5, 0.75, 1, 1.5, 2, 3, 4, 6, 8, and 12 μg/μl) 90

Figure 4.16: Height achieved for different concentration per drop 90

Figure 4.17: Surface mapping of GOF coated on waveguides 90

Figure 4.18: Height profile across the diameter of 4 selected concentrations (12, 8, 4, and 1.5 μg/μl) 91

Figure 4.19: Height profile of 3 selected concentrations (8.5, 7.2, and 6 μg/μl) diluted using ethanol from 12 μg/μl GO solution 92

Figure 4.20: Height gain for different number of drops 93

Figure 5.1: Image capture of GOWP chip 100

Figure 5.2: Characterization setup for GOWP. a) Polarimeter measurement and b) insertion loss measurement 101

Figure 5.3: Polar plot of GOWP 102

Figure 5.4: Top view of GOWP with TM- and TE-polarised light propagating through the waveguide 103

Figure 5.5: Insertion loss of TE- and TM-polarised light of GOWP coated with different film thickness at 1550 nm. The solid line is the simulation results 104

Figure 5.6: Broadband response of GOWP. The solid line is the simulation fitting result 104

Figure 5.7: FESEM micrograph of GOWP. a) Top view at the middle of GOWP, b) top view at the edge of GOF, c) higher magnification on the channel side wall, an air viod was observed, and d) GOF internal surface morphology that was attached to the waveguide surface 106

Figure 5.8: Simulation model of cross-section of the GOWP 107

Figure 5.9: Effect of doping (μ) on conductivity of Graphene at infrared frequency... 108

Figure 5.10: Simulation model of GOWP for both TE- and TM-mode propagating loss and their different (extinction ratio) 110

Figure 5.11: Simulation model of Electric field component distribution of a) both TE– and TM–mode across the channel axis and b) Ex plot of TE-mode, c) Ey plot of TM - mode at the channel cross section for GOF of 2 μm 111

Figure 5.12: Effect of conductivity of GOF on TE–mode absorption 112

Figure 5.13: Effect of refractive index of GOF on TE–mode absorption 113

Figure 5.14: Simulation and experimental result of extinction ratio 114

Figure 5.15: Simulation of wavelength dependent imaginary refractive index of the GOWP for both TE- and TM-mode 115

Figure 5.16: Configuration of light source amplification by EDFA 117

Figure 5.17: EDFA amplification of TLS signal 117

Figure 6.1: Model of two GO sheet 124

Figure 6.2: Transport mechanism of water molecules between two GO sheets. a) Top view of optimised atomic structure of ice monolayer between the layers of graphite. Oxygen, hydrogen, and carbon atoms are denoted by red, grey and green colour. The ice layer can slide along x-, y- and m-direction. b, c) Side view of ice mono- and bilayers along y (left) and along x (right) direction 125

Figure 6.3: Schematic diagram of GO-coated waveguide sensor and the experiment setup for water detection..... 129

Figure 6.4: The response (change in transmission power) of the proposed sensor to a drop of water..... 130

Figure 6.5: Performance of water sensor toward water-alcohol mixture a) above 30% and b) selected mixture 132

Figure 6.6: The change in drying time measured by the proposed sensor toward various water-alcohol mixture solution with different water content was applied..... 133

Figure 6.7: Schematic diagram of the proposed humidity sensor for fast response measurement 136

Figure 6.8: Schematic diagram of the proposed humidity sensor for humidity measurement 136

Figure 6.9: a) Change in transmitted power over time when humid air was introduced onto the GOF, from the 6^{th} second to 9^{th} second, and corresponding optical micrographs of the GOF at the marked times: b) before humid air was introduced; c) the beginning of the flow of humid air at the 6^{th} second; d) the end of the humid air flow; e) first drying stage of the GOF with water droplets on substrate; f) second drying stage, where water droplets on substrate and GOF has evaporated; and g) final stage of drying where water content in the GOF recedes rapidly from the edge to the centre..... 138

Figure 6.10: Changes in the normalized transmitted power when humid air (100% RH) was introduced onto the proposed sensor periodically at a) 5.0 seconds intervals and b) 0.67 seconds intervals 140

Figure 6.11: Linear response to humidity in the range of 60% RH to 100% RH 141

Figure 6.12: The aging effect of the proposed sensor..... 143

Figure 6.13: FTIR characterization of GOF at different time (hour)..... 145

Figure 6.14: FTIR ratio of peak intensity 1735 to 1650 of GOF at various time 145

Figure 7.1: Experimental setup for optical modulation measurement..... 152

Figure 7.2: Broadband attenuation of the signal-source power by the GO optical switch at 1550 nm with different 1480 nm CW control-source power 155

Figure 7.3: Broadband attenuation of 1550 nm broadband signal-source power by the GO optical switch with different 1480 nm CW control-source power 155

Figure 7.4: Modulation depth of the optical switch measured using a photodiode at 3 different modulation frequencies with fixed pulse duration of 100 μs. 156

Figure 7.5: Modulation efficiency of the switch at various pulse durations, modulated at 50 Hz 157

Figure 7.6: Modulation efficiency of the proposed switch for modulation frequency in the range from 0.5 kHz to 5 kHz with fixed 50% duty cycle 158

Figure 7.7: Modulation efficiency and GOF temperature at various control laser power 159

Figure 7.8: Modulation efficiency of the GO switch with 1480 nm and 980 nm control source 161

Figure 8.1: Optical NAND gate design based on GO switch principle 167

Figure A.1: a) Photo and b) schematic diagram of all-fibre laser direct writing system. 171

Figure A.2: Specific absorbance of SU-8 173

Figure A.3: Real time CCD image of the direct writing system 174

Figure A.4: Some example of direct written waveguide 175

Figure A.5: a) Photolithographically waveguide and b) direct written waveguides. Jagged occurred in direct written waveguide 176

LIST OF TABLES

Table 3.1: Insertion of SU-8 waveguide to SMF and UHNA4 fibre at 1550 nm 61

Table 4.1: Summary of vibrational modes of GO in FTIR absorption 80

LIST OF SYMBOLS AND ABBREVIATIONS

AFM	Atomic Force Microscopy
AWG	Array Waveguide Grating
CVD	Chemical Vapour Deposition
DI	De-ionized Water
FBG	Fibre Bragg Grating
FDTD	Finite Difference Time Domain
FEM	Finite Element Method
FESEM	Field Emission Scanning Electron Microscopy
FTIR-ATR	Fourier Transform Infrared Spectroscopy - Attenuated Total Reflectance
FTTH	Fibre to the Home
GO	Graphene Oxide
GOF	Graphene Oxide Film
GOP	Graphene Oxide Paper
GOWP	Graphene Oxide Waveguide Polariser
H_2O_2	Hydrogen Peroxide
HCl	Hydrochloric Acid
IPA	Isopropanol Alcohol
$KMnO_4$	Potassium Permanganate
LD	Laser Diode
MFD	Mode Field Diameter
NA	Numerical Aperture
OPM	Optical Power Meter
OSA	Optical Spectrum Analyser

PC	Polarisation Controller
PD	Photo Diode
PEB	Post Exposure Bake
PIC	Photonic Integrated Circuits
PLC	Planar Lightwave Circuit
SLD	Superluminescent Laser Diode
SNR	Signal - to - Noise Ratio
TE	Transverse Electric
TIR	Total Internal Reflection
TM	Transverse Magnetic
UV-VIS-NIR	UV Visible Near Infrared Spectroscopy
WDM	Wavelength Division Multiplexing
XRD	X-ray Diffraction Measurement

CHAPTER 1: INTRODUCTION

1.1 The Birth of Planar Lightwave Circuits (PLCs)

In 2009, Charles K. Kao was awarded the Nobel Prize in Physics by The Royal Swedish Academy of Sciences for his influential contribution on the phenomena of light transmission in optical fibres used for communication. This award represented recognition of his contribution to fibre optic communication systems that have changed our everyday lives throughout the past 15 years, where information can be transferred around the world with just a few keyboard strokes [1]. By comparing with the traditional electric copper wire, the bandwidth of a single mode fibre is about 50 THz, which are 5000 times faster than copper wire. First few tens year after the born of fibre optic in 1966, fibre optic technologies were only used in the military and only until 1990s, fibre optic are applying in internet backbone between countries. The driven factor of this application is due to the creation of World Wide Web in 1989 by Tim Berners-Lee [2], an historical milestone of "Information Age", resulted in a hugely increasing amount of personal internet usage in daily life occurring at the beginning of this new millennium. As a means to satisfy the capacity demands, the concept of Fibre-To-The-Home (FTTH) became realistic whereby fibre optic was used in all levels. Many countries like Japan, North America, and Europe adopted FTTH technologies into their communication system, Japan alone in 2006 had more than 6 million FTTH subscribers online, and became the first country to connect more new FTTH customers than Digital-Subscriber-Line (DSL) customers [3]. In Malaysia, the FTTH project was launched on 2007 to provide FTTH broadband access by the second half of 2008 in Klang Valley and other major urban centres in Peninsula Malaysia as a preliminary step towards an ultimate digital home experience [4].

In order to support the fibre optic communication system, devices are necessary in order to manipulate and process light signals. Light manipulation in the 1980s was done by converting it into an electrical signal, electronically processed and finally conversion of the signal back into an optical signal for launch into the fibre optic system. This kind of conversion is not efficient in today's optical communication system because it causes slow down in the optical networking speed due to the relatively slow response time (when compared to the optical signal transmission light speed) of electronic devices, and furthermore an external electricity supply is needed for operation of electronic devices. Hence, research on multifunctional passive optical devices has become the focus for scientists around the world. However, with the exception of Fibre Bragg Grating (FBG, a narrow-band wavelength filter), not all functions necessary for the elimination of electrical conversion can be fabricated directly onto the fibre. Other functions that are equally important in fibre optic communication system, such as Splitters, Array Waveguides Gratings (AWGs), and wavelength combiners, can only be integrated in a planar platform (also known as a planar waveguide or Planar Lightwave Circuit (PLC)). Research and development necessary for planar waveguide devices has already been justified by the commercial deployment of optical passive splitters in FTTH telecommunication systems. It is believed that more planar waveguide devices will follow the success of optical splitters, especially in telecommunications, where researchers are focusing their efforts to reduce the footprint of planar waveguide devices and to integrate more functions onto a single chip, as well as to reduce the optical insertion loss and fabrication cost [3, 5]. It is worth noting that PLC developments have resulted in high component density on a single chip: such components do not only refer to optical components but also electronics components. Electronics functions can also be integrated into a PLC and function together with the optical components in a single chip. Examples of these components are waveguides, gratings, emitters (laser source), detectors

(photodiode), and splitters. Due to their great potential, PLCs are attractive within fields other than telecommunications, such as medical, military, and aerospace, and applications of PLCs are expected to grow wider in the future.

1.2 Planar Lightwave Circuits as Optical Waveguides

A PLC is a type of optical waveguide - a structure that is able to guide wave such as electromagnetic waves - that is fabricated on a flat substrate such as silica, silicon or any insulator. There are many types of optical material suitable for PLC fabrication, including silica on silicon, silica on silica, silicon on insulator, silicon oxynitrides, indium phosphide, lithium niobate, and polymer. PLC waveguides that uses silica on silica are attractive in the commercial market because this platform takes advantages of well-established semiconductor processing technology, low fabrication cost, low optical propagation loss in the optical Communication Band (C-band), and high coupling efficiency with conventional silica based optical fibres [6]. Silica wafers offer the advantages of high degree of planarity, good adhesion to silica deposition, no thermal mismatch between layers, and a relatively low cost due to their mass production [7].

Silica on silica refers to two or three layers of silica with different optical properties that are deposited on top of a silica substrate. These silica layers are responsible for the waveguide operation. The basic operation principle of a PLC waveguide is similar to that for optical fibre, in which light is guided in the silica layer that has a higher refractive index (usually referred to as core) than the surrounding silica layer (usually stated as cladding) by the mechanism of Total Internal Reflection (TIR). In order to fabricate silica layers that have different optical properties, dopants like phosphorous, boron, and germanium are added into each silica layer during the fabrication process. These dopants affect the atomic bonding of the silica layer and cause a change in

refractive index, glass transition temperature and other properties that play an important role in an optical waveguide.

In terms of waveguide profiles, the PLC waveguide is in planar form as indicated by it's name. The structure of the PLC waveguide core layer can generally be divided into 4 waveguide categories: slab, deep ridge, channel, and ridge waveguides. The cross-sectional geometrical structure of these waveguides is represented in Figure 1.1. While the lengthwise structure of the core is along the z-axis, the wave propagation axis is dependent on the function of the PLC waveguides e.g. it has a Y-shape for a power splitter [8].

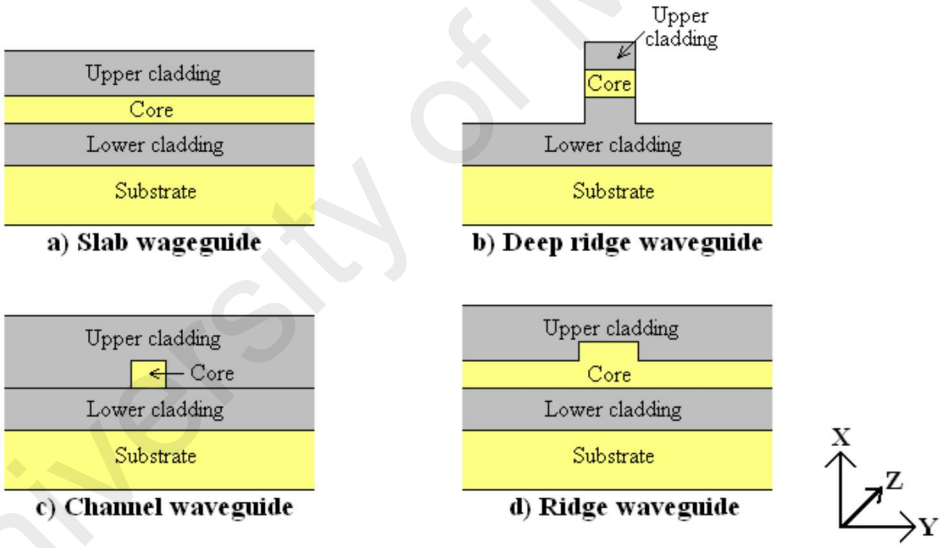

Figure 1.1: Types of waveguides structure with light propagation along z-axis.

1.2.1 Planar Lightwave Circuits Technology

Silica-on-silica PLCs offer aforementioned competitive commercial value and fall within the category of low index contrast optical waveguides, wherein the refractive index difference between core and cladding is below 1%. Index contrast is important in waveguide design because this parameter determines the main characteristic of light

propagation and the dimension of the waveguide [9]. A low index contrast has a typical square core dimension ranging from 5 to 9 μm with very low optical loss of 0.05 dB/cm, low birefringence and very high coupling efficiency in comparison to standard single mode fibre. The minimal bending radius of 5 mm in low index contrast waveguides limits the scale of function integration in a single chip [9, 10]. On the other hand, high index contrast waveguides, such as Silicon Photonics with index contrast of up to 140%, overcome these limitations due to a small bending radius of a few microns. However, this high index waveguide structure suffers from high coupling loss compared to ordinary fibre due to a sub-micron core size, high scattering loss due to core surface roughness, mode hybrid (light polarisation), stress and birefringence [10].

The medium index contrast waveguide, referring to optical waveguides having index contrast of 2% to 10%, balances the ideal of high function integration with realistic application within current optical fibre network systems. Usually a medium index contrast waveguide will have an optical propagation loss of less than 0.2 dB/cm with minimum bending radius of less than 300 μm. Typical examples of medium index contrast waveguides are silicon oxynitride and polymer. In this thesis work, we focus on medium index contrast waveguide design and application.

1.2.2 Polymer Based Waveguides

As mentioned earlier, one example of medium index contrast waveguide is a polymer-based waveguide. Polymeric platforms are usually chosen for integrated optical devices as they are relatively cheap to fabricate compared to silica waveguides. Typically, the polymer material used as core is photosensitive and can be patterned by photolithography or direct writing. In terms of fabrication, the polymer can be directly spun-coated onto a base substrate. The base substrate can be silica or another polymer

material that has lower refractive index. This core layer subsequently undergoes patterning and finally optionally has a cover added consisting of another polymer material [11-14]. With this simple fabrication process, the use of bulky machines such as glass deposition, metal deposition and dry etching system can be avoided and thus reduce the chip fabrication cost. Examples of polymer waveguide material are PMMA [15], PDMS [16] and BCB [17-20].

Gradually SU-8 formulated by Microchem Corporation become a popular candidate for polymer optical device development due to its high optical transparency and its ability to yield structures possessing high aspect ratio. The relatively low synthesis cost and process temperature of polymer-based devices also translated into lower production cost with the possibility of electronics integration, which is itself a low temperature process [12, 14, 21]. More details on SU-8 will be discussed in chapter 3. It is worth nothing that SU-8 was chosen in this thesis work as the material of the basic optical waveguide platform. We then integrate Graphene Oxide film on to this basic optical platform to further explore optical chip functionality.

1.3 Graphene Photonics

Pencils were developed a century ago and consist of Graphite (carbon atoms in a crystalline structure) sandwiched between 2 pieces of wood. It took until 2004 for single layer Graphite, known as Graphene, to be successfully isolated out from Graphite by the physicists Andre Geim and Konstantin Novoselov, who were consequently awarded a Nobel Prize in 2010 [22]. Thereafter, Graphene and Graphene Oxide (GO) became a hot research topic due to its superb natural properties whereby signal emitting, transmitting modulating, and detection can be all integrated onto one single chip. Besides, Graphene shows remarkably high thermal conductivity, high optical damage threshold, and high

third-order optical nonlinearities properties [23-27]. Graphene also shows a frequency-independent optical transmittance that is solely determined by the theoretical fine structure constant (~2.3% of broadband absorption per layer). Moreover, this dielectric property can be controlled via chemical doping (oxidation of Graphene become Graphene Oxide) and electron doping. As a result, Graphene has been applied in Graphene waveguides, broadband polarisers, Graphene modulators, Graphene photodetectors, and saturable absorbers for mode lock and Q-switched lasers [28-35].

Although Graphene has many advantages, perfect single layer Graphene sheets are not easy to obtain in large quantities, as they require creation via a CVD system. Most of the Graphene sheet is in it's oxidized form, Graphene Oxide (GO), which is simple to fabricate from Graphite via Hummer's method (this will be discussed in chapter 4). In this thesis work, the optical light (visible and telecommunication band – 1550 nm) interaction with GO Film (GOF) was studied. GOF allows for a light polarisation effect due to it's natural anisotropic dielectric properties. This effect was exploited within optical waveguides to achieve a waveguide polariser, water and humidity sensing, and optical switch control.

1.4 Thesis Objective and Outline

The objectives of this work are

1) To characterize the fabricated GOF using drop-casting
2) To functionalize planar optical waveguide with GOF coating to achieve
    a. Broadband waveguide polarizer which can be used in the 2nd and 3rd optical communication windows.
    b. All optical humidity sensing with high resolution (1% RH)
    c. All optical switch / modulator with more than 50% modulation efficiency

The achievement of these objectives is outlined as follows.

The waveguide principle and light polarisation principle will be discussed in the next chapter. A comparison of simulation method and software will be discussed as well. Details of the overall optical chip fabrication process will be discussed in chapter 3. In this chapter, the basic aspect of polymer waveguide fabrication will be discussed, which includes the fabrication environment, choosing the suitable substrate, pattern definition, and optical characterization. The pattern definition method that will be discussed is mainly focused on a photolithography technique. GO preparation (via Hummer's method), GOF fabrication (via drop-casting technique) and its characterisation are discussed in chapter 4. Chapters 5 to 7 are mainly focused on the application of the GOF coating on optical waveguides: on-chip polarisers in chapter 5, water - humidity sensing in chapter 6, and optical switches in chapter 7. Finally, a thesis conclusion and future potential work will be discussed in chapter 8.

References

1. *The Nobel Prize in Physics 2009*, in *Nobel Prize Organization*. 2009.

2. McCracken, H., *THe Web at 25: Revisiting Tim Berners-Lee's Amazing Proposal*, in *Time*. March 2014, Time.

3. Pearson, M., *FTTx Technologies: Planar Lightwave Circuits Revolutionize photonics.*, in *Laser Focus World*. 2007.

4. *TM showcases fiber-to-the-home (FTTH) technology delivering high-speed broadband access service from 10MBps up to maximum speed of 100Mbps to the home.*, in *News Release Telekom Malaysia*. TMRND.

5. Mynbaev, D.K. and L.L. Scheiner, *Fiber-optic Communications Technology*. 2001: Prentice Hall.

6. Jung, S.-T., et al., *Inductively coupled plasma etching of SiO2 layers for planar lightwave circuits.* Thin Solid Films, 1999. **341**(1–2): p. 188-191.

7. Adikan, F.R.M., *Direct UV-written waveguide devices*, in *Optoelectronic Research Centre*. 2007, University of Southampton.

8. Calvo, M.L. and V. Lakshminarayanan, *Optical Waveguides:From Theory to Applied Technologies*. 2007, Boca Raton: CRC Press Taylor & Francis Group.

9. Melloni, A., et al., *The role of index contrast in dielectric optical waveguides.* International Journal of Materials and Product Technology, 2009. **34**(4): p. 421-437.

10. Melloni, A., et al. *Waveguide index contrast: implications for passive integrated optical components*. in *Fibres and Optical Passive Components, 2005. Proceedings of 2005 IEEE/LEOS Workshop on*. 2005.

11. Ma, H., A.K.Y. Jen, and L.R. Dalton, *Polymer-Based Optical Waveguides: Materials, Processing, and Devices.* Advanced Materials, 2002. **14**(19): p. 1339-1365.

12. Eldada, L. and L.W. Shacklette, *Advances in polymer integrated optics.* Selected Topics in Quantum Electronics, IEEE Journal of, 2000. **6**(1): p. 54-68.

13. Eldada, L., et al., *Laser-fabricated low-loss single-mode raised-rib waveguiding devices in polymers.* Lightwave Technology, Journal of, 1996. **14**(7): p. 1704-1713.

14. Eldada, L., *Optical communication components.* Review of Scientific Instruments, 2004. **75**(3): p. 575-593.

15. Jaesun, K., et al. *UV written waveguides using crosslinkable PMMA-based copolymers*. in *Lasers and Electro-Optics, 2002. CLEO '02. Technical Digest. Summaries of Papers Presented at the*. 2002.

16. Zhao, X.-M., et al., *Demonstration of waveguide couplers fabricated using microtransfer molding.* Applied Physics Letters, 1997. **71**(8): p. 1017-1019.

17. Kane, C.F. and R.R. Krchnavek, *Benzocyclobutene optical waveguides.* IEEE Photonics Technology Letters 1995. **7**(5): p. 535-537.

18. Kane, C.F. and R.R. Krchnavek, *Processing and characterization of benzocyclobutene optical waveguides.* Components, Packaging, and Manufacturing Technology, Part B: Advanced Packaging, IEEE Transactions on, 1995. **18**(3): p. 565-571.

19. Yahya, N.A.M., et al., *Curing Methods Yield Multiple Refractive Index of Benzocyclobutene Polymer Film.* World Academy of Science, Engineering and Technology, 2011. **74**: p. 540-542.

20. Yahya, N.A.M., et al., *Fabrication and characterization of a dual layer multiple refractive index benzocyclobutene polymer platform for integrated optical devices.* Optical Materials, 2012. **34**(11): p. 1735-1741.

21. Dey, P.K. and P. Ganguly, *A technical report on fabrication of SU-8 optical waveguides.* Journal of Optics, 2014. **43**(1): p. 79-83.

22. *The Nobel Prize in Physics 2010*, in *Nobel Prize Organization*. 2010.

23. Bonaccorso, F., et al., *Graphene photonics and optoelectronics.* Nat Photon, 2010. **4**(9): p. 611-622.

24. Bao, Q. and K.P. Loh, *Graphene Photonics, Plasmonics, and Broadband Optoelectronic Devices.* ACS Nano, 2012. **6**(5): p. 3677-3694.

25. Roberts, A., et al., *Response of Graphene to femtosecond high-intensity laser irradiation.* Applied Physics Letters, 2011. **99**(5): p. -.

26. Garg, A., A. Kapoor, and K.N. Tripathi, *Laser-induced damage studies in GaAs.* Optics & Laser Technology, 2003. **35**(1): p. 21-24.

27. Hendry, E., et al., *Coherent Nonlinear Optical Response of Graphene.* Physical Review Letters, 2010. **105**(9): p. 097401.

28. Bao, Q., et al., *Broadband Graphene polarizer.* Nature Photon., 2011. **5**: p. 411.

29. Liu, M., et al., *A Graphene-based broadband optical modulator.* Nature, 2011. **474**: p. 64.

30. Mueller, T., et al., *Role of contacts in Graphene transistors: A scanning photocurrent study.* Physical Review B, 2009. **79**(24): p. 245430.

31. Xia, F., et al., *Photocurrent Imaging and Efficient Photon Detection in a Graphene Transistor.* Nano Letters, 2009. **9**(3): p. 1039-1044.

32. Mueller, T., F. Xia, and P. Avouris, *Graphene photodetectors for high-speed optical communications.* Nat Photon, 2010. **4**(5): p. 297-301.

33. Xia, F., et al., *Ultrafast Graphene photodetector.* Nat Nano, 2009. **4**(12): p. 839-843.

34. Zhao, L.M., et al., *Dissipative soliton operation of an ytterbium-doped fiber laser mode locked with atomic multilayer Graphene.* Optics Letters, 2010. **35**(21): p. 3622-3624.

35. Lim, G.-K., et al., *Giant broadband nonlinear optical absorption response in dispersed Graphene single sheets.* Nat Photon, 2011. **5**(9): p. 554-560.

CHAPTER 2: WAVEGUIDE THEORY AND SIMULATION

In this chapter, optical waveguide theory and simulation will be discussed for guided modes in a homogenous medium as well as in complex structures such as a channel in a planar waveguide. The two common simulation techniques, FDTD and FEM, with their corresponding simulation software are also discussed in detail.

2.1 Waveguide Theory

It was well known from the Ray theory of light that light travelled in a straight line with a finite velocity in a homogenous medium such as air or vacuum. Optical elements or waveguides are needed to route light into the desired optical path, where the term waveguide refers to a structure that guides waves such as electromagnetic waves or sound wave. Different waveguide structures are required for guiding different types of wave or even a different range of frequency. For example, a hollow conductive metal pipe was used to guide microwaves while a dielectric medium such as fibre optic was found suitable to guide optical frequency waves. In this chapter, only optical waveguides are discussed.

2.1.1 Formation of Guided Modes in A Waveguide

An optical waveguide consists of a dielectric core in which light is confined, and a lower refractive index dielectric cladding that surrounds the core. Figure 2.1 illustrates a slab waveguide core with refractive n_c on a substrate with refractive index n_{sub} and covered by a cladding with refractive index n_{clad}. Optical light is guided along the z-axis and this structure is extended to infinity along the y-axis. The basic guiding principle of an optical waveguide is based on total internal refraction between the core and cladding boundary due to the difference in refractive index. For simplicity, assume $n_{sub} = n_{clad}$, which is a logical assumption for means of obtaining isotropic waveguides as is

practiced in the commercial waveguide industry to reduce the polarisation-dependent loss. From Snell's Law,

$$n_1 \sin \theta_{ic} = n_c \sin \alpha_c \qquad \text{Eqn 2.1}$$

and usually the medium of n_i is air, which is approximately 1. Θ_{ic} is defined as the **critical incident angle** (also known as **acceptance angle**) and α_c is defined as the **critical propagation angle**. Incident light that has an angle smaller than Θ_{ic} will be guided in this slab waveguide whereas differently angled light (the dotted line) will be leaking out from this slab waveguide.

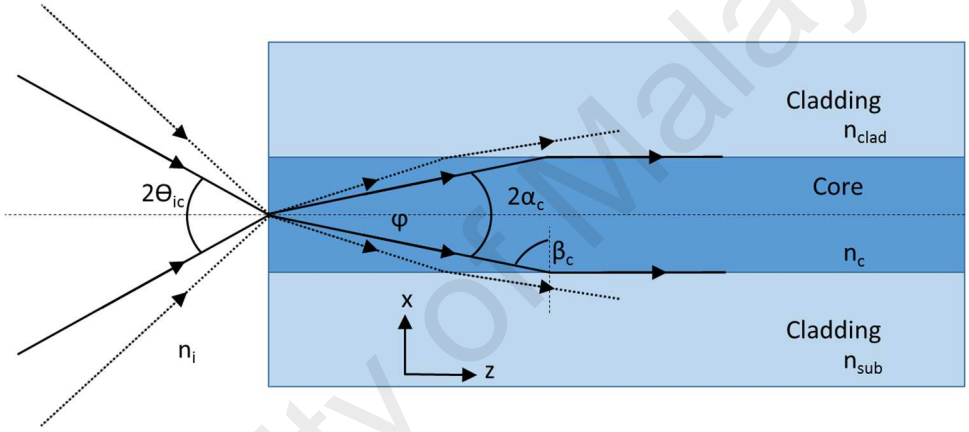

Figure 2.1: Geometrical structure of a slab waveguide.

Numerical Aperture (NA) is a dimensionless number that characterizes the range of angles over which the system can accept or emit light. Hence NA is defined as below,

$$NA = \sin \theta_{ic} = n_c \sin \alpha_c \qquad \text{Eqn 2.2}$$

The term sin α_c can be replaced by another set of Snell's Law purely based on n_c and n_{clad} as below,

$$n_c \sin \beta_c = n_{clad} \sin 90^o = n_{clad} \qquad \text{Eqn 2.3}$$

The angle β_C and α_C are interchangeable where,

$$\sin \beta_c = \cos \alpha_c = \frac{n_{clad}}{n_c} \qquad \text{Eqn 2.4}$$

and with the simple theorem of Pythagoras, the identity becomes as below,

$$sin\ \alpha_c = \sqrt{1 - cos^2\ \alpha_c} = \sqrt{1 - \frac{n_{clad}}{n_c}} \quad \text{Eqn 2.5}$$

NA can be rewritten as below,

$$NA = \sqrt[2]{n_c^2 - n_{clad}^2} \quad \text{Eqn 2.6}$$

where it can be recognized as a unit purely based on the refractive index of the waveguide structure. Another important definition term in the waveguide is **refractive index difference**, Δ given by

$$\Delta = \frac{n_c^2 - n_{clad}^2}{2n_c^2} \cong \frac{n_c - n_{clad}}{n_c} \quad \text{Eqn 2.7}$$

and practically approximate to the form in the right hand side if the difference in refractive index of the core and cladding is small. Refractive index difference is commonly expressed as a percentage, which is a useful factor in waveguide fabrication. The term NA can be further expressed as below,

$$NA = n_c \sqrt[2]{2\Delta} \quad \text{Eqn 2.8}$$

The paragraph above discussed the mechanism of mode confinement of light that involves the incident angle within the acceptance angle. However, not all light rays with incident angle within the acceptance angle can be guided, and this is related to the guided modes of the waveguide that are discrete in nature. Let consider a plane wave with wavenumber of $n_c k$ ($k = 2\pi/\lambda$, λ is the wavelength of light in vacuum) propagating in the core along z-axis with an angle ϕ ($\phi < \alpha_c$) as shown in Figure 2.2.

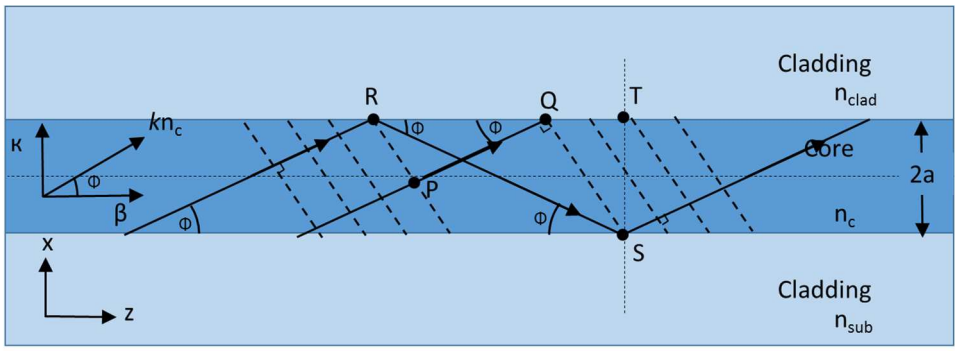

Figure 2.2: Light rays (with an angle ϕ) and their corresponding phase fronts (dotted line) in a slab waveguide with core size 2a.

According to the phase fronts diagram in Figure 2.2, the phase fronts at points P, Q, R, and S should be equal. The light ray RS is reflected twice at the core-cladding boundary may encounter phase shift, Φ known as the Goos-Hanchen shift. The phase shift Φ can be derived from the Fresnel equation. By applying the boundary condition arising from Maxwell equation, the electric field, **E** and magnetic field, **B** of the light ray parallel to the boundary plane is continuous at the boundary. Consider the light ray polarised perpendicular to the incident plane (TE-mode), such that two sets of equation based on boundary condition can be made as below,

$$\mathbf{E}_i + \mathbf{E}_r = \mathbf{E}_t \qquad \text{Eqn 2.9}$$

$$\mathbf{B}_i \sin\phi - \mathbf{B}_r \sin\phi = \mathbf{B}_t \sin\phi_t \qquad \text{Eqn 2.10}$$

Where subscript i ,r, and t are referring to incident, reflected and transmitted light ray, ϕ_t is the angle of the transmitted light ray into the cladding. The magnetic field **B** can be replaced by $\mathbf{B} = n\mathbf{E}/c$, where c is the speed of light and Eqn 2.10 can be rewritten as

$$n_{core}\,\mathbf{E}_i \sin\phi - n_{core}\,\mathbf{E}_r \sin\phi = n_{clad}\,\mathbf{E}_t \sin\phi_t \qquad \text{Eqn 2.11}$$

Eliminating $\mathbf{E}_t$ in Eqn 2.9 and Eqn 2.11, and ϕ_t using Snell's law, the reflection coefficient, R of the total reflected light can be expressed as

$$R = \frac{\boldsymbol{E_r}}{\boldsymbol{E_i}} = \frac{n_c \sin\phi + j\sqrt{n_c^2\, cos^2\phi - n_{clad}^2}}{n_c \sin\phi - j\sqrt{n_c^2\, cos^2\phi - n_{clad}^2}} \qquad \text{Eqn 2.12}$$

The reflection coefficient takes above the form of R = (x- iy) / (x+ iy), hence the phase of R can be expressed in the form

$$R = \frac{e^{-i\Phi}}{e^{i\Phi}} = e^{-2i\Phi} \quad \text{Eqn 2.13}$$

and the phase Φ can be obtained by

$$\tan\frac{\Phi}{2} = \frac{y}{x} \quad \text{Eqn 2.14}$$

Eqn 2.14 can be rearranged into the following form

$$\Phi = -2tan^{-1}\frac{\sqrt{n_{core}^2\, cos^2\phi - n_{clad}^2}}{n_{core}\, \sin\phi} \quad \text{Eqn 2.15}$$

By substituting Eqn 2.7 and simple trigonometry identity,

$$\Phi = -2tan^{-1}\sqrt{\frac{2\Delta}{sin^2\phi} - 1} \quad \text{Eqn 2.16}$$

The difference in optical path of light ray PQ and RS (including the Goos-Hanchen shift) should be an integral multiple of 2π. The length RS, ℓ_{RS} is expressed by

$$\ell_{RS} = \frac{2a}{\sin\phi} \quad \text{Eqn 2.17}$$

while the length PQ, ℓ_{PQ} can be expressed by

$$\ell_{PQ} = \ell_{RQ}\cos\phi \quad \text{Eqn 2.18}$$

where ℓ_{RQ} is the length between point R and Q. The length RQ is also related to length RT, ℓ_{RT} and length QT, ℓ_{QT}. Both length ℓ_{RT} and ℓ_{QT} can be derived in terms of core size and angle ϕ.

$$\ell_{RQ} = \ell_{RT} - \ell_{QT} \quad \text{Eqn 2.19}$$

$$\ell_{RT} = \frac{2a}{\tan\phi} \quad \text{Eqn 2.20}$$

$$\ell_{QT} = 2a\tan\phi \quad \text{Eqn 2.21}$$

The phase matching condition for optical path PQ and RS then becomes

$$(kn_c\ell_{RS} + 2\,\Phi) - kn_c\ell_{PQ} = 2m\pi \qquad \text{Eqn 2.22}$$

where m is an integer. Substituting Eqn 2.16 to Eqn 2.21, Eqn 2.22 and by eliminating Φ, the condition for the propagation angle ϕ is

$$\tan\left(kn_c a \sin\phi - \frac{m\pi}{2}\right) = \sqrt{\frac{2\Delta}{sin^2\phi} - 1} \qquad \text{Eqn 2.23}$$

Eqn 2.23 shows that the propagation angle of confined light in the waveguide core is discrete and determined by the core size, core refractive index, cladding refractive index and wavelength. The optical field distribution that satisfies this phase matching condition is called a mode and it has a discrete propagation constant β_m, where m = 0 refers to the fundamental mode.

For a guided mode $\phi \leq \alpha$, hence $n_c \sin\phi \leq NA$. By substituting Eqn 2.8 and introducing a parameter ratio ζ,

$$\zeta = \frac{\sin\phi}{\sqrt{2\Delta}} \leq 1 \qquad \text{Eqn 2.24}$$

By using trigonometric identity

$$tan^{-1}x = cos^{-1}\frac{1}{\sqrt{1+x^2}} \qquad \text{Eqn 2.25}$$

and Eqn 2.24, the phase matching Eqn 2.23 can be rewritten as

$$kn_c a\sqrt{2\Delta} = kaNA = \frac{cos^{-1}\zeta + \mathrm{m}\frac{\pi}{2}}{\zeta} = V \qquad \text{Eqn 2.26}$$

where a new parameter V known as normalised frequency (or V-number) is defined.

V-Number can be interpreted as normalized optical frequency that determines the confinement factor of energy in the core for different wavelengths. V-number also can be used to determine the number of operation modes potentially supported by a particular waveguide. In the case of the slab waveguide above, for fundamental mode, m = 0, since ζ maximum = 1, $V \leq \pi / 2$. This means that if a slab waveguide will only support 1 mode (which is fundamental mode) if $V \leq \pi / 2$. In fibre, a similar

mathematical derivation has been conducted with the finding that the cut-off V-number is 2.405. Fibres possessing V > 2.405 are usually multimode waveguide that can support up to approximately V^2 / 2 modes. Rearranging Eqn 2.26 with substituted maximum V- number for single mode operation allows for the cut-off wavelength λ_c to be obtained

$$\lambda_c = \frac{\pi d}{V_{max}} NA \qquad \text{Eqn 2.27}$$

where d is the diameter of the core.

Mode Field Diameter (MFD), w, refers to the lateral position of the Gaussian field power density reduced to $1/e^2$ of the maximum power density away from the waveguides centre in single mode operation waveguides. To date, there are many approximations that calculate MFD, such as Marcuse model, Myslinski model, Desurvire Model, and Whitley model.

$$\frac{w}{d} = 0.65 + \frac{1.619}{V^{\frac{3}{2}}} + \frac{2.879}{V^6}$$

$$\frac{w}{d} = 0.761 + \frac{1.237}{V^{\frac{3}{2}}} + \frac{1.429}{V^6}$$

$$\frac{w}{d} = 0.759 + \frac{1.289}{V^{\frac{3}{2}}} + \frac{1.041}{V^6}$$

$$\frac{w}{d} = 0.616 + \frac{1.66}{V^{\frac{3}{2}}} + \frac{0.987}{V^6} \qquad \text{Eqn 2.28}$$

$$\frac{w}{d} = \frac{1}{\ln V}$$

The ratio w/d is known as normalised MFD or normalised spot size. This ratio shows how MFD changes with respect to the core radius that is constant for a given waveguide or fibre.

Polarisation in Plane Wave – optical light can be classified into polarised an unpolarised. In a plane wave, the electric field vector always oscillates parallel to a fixed direction of spaces, and this called linearly polarised light. The electric field of a

linearly polarised light can be parallel (p - polarised) or perpendicular (s - polarised) to its plane of propagation. In fibre, due to the cylindrical symmetry structure, there will be no difference between these two polarisations. However, in planar waveguides, the term TE is denoted for the electric field polarised parallel to the substrate axis which is y-axis, and likewise TM is denoted for electric field polarised perpendicular to the substrate axis which is x-axis, as shown in Figure 2.2. These two modes are important in solving the set of Maxwell's equation to obtain the dispersion relation of a particular waveguide structure. For a square core waveguide with homogeneous cladding refractive index, this polarisation effect will not be significant. However, an asymmetric cladding refractive index or/and rectangular core will cause the waveguide to operate in two different modes and result in signal broadening. Hence, extra attention is needed in designing waveguide with such structures.

Dispersion Equation in Slab Waveguide

Considering the slab waveguide structure as shown in Figure 2.2, a set of Maxwell's equations can be obtained to describe the electromagnetic field distribution of every mode in the waveguide. The two basic Maxwell's equations are

$$\nabla \times \vec{\boldsymbol{E}} = -\mu_o \frac{\partial \vec{\boldsymbol{H}}}{\partial t} \qquad \text{Eqn 2.29}$$

$$\nabla \times \vec{\boldsymbol{B}} = -\varepsilon_o n^2 \frac{\partial \vec{\boldsymbol{E}}}{\partial t}$$

where $\vec{\boldsymbol{E}}$ and $\vec{\boldsymbol{H}}$ are the electric and magnetic field of the propagating wave. For a slab waveguide, the optical light is confined and propagates along the z-axis, hence plane wave propagation is in the following form

$$\vec{\boldsymbol{E}} = E(x,y)e^{j(\omega t-\beta z)} \qquad \text{Eqn 2.30}$$

$$\vec{\boldsymbol{H}} = H(x,y)e^{j(\omega t-\beta z)}$$

substituting Eqn 2.30 in Eqn 2.29, the following set of equations for the electromagnetic field components can be obtained.

$$\frac{\partial E_z}{\partial y} + j\beta E_y = -j\omega\mu_o H_x$$

$$-j\beta E_x - \frac{\partial E_z}{\partial x} = -j\omega\mu_o H_y \qquad \text{Eqn 2.31}$$

$$\frac{\partial E_y}{\partial x} - \frac{\partial E_x}{\partial y} = -j\omega\mu_o H_Z$$

$$\frac{\partial H_z}{\partial y} + j\beta H_y = j\omega\varepsilon_o n^2 E_x$$

$$-j\beta H_x - \frac{\partial H_z}{\partial x} = j\omega\varepsilon_o n^2 E_y \qquad \text{Eqn 2.32}$$

$$\frac{\partial H_y}{\partial x} - \frac{\partial H_x}{\partial y} = j\omega\varepsilon_o n^2 E_Z$$

In an ideal slab waveguide, the electromagnetic field $\vec{\boldsymbol{E}}$ and $\vec{\boldsymbol{H}}$ in the y-axis should be extended to infinity and hence the terms $\partial\vec{\boldsymbol{E}}/\partial y = 0$ and $\partial\vec{\boldsymbol{H}}/\partial y = 0$.

For TE-mode, $E_x = E_z = H_y = 0$, the equation Eqn 2.31 and Eqn 2.32 can simplified to

$$\frac{\partial^2 E_y}{\partial x^2} + (k^2 n^2 - \beta^2) E_y = 0 \qquad \text{Eqn 2.33}$$

On the other hands, for TM-mode, $E_y = H_x = H_z = 0$, the equation Eqn 2.31 and Eqn 2.32 can simplify to

$$\frac{\partial}{\partial x}\left(\frac{1}{n^2}\frac{\partial H_y}{\partial x}\right) + \left(k^2 - \frac{\beta^2}{n^2}\right) H_y = 0 \qquad \text{Eqn 2.34}$$

The above two equations are in form of an eigenvalue equation. If the guided TE electromagnetic fields are considered to be confined in the core and exponentially decay in the cladding, the electric field distribution can be expressed as

$$E_y = \begin{cases} A\cos(\kappa a - \phi)\mathrm{e}^{-\sigma(x-a)} & (x > a) \\ A\cos(\kappa x - \phi) & (-a \le x \le a) \\ A\cos(\kappa a + \phi)\mathrm{e}^{\xi(x+a)} & (x < -a) \end{cases} \qquad \text{Eqn 2.35}$$

where κ, σ and ξ are wavenumbers along the x-axis in the core and cladding regions, and are given by

$$\kappa = \sqrt{k^2 n_c^2 - \beta^2}$$
$$\sigma = \sqrt{\beta^2 - k^2 n_o^2}$$
$$\xi = \sqrt{\beta^2 - k^2 n_s^2} \qquad \text{Eqn 2.36}$$

Both the electric field E_y and magnetic field H_z should be maintained at the core-cladding interface ($x = \pm a$). From equation Eqn 2.31, H_z is related to the derivative of E_y as below,

$$H_z = \frac{j}{w\mu_o}\frac{\partial E_y}{\partial x} \qquad \text{Eqn 2.37}$$

By taking the derivative of E_y in Eqn 2.35,

$$\frac{\partial E}{\partial x} = \begin{cases} -\sigma A \cos(\kappa a - \phi) e^{-\sigma(x-a)} & (x > a) \\ -\kappa A \sin(\kappa x - \phi) & (-a \le x \le a) \\ \xi A \cos(\kappa a + \phi) e^{\xi(x+a)} & (x < -a) \end{cases} \qquad \text{Eqn 2.38}$$

From the condition that H_z should be continued at core-cladding interface, the following two equations can be obtained,

$$\kappa \sin(\kappa a + \phi) = \xi \cos(\kappa a + \phi) \qquad \text{Eqn 2.39}$$
$$\sigma \cos(\kappa a - \phi) = \kappa \sin(\kappa a - \phi)$$

By defining a new variable for normalised wavenumber,

$$u = \kappa a$$
$$w = \xi a \qquad \text{Eqn 2.40}$$
$$w' = \sigma a$$

Eqn 2.39 can be simplified to

$$\tan(u + \phi) = \frac{w}{u} \qquad \text{Eqn 2.41}$$
$$\tan(u - \phi) = \frac{w'}{u}$$

Finally an eigenvalue equation can be obtained as

$$u = \frac{m\pi}{2} + \frac{1}{2}\tan^{-1}\frac{w}{u} + \frac{1}{2}\tan^{-1}\frac{w'}{u} \quad (m = 0,1,2,\dots) \qquad \text{Eqn 2.42}$$
$$\phi = \frac{m\pi}{2} + \frac{1}{2}\tan^{-1}\frac{w}{u} - \frac{1}{2}\tan^{-1}\frac{w'}{u}$$

All three normalised wavenumber u, w, and w' are not independent. By defining the term normalised frequency ν in relation to u and w with

$$\nu^2 = u^2 + w^2 \qquad \text{Eqn 2.43}$$

and substituting Eqn 2.36 into Eqn 2.43, the following equation can be obtained

$$\nu^2 = k^2 a^2 (n_c^2 - n_{sub}^2) \qquad \text{Eqn 2.44}$$
$$w' = \sqrt{\gamma \nu^2 + w^2}$$

where

$$\gamma = \frac{n_{sub}^2 - n_{clad}^2}{n_c^2 - n_{sub}^2} \qquad \text{Eqn 2.45}$$

where the subscript n_c and n_{sub} are referring to the refractive index of core and substrate. The term γ is a measure of asymmetry of the cladding refractive index. Once the frequency and the geometry of the waveguide are defined, the normalised frequency ν and γ can be determined. Therefore, the three normalised wavenumber u, w, w' and ϕ can be obtained by solving Eqn 2.42 under the constraints of Eqn 2.44 and eventually the propagation wavenumber β can be deduced. In an asymmetric waveguide, there are no particular discriminate of which side is cladding and substrate. However, the side that has a higher refractive index will be assigned to n_{sub} for the normalised frequency calculation in Eqn 2.44. The motive of using higher refractive as n_{sub} is because the cut-off condition is determined when the normalised propagation constant, β/k coincides with the higher refractive index surrounding boundary. The normalised propagation constant is dimensionless and is a "refractive index" itself in the plane waves that propagate in the core. Hence, this term is known as effective index n_e, and the condition below must satisfy

$$n_s \leq n_e \leq n_c \qquad \text{Eqn 2.46}$$

By defining a new term as normalised propagation constant b,

$$b = \frac{n_e^2 - n_{sub}^2}{n_c^2 - n_{sub}^2} \qquad \text{Eqn 2.47}$$

Eqn 2.46 can be normalised to $0 \leq b \leq 1$, with the cut-off condition expressed as $b = 0$. Rewriting Eqn 2.40 and Eqn 2.42 in term of ν and b,

$$2\nu\sqrt{1-b} = m\pi + \tan^{-1}\sqrt{\frac{b}{1-b}} + \tan^{-1}\sqrt{\frac{b+\gamma}{1-b}} \qquad \text{Eqn 2.48}$$

$$\begin{aligned} u &= v\sqrt{1-b} \\ w &= v\sqrt{b} \\ w' &= v\sqrt{b+\gamma} \end{aligned} \qquad \text{Eqn 2.49}$$

For a symmetric slab waveguide with $n_{clad} = n_{sub}$, $\gamma = 0$, the dispersion equation Eqn 2.48 can be simplified to

$$\nu\sqrt{1-b} = \frac{m\pi}{2} + \tan^{-1}\sqrt{\frac{b}{1-b}} \qquad \text{Eqn 2.50}$$

which is equal to Eqn 2.23 by replacing $u = k\, n_c\, a \sin\phi$. At cut off condition, $b = 0$, then from Eqn 2.49, $w = 0$ and $u = \nu$. Deduced from Eqn 2.50, $\nu = \pi / 2$ which is the same condition as in Eqn 2.26. Eqn 2.50 only can be solved by numerical method and the following equation can be used to calculate the optical power of TE-mode distribution:

$$P_{TE} = \frac{\beta}{2\omega\mu_o}\int_{-\infty}^{\infty}\left|E_y\right|^2 dx \qquad \text{Eqn 2.51}$$

On the other hand, for TM-mode, the magnetic distribution H_y can be expressed as

$$H_y = \begin{cases} A\cos(\kappa a - \phi)e^{-\sigma(x-a)} & (x > a) \\ A\cos(\kappa x - \phi) & (-a \leq x \leq a) \\ A\cos(\kappa a + \phi)e^{\xi(x+a)} & (x < -a) \end{cases} \qquad \text{Eqn 2.52}$$

By applying the boundary condition H_y and E_z should be continuous at $x = \pm a$. After going through similar steps as in the TE-mode derivation above, the dispersion relation can be obtained as the following, or in the normalised frequency mode.

$$u = \frac{m\pi}{2} + \frac{1}{2}\tan^{-1}\frac{n_c^2 w}{n_{sub}^2 u} + \frac{1}{2}\tan^{-1}\frac{n_c^2 w'}{n_{clad}^2 u} \qquad \text{Eqn 2.53}$$

$$2\nu\sqrt{1-b} = m\pi + \tan^{-1}\frac{n_c^2}{n_{sub}^2}\sqrt{\frac{b}{1-b}} + \tan^{-1}\frac{n_c^2}{n_{clad}^2}\sqrt{\frac{b+\gamma}{1-b}} \qquad \text{Eqn 2.54}$$

Similarly, the power distribution of the TM-mode can be obtained by

$$P_{TE} = \frac{\beta}{2\omega\varepsilon_o}\int_{-\infty}^{\infty}\frac{1}{n^2}\left|H_y\right|^2 dx \qquad \text{Eqn 2.55}$$

2.1.2 Analytical and Numerical Approached

In the above section, only a slab waveguide was considered where the electric and magnetic fields are independent of the y-axis, or $\partial\vec{\boldsymbol{E}}/\partial y = 0$ and $\partial\vec{\boldsymbol{H}}/\partial y = 0$. However, in practice, a square core with a homogenous refractive index cladding surrounding the core structure is used. The reason of using such dimensions is that the light confinement is superior and can reduce polarisation dependent loss. As a result, equation Eqn 2.31 and Eqn 2.32 become complicated to solve with the addition of the y- dimension. Kumar et al., based on Marcatili's earlier work, suggest that this structure can analysed using approximation by separating it into two independent slab waveguides which will only be combined for the dispersion equation after analysis to obtain their mode details such as energy distribution as well as the optical loss of that particular mode. These details are important in optical component design. For example, by knowing the optical loss of the guided waveguide mode, the 3-dimension problem can be reduced to a 2-dimension problem where only the parameters of the component design need to be considered. Although Kumar's method gives a more accurate result, this method is restricted to a basic homogeneous rectangular structure. In research or advanced optical components, the waveguide structure can be complex, such as a rib waveguide or non-symmetric waveguide. These complex structures need another advanced approach known as Effective Index Method. The Effective Index Method assumes that the x- and y-components of electromagnetic field is independent between

each other. Hence the waveguide can be separated into a multilayer slab waveguide and the effective index of each particular mode can be calculated by applying a continuity condition between each layer.

Although several approaches have been introduced, more complex designs like graded index or the model design in chapter 5 are impossible to solve analytically. Numerical method was the only way to obtain a solution for such complicated structures. In this method the effective index, n_e of each mode is obtained via the finite element method or finite difference method. The details of this method will be discussed in section 2.3. Before that, the electromagnetic wave behaviour in different medium is discussed in section 2.2. Their behaviour is important, especially in simulations where material properties are required as input parameters.

2.2 Optical Loss in A Medium

Propagation of a light ray or waves in a medium will vary from one material to another. In general, all materials can be categorised into three categories: lossless, lossy and conductor. In an optical waveguide, the first two mediums are dominant and will be discussed in detail, whereas a description of optical light propagation in a conductor is disregarded.

Low-Loss Dielectric Medium

A source-free wave equation in non-conducting media is governed by the Helmholtz equation

$$\nabla^2\vec{\boldsymbol{E}} + k^2\vec{\boldsymbol{E}} = 0 \qquad \text{Eqn 2.56}$$

where k is the wavenumber that is related to the material properties of the media by

$$k = \omega\sqrt{\varepsilon\mu} = \frac{\omega}{u_p} \qquad \text{Eqn 2.57}$$

with

$$u_p = \frac{1}{\sqrt{\varepsilon\mu}} \qquad \text{Eqn 2.58}$$

where u_p is the velocity of the propagating wave, ε is permittivity, and μ is permeability of the medium. For simplicity, an ideal uniform plane wave with uniform E_x was used. Thereafter, Eqn 2.57 can be simplified to an ordinary differential equation formed that is dependent only on z. The solution of this equation will be in the following format

$$E(z,t) = E_o cos\,(\omega t - kz) \qquad \text{Eqn 2.59}$$

where E_o is the maximum electric field amplitude travelling in the z direction. In the context of optical frequencies, the term refractive index is preferred over the term dielectric constant. Hence, Eqn 2.58 is rewritten into

$$u_p = \frac{1}{\sqrt{\varepsilon_o\mu_0}\sqrt{\varepsilon_r\mu_r}} = \frac{C}{\sqrt{\varepsilon_r\mu_r}} = \frac{C}{n} \qquad \text{Eqn 2.60}$$

where *C* is the speed of light in free space and the subscript "0" and "r" denote free space and relative coefficient respectively. In naturally occurring materials, μ_r is usually equal to unity, hence the term refractive index is directly related to the square root of relative permittivity, $n^2 = \varepsilon_r$.

Lossy Medium

For a conducting medium that has an external time-varying electric field applied, the bound charges in the conducting medium will response to the external electric field. The small displacement of the bound charges results in a finite volume density of polarisation. The polarisation vector will vary with the same frequency as the applied field. As the frequency increases, the inertia of the charged particles tends to prevent the particle displacement from keeping in phase with the field changes; this effect acts as a damping force. Moreover, the movement of free charge carriers (which can be free electrons in a metal, electrons and holes in a semiconductor, or ions in an electrode) will

have ohmic losses, and these losses are incorporated into considerations of permittivity. Hence the term permittivity will take a complex form with $\varepsilon_r = \varepsilon' + j\varepsilon''$. Note that physicists tend to use "+" sign but engineer tend to use "-" sign. The conductivity σ that corresponds to all losses is directly proportional to ε'' and angular frequency.

$$\varepsilon'' = \frac{\sigma}{w} \qquad \text{Eqn 2.61}$$

Note that both real and imaginary parts of permittivity are frequency dependent. A good conductor at low frequencies might be a lossy dielectric at high frequencies. Similarly, a complex term must be introduced in regards to refractive index to take these losses into consideration, so $n = n_r + j\, n_c$. The refractive index and permittivity can be interchanged by

$$\epsilon_r' = n_r^2 + n_c^2 \qquad \text{Eqn 2.62}$$
$$\varepsilon_r'' = 2n_r n_c$$

Anisotropic Medium

Anisotropic properties are found in some naturally occurring materials such as ice, Sapphire, Graphite, and some two-dimensional material such as thin metal film, Graphene and GOF. Anisotropic means that the material has different physical or mechanical properties when measured along different axes. An anisotropic medium that has different refractive indices is known as a birefringent material. Extra care is necessary for selecting a particular material properties for polarisation modes in analytical or numerical simulation.

2.3 Simulation Method and Software

As mentioned in earlier, numerical method is the only practical solution to wave propagation in a complex waveguide structure. In general, there are two common numerical techniques, Finite Element Method (FEM) and Finite Difference Method (FDM). Both methods discretized the domain of the problem into small elements. By

solving the set of basic equations that govern the method, the properties of electromagnetic wave can be obtained in each element and then recombined to give a solution of the problem. Both techniques have their own basic equation sets, and have their own advantages in specific problems.

2.3.1 Finite Element Method

FEM is a powerful tool for effective mode analysis of optical waveguides having an arbitrary refractive index profile and complicated waveguide structure. Moreover, FEM is also applicable for stress analysis in optical waveguides. In FEM, the domain of the problem is discretized into smaller elements. The solution of the problem is approximated in each element and it is connected at the node points to form the solution model across the entire analysis domain. All of the elements contributions to the system are assembled from the functional, which consists of the field value at the n nodes and boundary conditions at the peripheral nodes. Hence an n-order of linear simultaneous equations is obtained. The solution of these linear simultaneous equations provides the unknown field values to be determined. Increasing the number of elements, which correspondingly reduces the element's size, can improve the accuracy of the determined field value. In general, FEM has better accuracy than FDM as the domain is discretized into triangle forms while FDM is in rectangular forms; a rectangular grid is not suitable for curved boundaries or interface where elements will intersect at points other than nodes. Similarly, rectangular grid lines are unsuitable for problems that have very steep field variation.

In general, analyses using FEM can be categorised into 3 steps. To aid discussion of these steps in detail, an example was used of a slab index with the graded core index, as shown in Figure 2.3. The inhomogeneous refractive index region $0 \leq x \leq$

A is denoted as the core with the maximum refractive of n_1. The refractive index of cladding and substrate is denoted as n_o and n_s with uniform refractive index distribution.

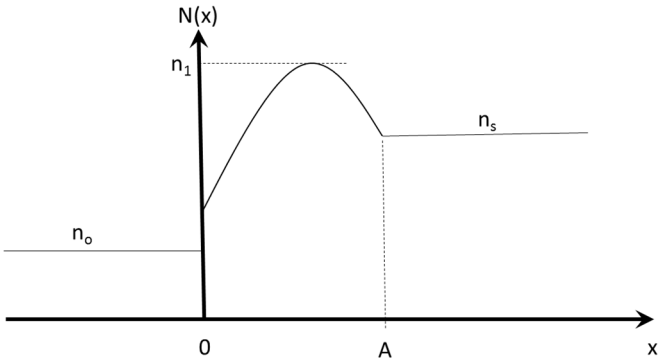

Figure 2.3: Refractive index distribution of the inhomogeneous slab optical waveguide.

Variational Formulation – Model Setup

Let the model setup begin with use of the general TE-mode equation that was described in Eqn 2.33. The boundary condition requires continuity of E_y and H_z (Eqn 2.37) at the $x = 0$ and $x = A$. For simplicity, the parameters were normalised with

$$\rho = x/a \qquad \text{Eqn 2.63}$$
$$E_y = R(\rho)$$
$$D = A/a$$

the wave equation can be rewritten as

$$\frac{d^2R}{d\rho^2} + [v^2 q(\rho) - w^2]R = 0 \qquad \text{Eqn 2.64}$$

where w is normalised transverse wavenumber, v is normalised frequency and $q(\rho)$ is normalised refractive index distribution defined by

$$w = a\sqrt{\beta^2 - k^2 n_s^2}$$
$$v = ka\sqrt{n_1^2 - n_s^2} \qquad \text{Eqn 2.65}$$
$$q(\rho) = \frac{n^2 - n_s^2}{n_1^2 - n_s^2}$$

with $R(\rho)$ and $dR(\rho) / d\rho$ continuous at $\rho = 0$ and $\rho = D$.

The solution of Eqn 2.64 is obtained as the solution of the variational problem which satisfies the stationary condition of the functional

$$I(R) = -\int_{-\infty}^{\infty} \left(\frac{dR}{d\rho}\right)^2 d\rho + \int_{-\infty}^{\infty} [v^2 q(\rho) - w^2] R^2 d\rho \qquad \text{Eqn 2.66}$$

assuming that $I[R]$ is stationary for $R(\rho)$ with slightly deviated function

$$R_{pert}(\rho) = R(\rho) + \delta\eta(\rho) \qquad \text{Eqn 2.67}$$

where δ denote as real small quantities and $\eta(\rho)$ is an arbitrary continuous function of ρ. Substitute Eqn 2.67 into Eqn 2.66 with the assumption that $I[R_{pert}]$ is stationary for $\delta = 0$.

$$\lim_{\delta \to 0}\{\frac{1}{2}\frac{\partial}{\partial\delta} I[R_{pert}]\} = -\int_{-\infty}^{\infty} \frac{dR}{d\rho}\frac{d\eta}{d\rho} d\rho + \int_{-\infty}^{\infty} [v^2 q(\rho) - w^2] R\,\eta d\rho = 0 \qquad \text{Eqn 2.68}$$

Eqn 2.68 can be rewritten as follows by partial integration

$$-[\eta\frac{dR}{d\rho}]_{-\infty}^{\infty} + \int_{-\infty}^{\infty} \left\{\frac{d^2R}{d\rho^2} + [v^2 q(\rho) - w^2] R\right\} \eta d\rho = 0 \qquad \text{Eqn 2.69}$$

Since $\eta(\rho)$ is an arbitrary continuous function of ρ, the first and second term of Eqn 2.69 independently should be equal to zero. Then $R(\rho)$ will satisfy the wave equation Eqn 2.64 and the boundary conditions of $dR(\rho) / d\rho$ are continuous and $\lim_{\rho \to 0} \frac{dR}{d\rho} = 0$. Besides, the solution should decays to zero at infinity. With this condition, the function $R(\rho)$ will make the Eqn 2.66 stationary and satisfy the wave equation Eqn 2.64 and the stated boundary.

Discretization of the Functional – Mesh

To simplify the calculation, the field profile in the core is discretized and expressed as

$$R(\rho) = \begin{cases} R_o \exp(w_o \rho) & (\rho < 0) \\ \sum_{i=0}^{n} R_i \phi_i(\rho) & (0 \le \rho \le D) \\ R_N \exp[-w(\rho - D)] & (\rho \ge D) \end{cases} \qquad \text{Eqn 2.70}$$

where R_o - R_N are field value at the sampling points and

$$w_o = a\sqrt{\beta^2 - k^2 n_o^2}$$

$$R_i = R(\rho_i) \quad \text{(i=0-N)} \qquad \text{Eqn 2.71}$$

$$\rho_i = \mathrm{i}\frac{D}{N} \quad \text{(i=0-N)}$$

The solution in the cladding and the substrate is easier and can be given by analytical functions. However, the sampling function ϕ_i becomes

$$\phi_0(\rho) = \begin{cases} \frac{N}{D}(\rho_1 - \rho) & (0 \le \rho \le \rho_1) \\ 0 & \text{all other areas} \end{cases}$$

$$\phi_i(\rho) = \begin{cases} \frac{N}{D}(\rho - \rho_{i-1}) & (\rho_{i-1} \le \rho \le \rho_i) \\ \frac{N}{D}(\rho_{i+1} - \rho) & (\rho_i \le \rho \le \rho_{i+1}) \\ 0 & \text{all other areas} \end{cases} \qquad \text{Eqn 2.72}$$

$$\phi_N(\rho) = \begin{cases} \frac{N}{D}(\rho - \rho_{N-1}) & (\rho_{N-1} \le \rho \le \rho_N) \\ 0 & \text{all other areas} \end{cases}$$

Note that the sampling function is a linear function of ρ, so Eqn 2.70 leads to the continuous function of R (ρ) being approximated by broken lines. The normalised refractive index distribution q (ρ) can be approximated by the sampling function.

$$q(\rho) = \sum_{\mathrm{i}=0}^{\mathrm{N}} q_i \phi_i(\rho) \qquad \text{Eqn 2.73}$$

$$q_i = \frac{n^2(\rho_i) - n_s^2}{n_1^2 - n_s^2}$$

Finally, substituting Eqn 2.70 into Eqn 2.66 allows the following functional to be obtained.

$$I = w_o R_o^2 - \int_0^v \left(\frac{dR}{d\rho}\right)^2 d\rho + \int_0^v [v^2 q(\rho) - w^2] R^2 d\rho - w R_N^2 \qquad \text{Eqn 2.74}$$

Dispersion Equation Based on the Stationary Condition – Computed

The stationary condition of the functional in Eqn 2.74 is given by partial differentiation with respect to R_i where (i = 0 – N) is

$$0 = \frac{1}{2}\frac{\partial I}{\partial R_i} = -w_o R_o \delta_{i,o} - \int_0^D \frac{dR}{d\rho}\frac{d\phi_i}{d\rho} d\rho + v^2 \int_0^D q(\rho) R \phi_i d\rho$$
$$- w^2 \int_0^D R \phi_i d\rho - w R_N \delta_{i,o} \quad (i = 0 - N) \qquad \text{Eqn 2.75}$$

The sampling function $\phi_i(\rho)$ is zero outside of the region $\rho_{i-1} \leq \rho \leq \rho_{i+1}$. Hence Eqn 2.75 can be broken into different regions

$$0 = \frac{1}{2}\frac{\partial I}{\partial R_i} = \quad -w_o R_o - \int_0^{\rho_1} (R_o \frac{d\phi_o}{d\rho} + R_1 \frac{d\phi_1}{d\rho}) \frac{d\phi_o}{d\rho} d\rho$$
$$+ v^2 \int_0^{\rho_1} (q_o \phi_o + q_1 \phi_1)(R_o \phi_o + R_1 \phi_1) \phi_o d\rho \qquad \text{Eqn 2.76}$$
$$- w^2 \int_0^{\rho_1} (R_o \phi_o + R_1 \phi_1) \phi_o d\rho$$

$$0 = \frac{1}{2}\frac{\partial I}{\partial R_i} = \quad - \int_{\rho_{i-1}}^{\rho_i} (R_{i-1} \frac{d\phi_{i-1}}{d\rho} + R_i \frac{d\phi_i}{d\rho}) \frac{d\phi_i}{d\rho} d\rho$$
$$- \int_{\rho_i}^{\rho_{i+1}} (R_i \frac{d\phi_i}{d\rho} + R_{i+1} \frac{d\phi_{i+1}}{d\rho}) \frac{d\phi_i}{d\rho} d\rho$$
$$+ v^2 \int_{\rho_{i-1}}^{\rho_i} (q_{i-1} \phi_{i-1} + q_i \phi_i)(R_{i-1} \phi_{i-1} + R_i \phi_i) \phi_i d\rho \qquad \text{Eqn 2.77}$$
$$+ v^2 \int_{\rho_i}^{\rho_{i+1}} (q_i \phi_i + q_{i+1} \phi_{i+1})(R_i \phi_i + R_{i+1} \phi_{i+1}) \phi_i d\rho$$
$$- w^2 \int_{\rho_{i-1}}^{\rho_i} (R_{i-1} \phi_{i-1} + R_i \phi_i) \phi_i d\rho$$
$$- w^2 \int_{\rho_i}^{\rho_{i+1}} (R_i \phi_i + R_{i+1} \phi_{i+1}) \phi_i d\rho \quad (i = 0 - N)$$

$$0 = \frac{1}{2}\frac{\partial I}{\partial R_N} = \quad - \int_{\rho_{N-1}}^{\rho_N} (R_{N-1} \frac{d\phi_{N-1}}{d\rho} + R_N \frac{d\phi_N}{d\rho}) \frac{d\phi_N}{d\rho} d\rho$$
$$+ v^2 \int_{\rho_{N-1}}^{\rho_N} (q_{N-1} \phi_{N-1} + q_N \phi_N)(R_{N-1} \phi_{N-1} + R_N \phi_N d\rho \qquad \text{Eqn 2.78}$$
$$- w^2 \int_{\rho_{N-1}}^{\rho_N} (R_{N-1} \phi_{N-1} + R_N \phi_N) \phi_N d\rho$$

The integrals of the sampling functions that exist in Eqn 2.76, Eqn 2.77, and Eqn 2.78 are given by

$$\int_{\rho_{i-1}}^{\rho_i} \frac{d\phi_{i-1}}{d\rho}\frac{d\phi_i}{d\rho}d\rho = -\frac{N}{D} \qquad (i = 1 - N)$$

$$\int_{\rho_{i-1}}^{\rho_i} \left(\frac{d\phi_i}{d\rho}\right)^2 d\rho = \frac{N}{D} \qquad (i = 1 - N)$$

$$\int_{\rho_i}^{\rho_{i+1}} \left(\frac{d\phi_i}{d\rho}\right)^2 d\rho = \frac{N}{D} \qquad (i = -N - 1)$$

$$\int_{\rho_{i-1}}^{\rho_i} \phi_{i-1}^2\phi_i \, d\rho = \frac{1}{12}\frac{N}{D} \qquad (i = 1 - N)$$

$$\int_{\rho_{i-1}}^{\rho_i} \phi_{i-1}\phi_i^2 \, d\rho = \frac{1}{12}\frac{N}{D} \qquad (i = 1 - N) \qquad \text{Eqn 2.79}$$

$$\int_{\rho_{i-1}}^{\rho_i} \phi_i^3 \, d\rho = \frac{1}{4}\frac{N}{D} \qquad (i = 1 - N)$$

$$\int_{\rho_i}^{\rho_{i+1}} \phi_i^3 \, d\rho = \frac{1}{4}\frac{N}{D} \qquad (i = -N - 1)$$

$$\int_{\rho_{i-1}}^{\rho_i} \phi_{i-1}\phi_i \, d\rho = \frac{1}{6}\frac{N}{D} \qquad (i = 1 - N)$$

$$\int_{\rho_{i-1}}^{\rho_i} \phi_i^2 \, d\rho = \frac{1}{3}\frac{N}{D} \qquad (i = 1 - N)$$

$$\int_{\rho_i}^{\rho_{i+1}} \phi_i^2 \, d\rho = \frac{1}{3}\frac{N}{D} \qquad (i = -N - 1)$$

Hence Eqn 2.76, Eqn 2.77, and Eqn 2.78 are a set of (N+1) ordered simultaneous equations having R_o-R_N as the unknown value. For simplification, these three equations can be written into a matrix form $[R_{1,N}][C_{N,N}]$ where C is given by

$$c_{0,0} = 1 - (3q_0 + q_0)\frac{v^2}{12}\delta^2 + \frac{w^2}{3}\delta^2 + w_o\delta$$

$$c_{i,i} = 2 - (q_{i-1} + 6q_i + q_{i+1})\frac{v^2}{12}\delta^2 + \frac{2w^2}{3}\delta^2 \quad (i = 1 - N - 1) \qquad \text{Eqn 2.80}$$

$$c_{i,i+1} = c_{i+1,i} = -1 - (q_i + q_{i+1})\frac{v^2}{12}\delta^2 + \frac{2w^2}{6}\delta^2 \quad (i = 0 - N - 1)$$

$$c_{N,N} = 1 - (q_{N-1} + 3q_N)\frac{v^2}{12}\delta^2 + \frac{w^2}{3}\delta^2 + w\delta$$

In order for Eqn 2.76, Eqn 2.77, and Eqn 2.78 to have nontrivial solutions except for $R_0 = R_1 = \ldots = R_N$, the determinant of matrix C should be equal to zero. i.e.

$$\text{Det (c)} = 0 \qquad \text{Eqn 2.81}$$

Eqn 2.81 is the eigenvalue equation for the TE-mode dispersion equation in an arbitrary refractive index profile. This equation can be solved if $q(\rho)$, v, w and w_o are given. Similarly, the analysis of the TM-mode will be similar to the above steps and will not be discussed.

FEM solutions are normally carried out using simulation programmes. In this work, COMSOL Multiphysics, which is a Graphic User Interfaced (GUI) programme, was used. The setup of a simulation model using COMSOL involved 3 steps. In the first step (mode setup), the structure of the waveguide is drawn out and subsequently, the material properties of each segment as well as other general parameter such as frequency of interest defined. In step 2, mesh size is selected to allow discretization to be undertaken. Usually smaller regions will need a higher mesh density to improve the simulation accuracy. By rule of thumb, the mesh size should be a sub-fraction of the wavelength of interest, or at least 2 to 3 nodes for every thin layer. Finally, in step 3, the software will automatically generate the mathematical source codes based on the user input and solve the problem based on FEM method. In conclusion, using commercial products such as COMSOL can significantly reduce potential confusion and debugging time associated with source code or equation based simulation software.

2.3.2 Finite Difference Method

Basic functions such as directional coupler, splitter, s-bend, and tapered are indispensable components in an integrated optical waveguide. In this structure the mode

coupling between parallel, closely spaced waveguide (described by coupled mode theory) need to be taken into consideration to evaluate propagation characteristics. The FEM stationary mode analysis method described in section 2.3.1 is not suitable to analyse wave propagation in this situation, while the Beam Propagation Method (BPM) is the most suitable technique for this structure. BPM is also useful in regards to short pulse propagation in waveguides. In general, BPM has two common procedures, these being based on Fast Fourier Transform (FFT) and finite difference method.

The basis of BPM lies in the Helmholtz equation,

$$\frac{\partial^2 E}{\partial x^2}+\frac{\partial^2 E}{\partial y^2}+\frac{\partial^2 E}{\partial z^2}+k^2 n^2(x,y,z)E=0 \qquad \text{Eqn 2.82}$$

where the electric field E (x, y, z) can be separated into two parts; the axially slow varying envelope term of ϕ (x, y, z) and the varying term of $exp(-jkn_o z)$. The term n_o refers to the refractive index of the cladding.

$$E(x,y,z)=\phi\,(x,y,\mathrm{z})\exp(-jkn_o z) \qquad \text{Eqn 2.83}$$

Further simplification can occur by assuming a weakly guiding condition where $(n^2-n_o^2)\cong 2n_0(n-n_0)$, Hence the Helmholtz equation can be simplified to

$$\frac{\partial \phi}{\partial z}=-\frac{j}{2\mathrm{k}n_o}\nabla^2\phi-j(n-n_0)\phi=0 \qquad \text{Eqn 2.84}$$

Both right hand side terms affect the light propagation simultaneously with the first term representing the waves propagating in a medium having a refractive index of n_o, and the second term represents the guiding function of the region having a refractive index of n (x, y, z). This concept is applied in BPM analysis where the wave is first analysed in regards to propagation in free space (refractive of n_o), and the phase retardation caused by the guiding function is only afterwards taken into account. Hence light propagation within various kinds of waveguide can be analysed by repeating this same procedure many times. Additionally, a term $-\alpha\phi$ can be added on the right hand side of Eqn 2.84 to take into consideration the optical loss or gain of the wave in the

waveguide. Due to the weak guiding assumption, BPM is inaccurate in high index contrast waveguides such as silicon photonics.

Two approaches can be used to solve Eqn 2.84. The first approach is to apply integration on the equation, followed by fast Fourier transform (or discrete Fourier transform). The second approach involves the finite difference method, where the partial difference equation is transformed into a series by discretizing the z-axis into many small segments. In the second approach, known as Finite Difference Time Domain (FDTD) method, the time factor can be included to study the evolution of the wave (or pulse) in the waveguide in a given time. Again there is commercial available software that builds based on BPM. The most famous BPM software in optical waveguides is Rsoft BeamPROP. The exactly same three basic steps as in FEM are needed in using Rsoft.

BPM has the ability to provide solutions for optical components with very large area size. The computational time required for even a few mm length device is minimum especially in two-dimensional. However, BPM has a limit in analysis of complex cross-sectional waveguide structures. In this case, the effective index of the complex structure can be calculated by FEM, in which this region is represented by a simple rectangular core with the refractive index properties obtained from FEM. Hence, the three-dimensional complex problem can be reduced to a simple two-dimensional problem (the cross-sectional energy distribution (mode) of the waveguide can be ignored), where the user can focus only on the parameters relating to optical component design.

References

1. K. Okamoto, Preface to the second edition, in: K. Okamoto (Ed.) Fundamentals of Optical Waveguides (Second Edition), Academic Press, Burlington, 2006, pp. xv-xvi.

2. D.K. Cheng, Fundamentals of Engineering Electromagnetics: Addison-Wesley Publishing Company; 1993.

3. R.G. Hunsperger, Integrated Optics: Theory and Technology: Springer; 2009.

4. D.K. Mynbaev, L.L. Scheiner, Fiber-optic Communications Technology: Prentice Hall; 2001.

5. F.L. Pedrotti, L.S. Pedrotti, Introduction to Optics: Prentice Hall; 1993.

CHAPTER 3: SAMPLE FABRICATION AND CHARACTERIZATION

In this chapter, polymer waveguide fabrication process is discussed. In order to fabricate a high quality waveguide, process parameters in each step need to be considered thoroughly. A dust-free fabrication environment is needed to produce high quality waveguide. Selection of materials used as substrate, underclad, core and overclad of the waveguide are also important to produce a good quality waveguide. Material properties needed and their corresponding restrictions on the fabrication process for each layer are discussed. It is then followed by the availability of materials in the market that fulfil most of the criteria. The waveguide fabrication process will then be discussed. Singulation of the fabricated waveguide samples through dicing and polishing will then be discussed. This is followed by the discussion on characterization methods of the fabricated waveguide layers after each process steps. The last 2 sections of this chapter focus on optical characterization of the fabricated optical waveguides.

3.1 Fabrication Environment

To produce good waveguides, fabrication environment must be taken into consideration seriously. Dust particles on the sample during the fabrication process such as photolithography can cause a permanent defect on the fabricated waveguide sample. As devices become smaller, the requirements for contamination control become higher. Therefore, a clean room is required. A clean room is a room in which the concentration of airborne particle is controlled. A clean room must be controlled and monitored very closely from construction to operation. Temperature, humidity, and particle count measurements must be conducted periodically to ensure the clean room is working properly according to the standard required. The clean room must be cleaned frequently with alcohol wipes and special vacuum cleaner. Every clean room user is required to wear

lint-free clean suits, overshoes, glove, hair cover and mask in the changing room and go through the air shower before entering the clean room.

The clean room in Photonic Research Centre, UM is a class 10k (US FED STD 209E) clean room, where the number of particles with size smaller than 0.1 μm are controlled to less than 10 thousand per cubic meter. The temperature of the clean room is controlled between 20 ^{o}C to 23 ^{o}C with humidity controlled in the range of 45% to 55%. A yellow room was also built within the main clean room area. This room is specially allocated for the photolithography process where the light used is UV-free. In addition, there are a number of facilities installed in the clean room which include spin coater, surface profiler, prism coupler and mask aligner.

3.2 Choice of Waveguide, Substrate, and Overclad Materials

The selection of optical waveguide materials are dictated by the optical properties of the materials. The waveguide core materials must have a very low optical propagation loss (at lease less than 1 dB/cm) in the wavelength range of interest - from 650 nm to 1630 nm. Besides, it would be a value-add if the material itself is photosensitive to ultraviolet (UV) light because no additional photoresist coating and etching process are required during the waveguide fabrication. Likewise, the underclad (can be the substrate itself in some cases) and overclad materials must have low loss at the optical wavelengths of interests and additional characteristics that suits the waveguide material processing conditions. The following sections discuss the materials that will be used in the fabrication of optical waveguide in this work.

SU-8 as Waveguide Material

One of the materials that is suitable as waveguide material is SU-8 from Microchem. SU-8 is an epoxy based negative resists, which can be spin-coated to produce a thin film on a planar substrate with thickness ranging from 1 μm to 300 μm by controlling its viscosity and spin speed. Due to its relatively high transparency to UV light, microstructures with high aspect ratio of > 20 have been fabricated from SU-8 using photolithography techniques [1]. Initially, SU-8 was developed for microelectronics industry and bio-MEMS, due to its biocompatibility and high aspect ratio. Later, SU-8 is also found suitable to be used as optical waveguide material because it exhibits a flat transmission response of more than 95% from 500 nm to more than 1600 nm as shown in Figure 3.1. Refractive index of SU-8 at 1550 nm is reported to be in the range between1.570 to 1.575 [1-3]. However, measurement of refractive index of a 6.93 μm thick SU-8 film using prism coupler produced a value of 1.566 as shown in Figure 3.2, which is slightly lower than the values reported. We believed that the discrepancy is the effect of different processing parameters (hard bake of SU-8 film at lower temperature), which will be further discussed in the next section). Using SU-8 as optical waveguide material has been reported in [3-5] with low optical loss of less than 1 dB/cm being achieved.

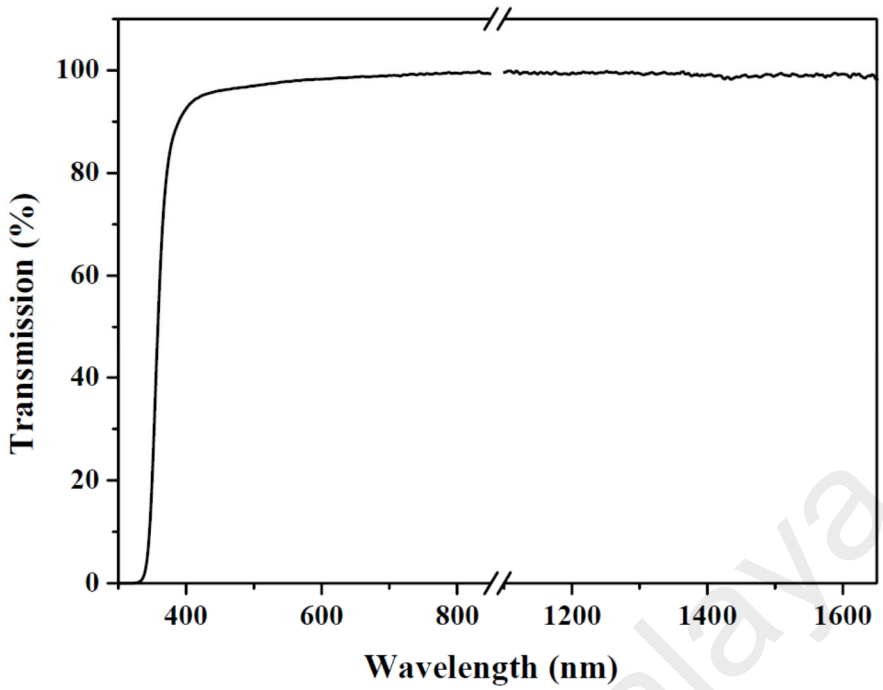

Figure 3.1: Transmission spectrum of SU – 8 after cure. [1]

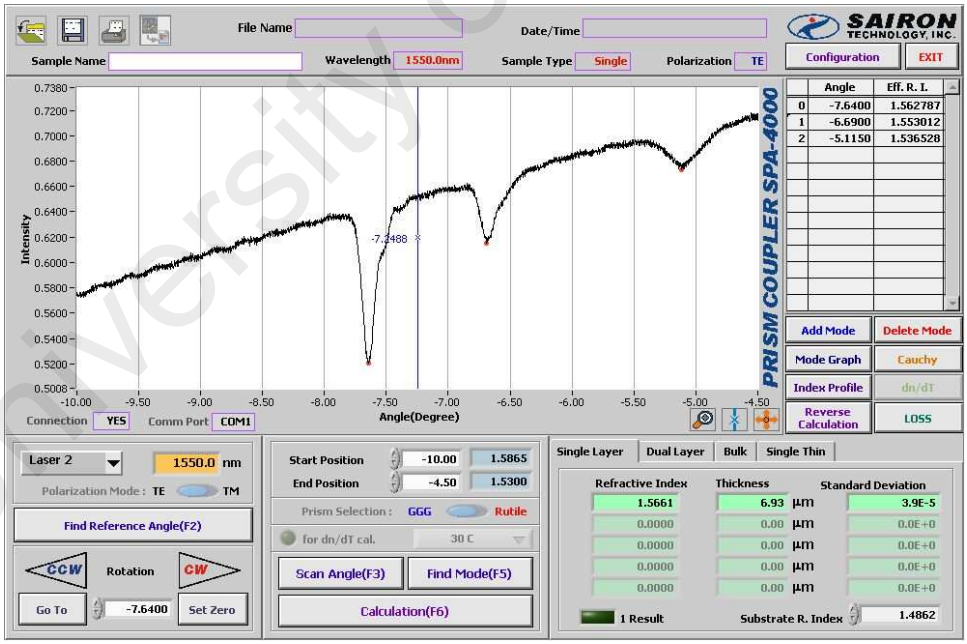

Figure 3.2: Screenshot of refractive index measurement of SU-8 at 1550 nm on CR-39 using Sairon SPA 4000 prism coupler.

Fabrication of SU-8 waveguide involves UV exposure and subsequent chemical development of the spin-coated SU-8 film, followed by a hard bake process step at temperature of 100 ^{o}C is required [6]. Therefore, the substrate materials to be used in SU-8 waveguide fabrication must have the following characteristics:

- lower refractive index than SU-8,
- low optical loss at the wavelength of interest,
- higher softening temperature than 100^{o}C,
- stable to UV exposure, and
- chemically stable to SU-8 developer and other processing chemicals.

Two approaches have been used to provide the above mentioned requirements. The first being the use of CR-39 as substrate material, while the second is the use of silicon wafer as substrate material with a sufficiently thick layer of Benzocyclobutene (BCB) coated on the silicon wafer as underclad buffer.

Allyl Diglycol Carbonate as Substrate

Allyl Diglycol Carbonate (CR-39) is a plastic material developed in the 1940s and was first used as transparent gauge tubes in aircraft. A few years later, CR-39 expended its application in eyeglass lenses and it became a trademark product of PPG industry. CR-39 plastic has a refractive index of 1.498 with an Abbe number of 59.3. Abbe number, V_D is a measure of material's dispersion,

$$V_D = (n_D - 1) / (n_F - n_C) \qquad \text{Eqn 3.1}$$

where n_D, n_F and n_C are the refractive index of the material at Fraunhofer D (589.3 nm) , F (486.1 nm) and C (656.3 nm) spectral lines. The refractive index of CR-39 at 1550 nm is 1.4862 measured using prism coupler as shown in Figure 3.3. CR-39 has the highest scratch resistance among other uncoated plastics, strong chemical resistance and aging resistance, which make it a suitable substrate material for waveguide applications [7].

However, there are drawbacks in using CR-39 as waveguide substrate. Firstly, its continuous handling temperature is limited to 100 ^{o}C, (or 130 ^{o}C for an hour). This gave rise to the need for a minor adjustment in the processing temperature of SU-8. Besides, the CR-39 plastic may experience "bowing" when subjected to a sudden change in temperature, i.e. during the soft bake process of SU-8. Hence, extra load is required to be applied on to the side of the SU-8 sample to compensate the "bowing" effect.

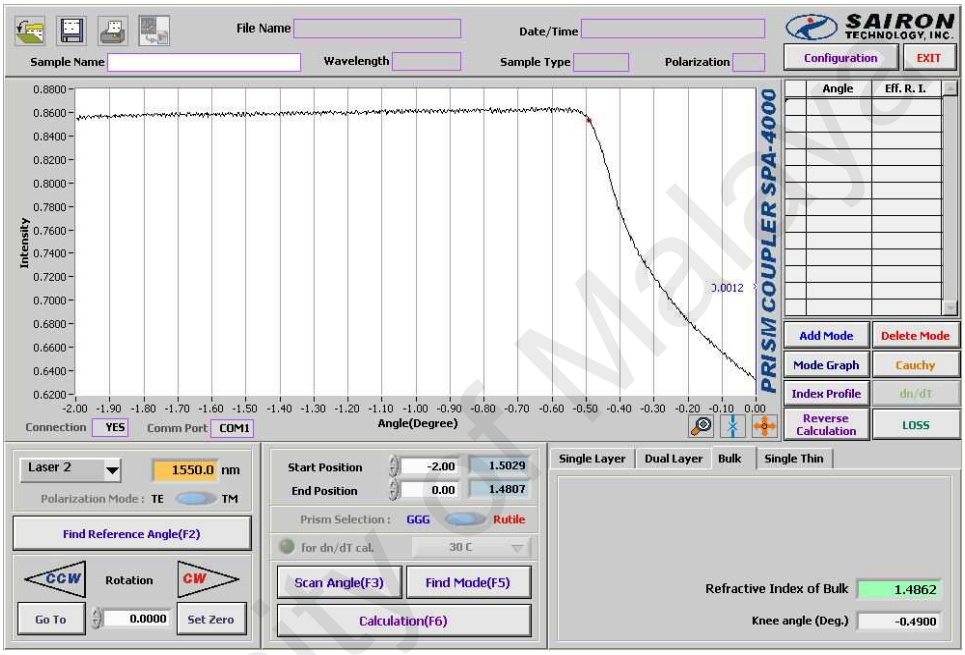

Figure 3.3: Screenshot of refractive index measurement of CR-39 using Sairon SPA 4000 prism coupler.

BCB 4024 on Silicon as Substrate

Benzocyclobutene (BCB) is an advance electronic resin product developed by Dow Chemical Company as dielectric insulating layer in microelectronic application. BCB has a refractive index of 1.545 to 1.56 at 1550 nm depending on its curing condition [8]. The use of BCB itself as the core material for waveguide application has been demonstrated in [8-13]. However, due to its relatively high material loss in telecommunication band, most of the fabricated waveguides have a propagation loss of > 2 dB/cm. Besides, BCB requires high curing temperature in an oxygen free environment, which resulted in SU-8

replacing BCB as the preferred material in waveguide application since the year 2005. However, applying BCB on silicon wafer as the underclad of a waveguide provides several advantages. Firstly, the refractive index contrast between BCB (1.54) and SU-8 (1.56) is only about 0.02 which is relatively lower than CR-39 – SU-8 which is 0.08. Lower index contrast allows larger core size for single mode operation and lower coupling loss. Secondly, as silicon wafer is a crystalline material, "cleave and break" technique can be used to produce a flat end-facet during singulation of individual waveguide devices after the waveguide fabrication process without the need of polishing. In other words, the "break" surface, although not optically flat, is good enough for efficient light coupling. Moreover, it refractive index is closer to that of NOA optical adhesive, which will be used as the overcladding material.

NOA UV Rasin as Overcladding

Overcladding materials need to fulfil extra requirement other than those mentioned earlier. Firstly, it must have a lower processing temperature, and the chemicals used in its processing must not affect the core and undercladding layer physical integrity as well as optical properties. Among many materials, NOA UV resin from Norland co. ltd. is one of the suitable choices. NOA UV resin has been used in fibre to waveguide bonding. It has the advantage of set cure in seconds when exposed to UV light. Besides, it has a series of products with different refractive indices ranging from 1.37 to 1.56 – measured at visible wavelength [14]. It is worth noting that NOA UV resin has a shelf life of only 1 year, after which the refractive index of an expired NOA UV resin will reduce slightly compared to "fresh" NOA UV resin. For example, the refractive index of fresh (expired) NOA 68 measured at 1550 nm is 1.5244 (1.5177) after UV curing. This change in refractive index over time need to be taken into consideration. However, NOA UV resin that was fully cured do not exhibit this change over time. The transmission spectrum of

NOA 65 is shown in Figure 3.4, taken from NOA datasheet [14]. It has a flat transmission of more than 95% spanning from 0.4 μm to about 2 μm. Although it is stated in the datasheet that when exposed to sufficient UV fluence the NOA resin can be fully cured, the resin is still physically sticky and soft, especially for NOA 65. Therefore, hard bake is necessary to further strengthen the resin. The hard bake process is simple - by placing the sample in an oven at 80 ^{O}C for 4 hours. NOA UV resin has also been used as waveguide materials as in [15-19].

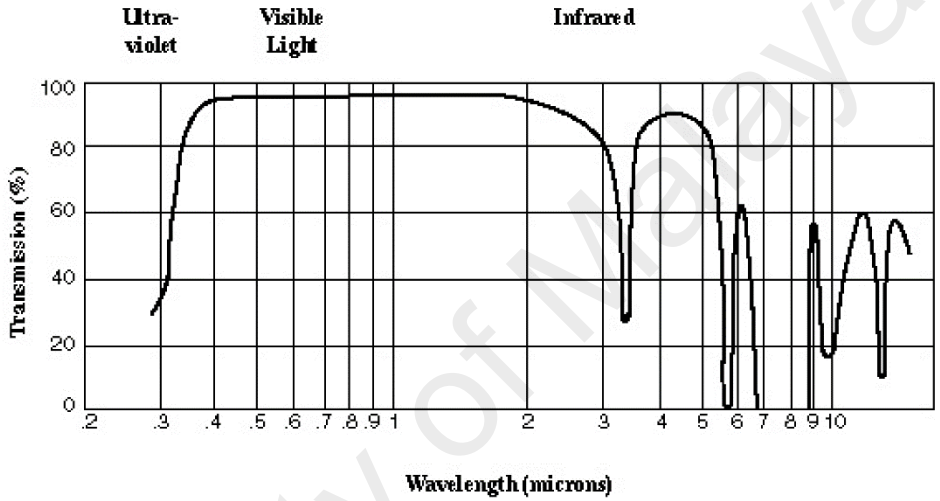

Figure 3.4: Transmission spectrum of NOA 65 UV resin. [14]

3.3 Substrate Preparation and Cleaning

Figure 3.5 shows the overall waveguide fabrication process flow. The process begins with substrate preparation and cleaning. Substrate preparation and cleaning are important, dirty substrate surface may produce wrinkled layer after spin coating that will lead to high optical loss or adhesive problem that may cause the waveguide channels to peel off during the fabrication process. The CR-39 sheet used as substrate is 1 mm thick. It is optically polished as purchased with protective layers on both surfaces. The protective layers were carefully removed, follow by cleaning using standard cleaning procedures. The standard cleaning procedure is rinsing using acetone, IPA, DI water followed by drying using nitrogen gas blower. The same cleaning procedures were

applied to the silicon wafer as well, followed by BCB undercladding spin coating and subsequent hard bake at 240 ºC for 1 hour.

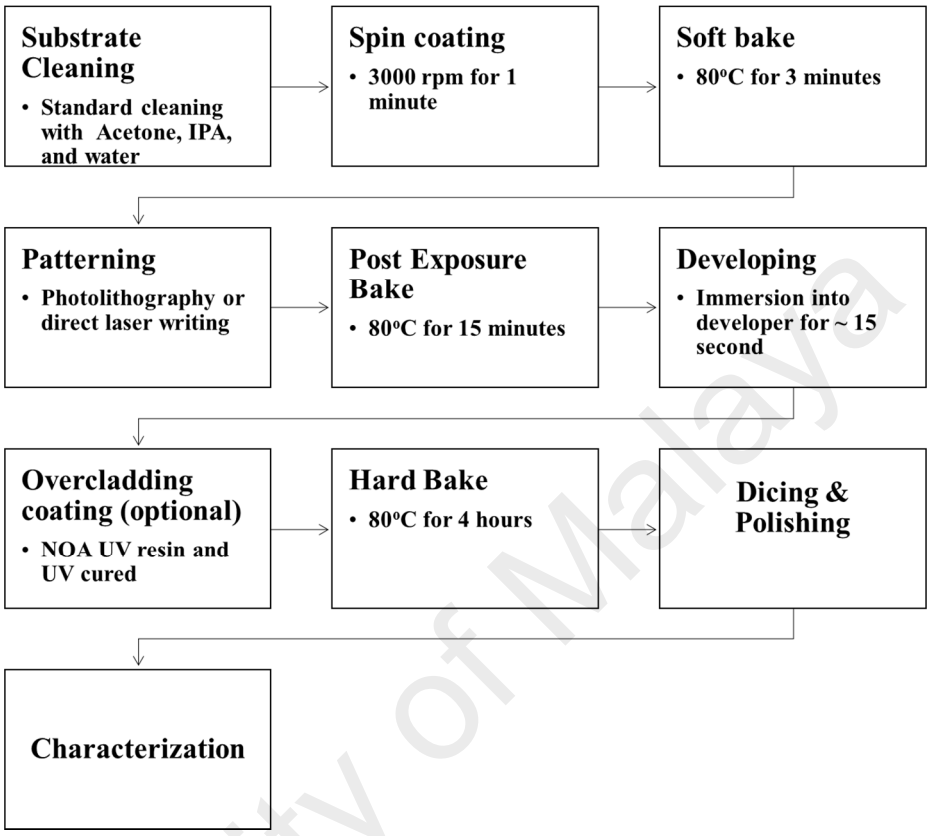

Figure 3.5: Summary of waveguide fabrication process flow.

3.4 Photolithography

Photolithography is a technique of transferring pattern of geometrical shapes on a photomask to a thin photosensitive layer of known as photoresists (here refer to SU-8) that is usually spin-coated onto a substrate. The following process steps are mainly based on the SU-8 processing guide [6] with minor modification especially on processing temperature, limited by the CR-39 sheet.

3.4.1 Spin Coating

Spin coating is a proven method for coating liquid based materials onto a large planar surface area uniformly. The thickness of the coated film can be very thin (submicron) with uniformity as good as 5 Å [20]. This coating method requires low start-up cost and is fast, consistent and easy to handle. The thickness of the film deposited using this method depends on the viscosity of the photoresist, spin time and spin speed (inversely proportional to the square root of the spin speed). Hence the film thickness can be easily controlled by the spin speed. However, the spin speed must not be slower than 1000 rpm. This is because the surface of the photoresist will not be smooth. The film surface smoothness is proportional to the spin speed. The only disadvantage of using the spin coating method is that this approach is not environment friendly. This is because more than 90% of the photoresist will be wasted in the spin coating process and the photoresist is a hazardous material [21, 22].

Like most photoresist materials, both SU-8 and BCB need to be stored at refrigerated temperature below 15 ^{o}C. Prior to spin coating process, the photoresists needs to be warmed up to room temperature. This is because the viscosity of the photoresist is temperature dependent. Using a pipette, a few ml of SU-8 was dispensed onto the substrate surface that was earlier placed on the spin coater. The pipette must be held as near as possible to the centre of the substrate to reduce the occurrence of trapped air bubble or dust during the process. Air bubbles or dust trapped in the SU-8 are causes defects in the fabricated waveguide channels. The substrate was then accelerated slowly to 500 rpm in 10 seconds with 50 rpm/second ramp up speed. The purpose of this stage is to spread the SU-8 evenly on the substrate surface and the ramp up speed need to be slow in order to provide the SU-8 sufficient time to spread and cover the entire substrate surface area. Then the substrate was spun at 3000 rpm for 1 minute with a ramp up time

of 10 seconds. During the second stage, the photoresist will undergo a thinning process due to centrifugal forces [23]. Finally, the rotation speed was ramped down to 0 rpm with a 10 second ramp down time.

3.4.2 Control of SU-8 Thickness

The SU-8 polymer used in this work was SU-8 2002 series with a spin speed dependent coating thickness of 3.6 μm (1000 rpm), 3 μm (2000 rpm), to 2.9 μm (3000 rpm) [1]. However, in waveguide fabrication, a thickness beyond this range maybe needed. Hence, methods of controlling the coating thickness by increase or decrease the viscosity and density have been developed.

To increase the coating thickness, the viscosity of the SU-8 solution was increased. To achieve this, the content of solvent in SU-8 needs to be removed without altering the characteristics of the SU-8 monomer and photo-initiator. It was found that by heating up the SU-8 solution to 130 ^{o}C with continuous stirring at 600 rpm, the SU-8 solvent will evaporate while there were no observable changes to its photosensitivity. With 1 hour of heating and stirring, a spin-coated SU-8 film with 5 μm thickness was obtained with a spin speed of 3000 rpm.

To decrease the coating thickness, additional volume of solvent was added to the SU-8 solution at a given ratio. The solvent for SU-8 is Cyclopentanone and the coating thickness of both SU-8 2002 and SU-8 2010 series can be reduced as shown in Figure 3.6. However, in some photoresists, the monomer structure might be larger and attempts to decrease the coating thickness via dilution of the photoresist may compromise the resolution in pattern transfer during photolithography process. Hence, dilution of photoresist by more than 30% is not advisable unless the resolution is not a concern.

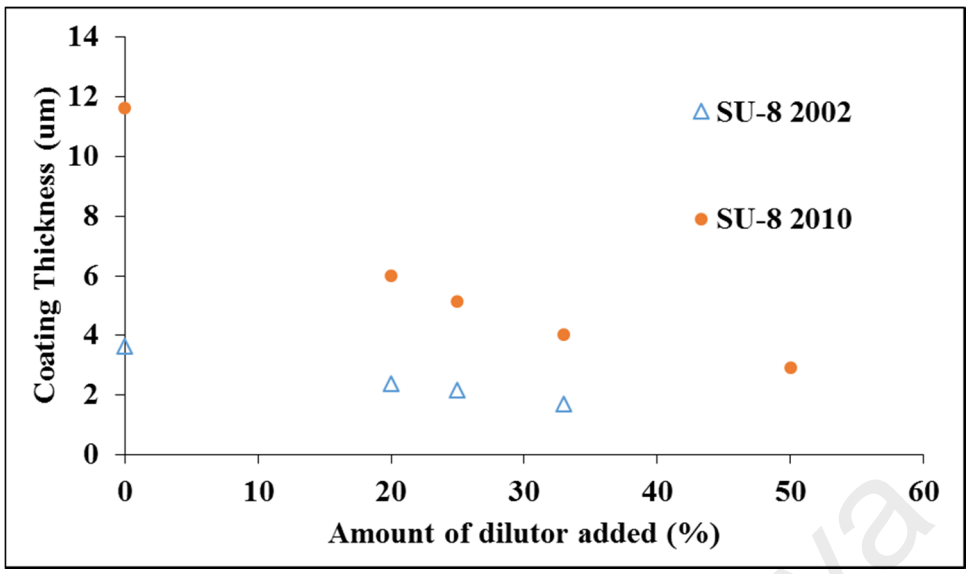

Figure 3.6: SU-8 coating thickness with respect to amount of dilutor (Cyclopentanone) added.

3.4.3 Soft Bake

After the spin coating, the sample will undergo soft bake. The purpose of this process is to reduce the solvent content in the SU-8 layer and increase its adhesion to the substrate [20]. Soft bake temperature and time are critical. The SU-8 film cannot be too "dry" because this will reduce the photosensitivity of the SU-8 film and eventually reduces the resolution [24]. The SU-8 film will be difficult to be developed or removed completely if it is over-baked. On the other hand, under-bake film will have very high solvent content which may cause the SU-8 film to stick on the photomask during photolithography process as well as reduces the resolution of photolithography process due to spatial diffusion of photo-initiators upon UV exposure [6]. Hence, soft bake time is important and need to be optimized to achieve straight and near vertical sidewall profile [25]. This baking process can be done by using an oven or hot plate. However, hot plate is preferable due to its nature of bottom-heating, allowing solvent in the SU-8 film to evaporate through its surface. The optimum temperature for soft bake process is 80 ^{o}C with 3 minutes of baking time. After the soft bake process, the sample must undergo UV

exposure in the photolithography process immediately to avoid uncertainties due to changes in solvent content over time.

3.4.4 UV Expose and Patterning

Pattern transfer was carried out using a UV mask aligner system. The UV mask aligner system is equipped with a 4-axis sample alignment stage that allows the sample to be aligned in the 3 linear axes as well as controlling its tilt angle relative to the photomask to ensure good pattern transfer from the photomask to the SU-8 film. The UV light source is a high vapour pressure mercury arc lamp. The mercury lamp has a multiple lines emission from 275 nm to 650 nm with peak emission at 365 nm (I-line). This wavelength is used to crosslink the photoresist. A mechanical shutter is in place to control the exposure time of the photolithography process. The arrangement of the UV mask aligner is as follow: the mercury arc lamp is located at the top of the mask aligner, followed by the mechanical shutter, photomask, sample, sample alignment system. The photolithography used in this work was contact-type, meaning that the sample was aligned to make physical contact with the photomask. They are two built in function in the alignment system to make a good contact between the photomask and the sample. There are vacuum contact and hard contact. Hard contact uses physical force to push the sample towards the photomask while vacuum contact uses a vacuum pump to remove all the air between the photomask and sample so that they will contact closely. Usually vacuum contact will result in better resolution in pattern transfer, but it may easily cause permanent scratch on the photomask as compared to hard contact. Due to this reason vacuum contact is usually applied to smooth surfaces only. The function of the shutter is to control the dosage of UV irradiation onto the sample by controlling its opening time. The shutter opening time can be controlled in the range between 0 to 999 second with an

interval of 0.1 second. The total exposes time is determined by the intensity of the UV light at the sample position and the UV dosage required by the photoresist.

In SU-8 processing, a 10 second exposure to 27 mW of UV light is sufficient for the process. During the exposure process, the triarysulfonium hexafluoroantimonate salt serving as a photo-acid generator is decomposed and generate a strong acid. This strong photo-acid then diffused to the SU-8 monomer and initiates cationic polymerization by the opening of the epoxy ring. The formation of crosslink takes place if another epoxy group is available due to diffusion and rearrangement of the monomer or polymer cluster [6]. As has been discussed in the previous section, the rate of diffusion is dependent on the film “dryness” which is controlled by the soft bake process.

3.4.5 Post Exposure Bake (PEB) and Developing

Negative tone resists usually requires PEB before chemical development process. The PEB temperature is identified as the most important process parameter influencing the residual stress in thin photoresists film [6]. Basically, in PEB, the photoresists film undergoes further drying that halt the diffusion of photo-acid. If the PEB is too rapid, the photo-acid may not have sufficient time to induce cross-link over the entire UV exposed area which is supposed to remain after chemical development. This will cause under-cut during chemical development which may lead to complete wash out of the pattern structure. On the other hand, if PEB is too long, the diffusion of photo-acid process may extend into area not exposed and results in the broadening of the pattern structure. It was also found that all the 3 processes – soft bake, UV exposes and PEB are interrelated and a change in 1 parameter can be compensated by the other 2 parameters. For example, if soft bake temperature or time is increased, this will reduce the film solvent content and hence a higher UV exposure dosage is required followed by shorter PEB. The optimum

PEB process parameters with the optimum soft bake and UV exposure dosage, were 80 ^{O}C for 15 minutes. After PEB process, due to the densification of the cross-linked area, pattern can be observed by bare eye.

Finally, the samples will undergo chemical development process. In industrial practices, the chemical development process involves dispensing the chemical developer onto the sample that is being rotated continuously for a duration of a few ten seconds. However, to reduce the usage of chemical developer, the sample was immersed in a small beaker containing chemical developer for about 15 seconds. The immersion duration is critical. If the developing time is too short, the unwanted area may not be completely removed, while too long will cause jagged edge in the produced channel or complete wash out of the channels due to undercut process. After the chemical development process, there will be photoresist residue in the form of monomers in the chemical developer which may re-deposit onto the sample surface that causes surface contamination. For photoresist that is soluble in water (i.e. AZ product from Microchem), De-Ionised (DI) water was used to clean the developed sample followed by drying using compressed air. However, in the case of SU-8 which is not soluble in water, cleaning can only be done using the developer itself. Hence the cleaning process for SU-8 is critical and removal of the produced channels by the cleaning developer need to be avoided. In practice, the immersion time during the cleaning process was reduced to about 10 seconds followed by one repetition.

3.5 Overcladding Coating

Coating of overcladding is an optional process, the patterned SU-8 may undergo the hard bake process directly before or after overcladding coating. However, coating of overcladding before hard bake process was preferred to reduce the total fabrication time.

Furthermore, exposure of patterned SU-8 waveguide structure to ambient environment especially in an air-circulation oven may result in dust sticking onto the SU-8 waveguide which will induce extra insertion loss to the fabricated waveguide device. The overcladding coating process involves first applying the NOA resin onto the sample surface, which was then covered by a second piece of CR-39 sheet to sandwich the NOA resin covered waveguide structures. This top CR-39 sheet was not part of the light guiding structure, but served to strengthen the structural integrity of the waveguide device and protects the waveguide structures from physical damage during subsequent polishing process. The top CR-39 need to be placed carefully to avoid trapping of air bubbles on the sample. Air bubbles in contact with the waveguide will cause a change in the local effective index, acting as a scattering point and hence create a high insertion loss in that particular area. Finally, the sample was again exposed to UV light to cure the NOA resin.

3.6 Hard Curing

SU-8 has good mechanical properties. A hard bake process was added to ensure that SU-8 properties do not change over time. This is because SU-8 is a thermal resin where its properties can continue to change when exposed to higher temperatures than that previously encountered. However, waveguide application in lab environment was always controlled at room temperature. Hence curing of SU-8 at temperature above 50 ^{o}C is more than sufficient. In practice, we applied hard bake process by heating the sample at 80 ^{o}C for 4 hours – this is because some NOA required longer thermal curing time to stable.

3.7 Dicing and Polishing

After the successful fabrication of a waveguide device, dicing and polishing of the input/output end facets was carried out before light can be coupled in and out of the

waveguide device. A good polishing surface will result in a lower coupling loss. The polishing quality becomes more critical when the core size or wavelength is reduced. A good polishing surface, known as optically flat surface, will have a roughness in a fraction of the operating wavelength which is in the sub-micron scale for our application. The quality of a polished surface can be assessed by observation under an optical microscope. The polished surface should have minimum scratches as shown in Figure 3.7d.

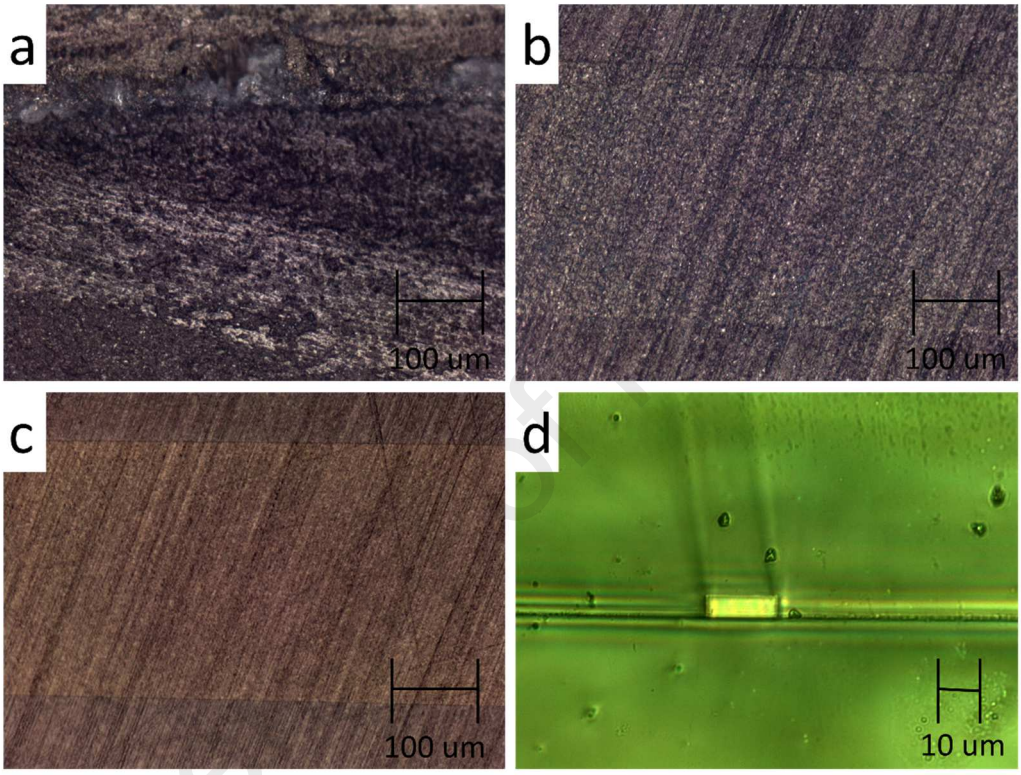

Figure 3.7: Microscope images of waveguide end facet after a) dicing, polished using b) 15 µm, c) 9 µm, and d) 0.3 µm polishing films – the bright rectangular at the centre is the waveguide core.

3.8 SU-8 Film Characterization

As waveguide fabrication process involved many process steps, it is necessary to evaluate the performance at different process steps in order to produce waveguide devices with the desired performance. In addition to the characterization of the fabricated waveguide device performance, the characteristics of the spin-coated film and the

physical properties of waveguide structures were also measured. There were 3 characterization tools used for these purposes. They are prism coupler, surface profiler and microscope.

Prism Coupler

Prism coupling technique was used to study the optical characteristics of SU-8 film such as refractive index, film thickness and material loss. The prism coupler used in this work was a model SPA-4000 from Sairon Tech Inc. The operation principle of prism coupler is shown in Figure 3.8. In a prism coupling setup, light is coupled into a thin film sample via a prism with refractive index higher than the measured film. With various light incident angles, a series of continuous incident light with different wave vector can be excited. However, due to quantize property of propagation constant of the guided light in the film, only incident light with wave vector equal to the guided mode propagation constant can be coupled into the testing film. By measuring the reflected power with a photodiode for various incident angles, the wave vector with corresponding guided mode propagation constant can be measured. With this information, the refractive index and the thickness of the thin film can be calculated [26, 27]. Figure 3.2 shows an example of a refractive index measurement of SU-8 on CR-39 substrate. However, if the measured film is too thin - thickness smaller than 3 guiding modes, only refractive index can be measured. In practice, at least 3 guiding modes are needed to calculate the refractive index and film thickness simultaneously. Likewise, for a bulk layer, for example a substrate with thickness of > 100 μm, only refractive index can be measured as shown in Figure 3.3.

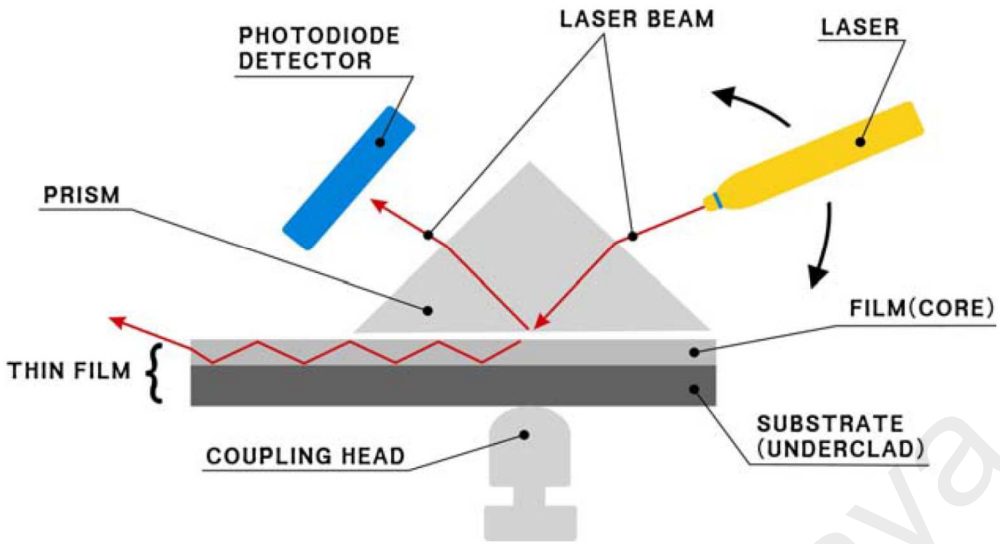

Figure 3.8: Operating principle of prism coupler.

When silicon wafers were used as substrate material, a thick undercladding layer was first coated on the substrate before the core layer coating. The undercladding layer acts as an optical buffer to prevent the light leakage into the silicon substrate which has a very high refractive index (3.40 at 1550 nm). In this case, the film structure will be a dual layer thin film. Refractive index and thickness of both layers can also be measured using prism coupling technique as well as shown in Figure 3.9. The first deeper dip on the left corresponds to the fundamental propagation mode of the SU-8 core. The second dip, which is the shallowest, and subsequent dips are the cladding propagation modes in the BCB undercladding. In this case, the SU-8 core thickness is thin enough that only 1 propagation mode is supported. The drawback of prism coupler is that the surface quality of the film must be optically flat. A rough surface will cause an air gap between the prism and the sample surface which will disrupt light coupling. This will cause a high error in measurement. Moreover, the prism may be damaged by the physical contact with rough sampler surface. Besides, the thin film might not be well cured, applying high pressure to push the sample contact with prism might cause some polymer stick on the prism which will then cause a high error in measurement.

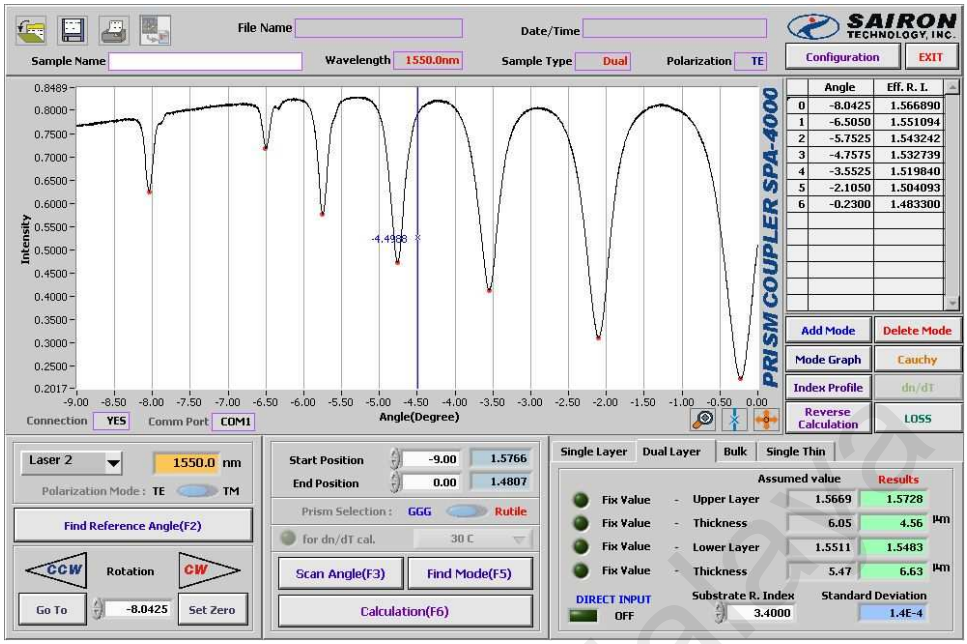

Figure 3.9: Screenshot of prism coupling spectrum measurement using Sairon SPA 4000 prism coupler and its corresponding refractive index and thickness of SU 8 - BCB dual layers on silicon substrate measured at 1550 nm.

The prism coupler can also be used for thin film propagation loss measurement. By dipping the sample into high refractive index fluid, the guided mode will be leaked out of the core layer. By measuring the leaked light intensity with respect to the length of sample dipped into the high refractive index fluid, the optical loss of the thin film can be measured [28]. Figure 3.10 (the blue line) shows an example of this propagation measurement on SU-8 – BCB dual layers film on silicon substrate.

Figure 3.10: Screenshot of propagation loss measurement (blue line) of SU-8 – BCB dual layers film on silicon substrate. The green line is another detector measurement for system referencing.

Surface Profiler and Microscope

After the patterning of the waveguide channel, it was necessary to measure the dimension and cross sectional profile of the waveguide channel as well as its surface roughness. For channel inspection (to determine whether the waveguide channel is in good condition without any breakage) and channel width measurement, optical microscope was used. To measure the surface roughness and channel height, surface profiler was used. The surface profiler used in this work is a Dektak 150 stylus-based profiler with a pin radius of 4 μm. The pin radius will limit the feature size that can be measured. For example, a 4 μm radius pin cannot be used to measure a "valley" that is narrower than 4 μm. The advantage of surface profiler is its very high vertical measurement resolution with a precision of 1 nm provided the profiler is placed in a vibration isolation table. Besides, as it is a contact type profiler, the force exerted by the stylus tip on the sample surface is very large, where soft material may be scratched by the profiler tip.

3.9 Fibre Coupling and Optimization

In order for a waveguide device to be useful, light needs to be coupled into and out of the waveguide device. Light coupling can be achieved either using free space objective lenses or optical fibre butt-coupling. Both methods require optical alignment between the waveguide device and the coupling elements. As most if not all waveguide devices are used in an optical fibre network, fibre butt-coupling method was used in this work. It involves the alignment between the input optical fibre and the input of waveguide device and between the output of the waveguide device with the output optical fibre. The figure of merit of a connectorised waveguide device is insertion loss,

$$Insertion\ \ loss = \sum(Loss_{MFD} + Loss_{NA} + Loss_{Fresnel}) \quad \text{Eqn 3.2}$$

There are many factors that contributed to the insertion loss of a waveguide device. Some factors are avoidable such as misalignment, and surface polishing quality. Reduction of waveguide losses, on the other hand, are not as straight forward. In general, these losses are core size mismatch, mode field diameter mismatch, NA mismatch, and Fresnel reflection loss due to index mismatch. The first 3 mismatches have the largest contribution to the overall waveguide loss. For example, as reported in [29], insertion loss resulting from the butt coupling of SU-8 waveguides with an index difference of 0.25 delta % to a normal SMF-28 fibre is ~10 dB, ~6 dB, and 2 dB for a 3 μm, 5 μm and 10 μm wide waveguide. Hence minimizing the insertion loss to the ordinary fibre system - SMF -28 is important in waveguide fabrication.

Mode Field Diameter (MFD) Mismatch – usually applicable when both waveguides to be aligned are in single mode operation. In a single mode waveguide, the intensity of the guided light will reduce radially in a Gaussian profile and the MFD is defined as the diameter in which the light intensity of the guided light reduced to $1/e^2$ of its peak intensity. MFD is a function of core size, the index difference between the waveguide

core and cladding and the fibre profile (step index or grad index). If the MFD between two waveguides to be aligned are different, there will be a MFD mismatch loss [30]. Note that MFD miss match is bi-directional. MFD mismatch loss between 2 waveguides denoted with subscript 1, and 2 can be estimated by

$$Loss_{MFD} = 10\,log(\frac{4}{(\frac{w_1}{w_2}+\frac{w_2}{w_1})^2}) \qquad \text{Eqn 3.3}$$

Core Diameter Mismatch – if either one or both sides of the waveguides to be aligned is/are multimodal, core size mismatch is a more appropriate description than MFD mismatch. Note that, core size mismatch is only significant when a larger core waveguide was coupled into a smaller core waveguide. Core diameter mismatch loss can be estimated by

$$Loss_{Core} = 10\,log\frac{d_r}{d_t} \quad , d_r < d_t \qquad \text{Eqn 3.4}$$

where "r" refers to receiving and "t" refers to transmitting waveguide [31].

Numerical Aperture (NA) Mismatch – NA of a waveguide determines its solid angle. A waveguide with smaller NA will have a smaller solid angle compared to a waveguide with larger NA. Similar to core size mismatch, NA mismatch is directional and is only significant when the receiving waveguide having smaller NA [31]. NA mismatch loss can be estimated by

$$Loss_{NA} = 10\,log\frac{NA_r}{NA_t} \quad , NA_r < NA_t \qquad \text{Eqn 3.5}$$

Core size mismatch (or MFD mismatch) and NA mismatch are additive, which means that the total loss is the sum of both core size mismatch and NA mismatch for ideal conditions. However, additional loss factors exist in butt-coupling joints, including fibre-end separation, fibre-end angle and Fresnel reflection.

In order to minimise the coupling loss between optical fibres and SU-8 waveguide, both MFD and NA of the coupling fibre need to be as closely matched to the SU-8 waveguide as possible. Among some of the commercially available fibres are SMF-28, HI-980 and UHNA4. The MFD of SMF-28, HI- 980, UHNA4 and SU-8 are 10.67 μm, 6.41 μm, 3.87 μm, and 3.84 μm respectively at 1550 nm. Meanwhile, their NAs are 0.14, 0.21, 0.35, and 0.39 respectively. Therefore, UHNA4 were found to have the closest MFD and NA with the current SU-8 waveguide design. Table 3.1 compares the theoretical and the experimental value of insertion loss between SMF-28 and UHNA4 fibres with 3x3 μm and 5x5 μm core dimension SU-8 waveguide.

Table 3.1: Insertion of SU-8 waveguide to SMF and UHNA4 fibre at 1550 nm.

Fibre type	**Waveguide core dimension (μm^2)**	**Theoretical (dB)**	**Measured over 1 cm long waveguide (dB)**
SMF 28	5x5	~8.9	~10
	3x3	~14	~20
UHNA4	5x5	~9.5	~10
	3x3	~0.7	~3

Note that the measured value are greater than the theoretical value due to surface scattering (more prominent for smaller core size) and waveguide propagation loss. The waveguide propagation loss is estimated to be 1 dB/cm, obtained from cut back measurement. It is worth noting that the splice loss between SMF-28, which is used in all telecommunication devices, and UHNA4 fibre can be as low as 0.3 to 0.6 dB with optimized splicing parameters. Therefore, the loss SU-8 waveguide interconnections can be made by using UNHA4 fibres, which are themselves spliced to standard SMF-28 fibres using optimized splicing parameters.

3.10 Optical Characterization

The fibre butt-coupling setup is shown in Figure 3.11. The procedure of light coupling is simple. First, the input fibre was aligned parallel to the waveguide channel with the help of a microscope. The fibre was placed on top of the waveguide and the pitch and tilt angles were adjusted to be parallel. Secondly, a 650 nm red light source was launched into the input fibre and the fibre was aligned to the waveguide channel. A red light source was initially used instead of 1550 nm (or other wavelength of interest) for the convenience of alignment as 650 nm light is observable by human eyes. Care was taken so that the input fibre tip is not in contact with the waveguide channel to avoid physical damage. An objective lens was placed at the output end of the waveguide channel to project the image of the waveguide output onto a screen. The experimental setup is shown in Figure 3.12a. When the input fibre was aligned to the waveguide channel, a small red dot (or multiple dots, depending on the number of output channels), with a long slab was observed as shown in Figure 3.12b. The red dots are the images of the waveguide channel outputs. Figure 3.12d shows the output from a commercial 1x8 splitter with 1550 nm light coupling. The image was captured using an infrared (IR) camera. When the input fibre was aligned to the waveguide channel, 8 bright dots were observed with minimum slab intensity. The small slab intensity is an indication of a good quality waveguide. The aligned sample is now ready for mode characterization and insertion loss measurement.

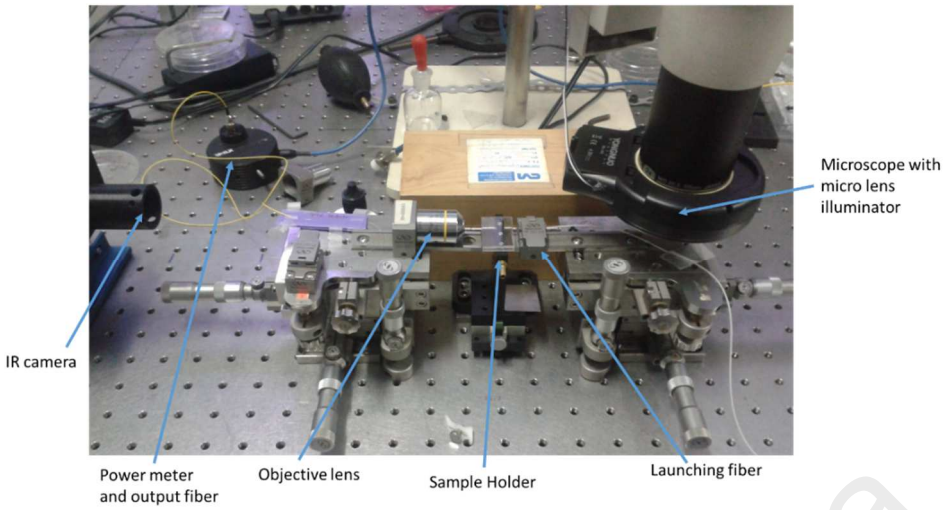

Figure 3.11: Waveguide optical alignment system.

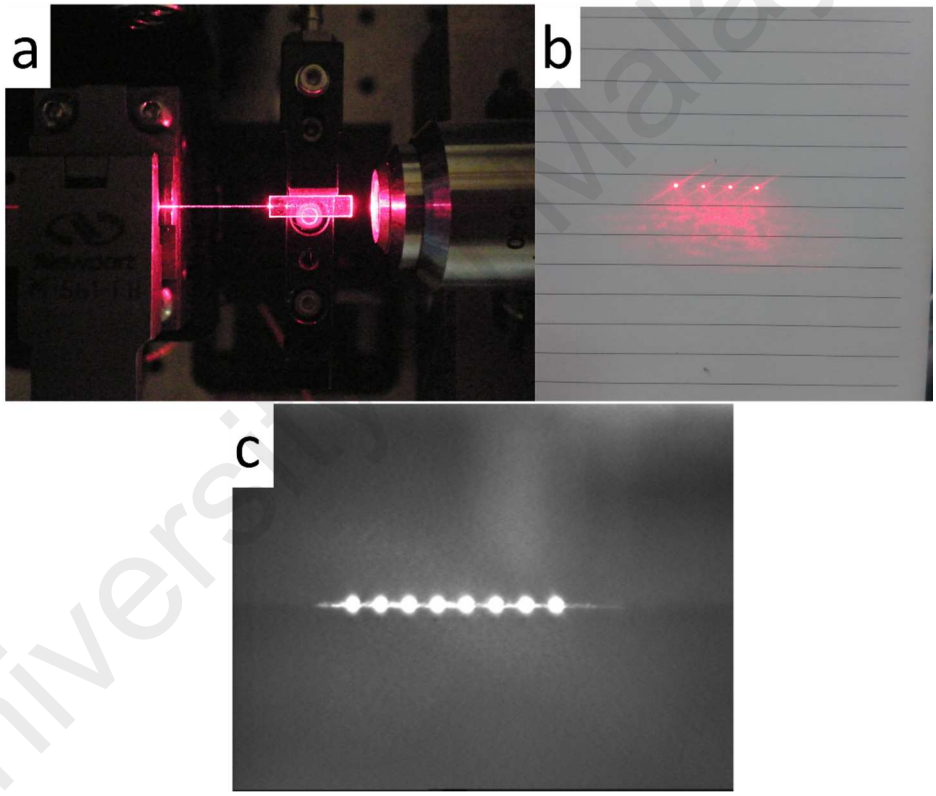

Figure 3.12: a) The top view of fibre to waveguide alignment setup using a red light source. The output of waveguide with b) red light source projected on to a white screen (for 1x4 splitter) and c) 1550 nm light source recorded with IR camera (for 1x8 splitter).

Mode Characterization

Mode characterization is important to study the guided light profile and whether it is in single mode operation or supports higher order spatial modes. To perform this

measurement, the red dot was first aligned into the IR camera until it can observe on the screen. The light source was then changed to 1550 nm (or other wavelength of interest) and the input fibre was aligned until maximum intensity was obtained at the waveguide channel output. Subsequently, the input power was reduced until no saturation observed in the IR camera image and the image was saved in grey scale and its intensity profile analysed using image analysis software. The input fibre was then slightly misaligned to see if higher order modes can be excited and guided by the waveguide channel. If only a Gaussian beam profile with varying intensity was observed during misalignment, the waveguide channel can be considered as a single mode waveguide at and above the wavelength used in the measurement.

Insertion Loss Measurement

To measure the insertion loss of the waveguide channel, the output objective lens was replaced with an output fibre after the input fibre was aligned to the waveguide channel using a red light source. This was followed by the alignment of the output fibre until the red light was observable at the output fibre pigtail. Next, the optical source was changed to 1550 nm (or other wavelengths of interest) and the output fibre pigtail connected to an optical power meter. Index matching fluid was applied onto both input and output fibre ends to reduce index mismatch between fibre and waveguide channel. Both input and output fibres were aligned until maximum power was measured by the power meter. Insertion loss can be determined by subtracting the measured output power from the launch power of the input fibre. At this stage, other characterization such as optical return loss, and polarization dependent loss can be conducted with slight modification to the launching and output fibre configurations.

Fibre to Waveguides Permanent Bonding

To bond the fibre permanently onto the waveguide, both the fibre ends and waveguide must be cleaned using IPA to make sure that they are grease free. Any surface contamination will cause adhesion problems. The step taken is similar to the insertion loss measurement with the index matching fluid replaced by NOA UV resin. After maximum power was obtained by alignment of both input and output fibres, UV light source from a portable UV source was irradiated on to both fibre ends for about 5 minutes. During the UV irradiation, the UV resin may be harden non-uniformly and may cause misalignment, which required minor alignment of both input and output fibres to re-obtain the maximum transmitted power.

3.11 Summary

Fabrication process of planar waveguide using photolithography techniques and waveguide characterization methods have been discussed in detail. The waveguide width of the fabricated SU-8 waveguides range from 3-5 μm. Using high NA optical fibres, low loss interconnection of the SU-8 waveguide was achieved. The minimum insertion loss was 3 dB measured at 1550 nm.

References

1. *SU-8 2002 Processing Guides*. MicroChem: MicroChem, http://www.microchem.com/pdf/SU-82000DataSheet2000_5thru2015Ver4.pdf.

2. Chien, S., *Investigation of SU-8 Waveguides*. 2005.

3. Yang, B., et al., *Fabrication and Characterization of Small Optical Ridge Waveguides Based on SU-8 Polymer.* Journal of Lightwave Technology, 2009. **27**(18): p. 4091-4096.

4. Bêche, B., et al., *Single-mode TE00–TM00 optical waveguides on SU-8 polymer*. Optics Communications, 2004. **230**(1–3): p. 91-94.

5. Borreman, A., et al., *Fabrication of Polymeric Multimode Waveguides and Devices in SU-8 Photoresist Using Selective Polymerization.* IEEE/LEOS Benelux Chapter 2002 Annual Symposium, 2002: p. 83-86.

6. Stephan, K., et al., *Processing of thin SU-8 films.* Journal of Micromechanics and Microengineering, 2008. **18**(12): p. 125020.

7. *Datasheet*. PPG Optical Product, www.ppg.com.

8. Yahya, N.A.M., et al., *Fabrication and characterization of a dual layer multiple refractive index benzocyclobutene polymer platform for integrated optical devices.* Optical Materials, 2012. **34**(11): p. 1735-1741.

9. Ibrahim, M.H., et al., *Single mode optical waveguides based on photodefinable benzocyclobutene (BCB 4024–40) polymer.* Microwave and Optical Technology Letters, 2007. **49**(2): p. 479-481.

10. Wan-Shao, T., et al., *Study of the Fabrication of BCB Waveguide Devices by Ultraviolet Pulsed-Laser Illumination.* Photonics Technology Letters, IEEE, 2008. **20**(2): p. 84-86.

11. Liang-Yin, C., et al., *Fabrication and Characterization of Benzocyclobutene Optical Waveguides by UV Pulsed-Laser Illumination.* Quantum Electronics, IEEE Journal of, 2007. **43**(4): p. 303-310.

12. Kane, C.F. and R.R. Krchnavek, *Benzocyclobutene optical waveguides.* IEEE Photonics Technology Letters 1995. **7**(5): p. 535-537.

13. Kane, C.F. and R.R. Krchnavek, *Processing and characterization of benzocyclobutene optical waveguides.* Components, Packaging, and Manufacturing Technology, Part B: Advanced Packaging, IEEE Transactions on, 1995. **18**(3): p. 565-571.

14. Norland, *Product Data Sheet*, www.norlandprod.com.

15. Singhal, R., M.N. Satyanarayan, and S. Pal, *Fabrication of monomode channel waveguides in photosensitive polymer on optical adhesive.* Optical Engineering, 2011. **50**(9): p. 094601-094601-3.

16. Jou Xie, A., F. Song, and S.-W. Seo, *An acousto-optic sensor based on resonance grating waveguide structure.* Sensors and Actuators A: Physical, 2014. **216**(0): p. 364-369.

17. Nam, S.-H., J.-W. Kang, and J.-J. Kim, *Direct pattering of polymer optical waveguide using liquid state UV-curable polymer.* Macromolecular Research, 2006. **14**(1): p. 114-116.

18. Prajzler, V., N. Neruda, and J. Spirkova, *Planar Large Core Polymer Optical 1x2 and 1x4 splitters connectable to Plastic OPtical FIber* Radioengineeing, 2013. **22**(3): p. 751-757.

19. Lee, K.S., H.L.T. Lee, and R.J. Ram, *Polymer waveguide backplanes for optical sensor interfaces in microfluidics.* Lab on a Chip, 2007. **7**(11): p. 1539-1545.

20. Gary, S.M. and C.J. Spanos, *Fundamentals of Semiconductor Manufacturing and Process Control*. 2006: Wiley

21. Sangjun, H., J. Derksen, and C. Jung-Hoon, *Extrusion spin coating: an efficient and deterministic photoresist coating method in microlithography.* Semiconductor Manufacturing, IEEE Transactions on, 2004. **17**(1): p. 12-21.

22. *Spin Coat Theory*. Columbia University, http://www.clean.cise.columbia.edu/process/spintheory.pdf.

23. Tortai, J.H., *Modeling of ultra thin resist film structure after spin-coating and post-application bake.* Microelectronic Engineering, 2004. **73–74**(0): p. 223-227.

24. Bogdanov, A.L. *SU-8 negative photoresist for optical mask manufacturing*. 2000.

25. Vempati Srinivasa, R., et al., *A thick photoresist process for advanced wafer level packaging applications using JSR THB-151N negative tone UV photoresist.* Journal of Micromechanics and Microengineering, 2006. **16**(9): p. 1841.

26. Tien, P.K. and R. Ulrich, *Theory of Prism-Film Coupler and Thin-Film Light Guides.* Journal of the Optical Society of America, 1970. **60**(10): p. 1325-1337.

27. Ulrich, R., *Theory of the Prism-Film Coupler by Plane-Wave Analysis.* Journal of the Optical Society of America, 1970. **60**(10): p. 1337-1350.

28. *SPA 4000 Prism Coupler User Manual*. Sairon Technology Inc, www.sairontech.com.

29. Nordstrom, M., et al., *Single-Mode Waveguides With SU-8 Polymer Core and Cladding for MOEMS Applications.* Lightwave Technology, Journal of, 2007. **25**(5): p. 1284-1289.

30. Marcuse, D., *Loss Analysis of Single-MOde Fiber Splices.* THe Bell System Technical Journal, 1977. **56**(5).

31. *Single Fiber Fusion Splicing - Application Note by Corning*, http://www.corning.com/media/worldwide/coc/documents/Fiber/RC-Application%20Notes/AN103_06-09.pdf.

CHAPTER 4: GRAPHENE, GRAPHENE OXIDE AND GRAPHENE OXIDE FILM

In this chapter, the physical and chemical properties of Graphene and Graphene Oxide (GO) are first discussed. This is followed by the discussion of synthesis process of GO solution and fabrication of GO Film (GOF) using drop-casting technique. A series of characterization tests on the GO solution and GOF conducted to verify the successful production of both "materials" during this study are discussed in detail. The test results also provided valuable information on the synthesized GO which is useful in subsequent studies. Finally, the effects of a number of experimental variables on the fabricated GOF are then discussed. These variables include GO solution concentration, volume droplet size, multiple drop casting and their corresponding film formation thickness and surface morphology.

4.1 Introduction to Graphene

Graphene is a single layer graphite consists of 2-dimensional monoatomic thick carbon atoms arranged in a honeycomb (hexagonal lattice) crystal structure. This structure is the unit block to construct other carbon-based materials. It can be folded into fullerenes, rolled up into nanotubes or stacked into graphite. The six-corner of the Graphene hexagonal Brillouin zone where the carbon atoms are allocated are called Dirac points and the electrons and holes are known as Dirac fermions. The symmetric conduction and valence band with respect to the Fermi level at the Dirac point causes a very unique electronic structure where it has zero bandgap properties and behaves as a semi-metal. Graphene has a universal minimum conductivity, σ in the order of $\frac{\pi e^2}{2h}$ where *e* is electron charge and *h* is Plank constant [1, 2].

The zero bandgap property and charge neutrality in Graphene enables optical transition transmission over a broad wavelength range from visible to infrared. In pristine Graphene, only interband transitions, which refer to electron excitation from the covalence band to the conduction band, are allowed. This is because in Graphene the valence band is fully filled while the conduction band is empty. This band structure can be easily modified – temporarily by applying a voltage potential; or permanently via chemical doping [3-5]. An n-doped Graphene (Fermi level is shifted into the conduction band), optical phonon with energy of less than $2E_f$ cannot be absorbed because the electron state in resonance in the conduction band is occupied, hence interband transition is not allowed. The same goes to p-doped Graphene, where optical phonon with energy of less than $2E_f$ cannot be absorbed because there are no electrons available for interband transitions. However, this optical phonon energy allows another type of transition– intraband transition. Intraband transition refers to electron transition within either valance or conduction bands. This type of transition is mainly observed in metals because metals have unfilled electron bands. Intraband transitions are not quantized and all photons with energy smaller than E_f can be absorbed continuously. These two types of transitions enable Graphene to support different plasmonic polarization modes. For interband (intraband) transition, TE- (TM-) mode where the electric field is parallel (perpendicular) to the Graphene plane can be supported. The polarisation effect of Graphene has been demonstrated by Bao [6], Kim [7, 8] and Liu [5]. The Graphene layer used in these works were produced using Chemical Vapour Deposition (CVD) technique, which exhibits very high quality with minimum defects. However, it is to date not possible to deposit Graphene directly onto optical waveguide materials such as silica glass, silicon and polymers. Coating of Graphene onto an optical waveguide requires physical transfer of the Graphene layer from its nickel or copper substrate onto the optical waveguide, which will introduce discontinuities and defects during the transfer process. Discontinuities due

to defects in the Graphene coating will in turn increase the propagation loss of the optical waveguide. Therefore, a method large area Graphene coating with minimum defects is still being pursued. Practically, few-layer (< 5 layers) Graphene was used instead of monolayer Graphene as reported by Bao et al. and Kim et al. However, adding extra layers of Graphene will cause the overall Graphene film conductivity will drop dramatically and eventually change its optical properties. The extinction ratio of a waveguide polariser dropped tremendously from 25 dB (2 – 3 layers Graphene) to less than 10 dB for Graphene coating of more than 20 layers. Moreover, the highest extinction ratio reported were just 27 dB, which is limited by the imperfections of the Graphene layer/s deposition.

Recently, uniform coating of Graphene Oxide (GO) layers using drop-casting technique has been reported. This method provides a simple alternative for uniform coating of thin Graphene-based films over a finite area [9]. By increasing the concentration of the GO solution used, it becomes possible to produce GOF with micrometer-scale thicknesses and a coating area in the square millimeter range [10].

4.1.1 From Graphene Oxide to Graphene Oxide Paper

Dikin et al defined GO Paper (GOP) as “a free-standing carbon-based membrane material made by flow-directed assembly of individual GO sheet” [10]. The formation of GOP requires the following criteria. First, at least a few hundred layers of GO are needed to form a free-standing membrane when stacked together. Second, a certain directional flow is required to assemble the GO sheets which are interlocked together in a near-parallel fashion to form GOP. Without either one of the above mentioned criteria, GOP could not be formed. The raw material used to produce GOP is GO solution produced

using improved Hummer's method (discussed in section 4.1.2). The synthesis of GO solution is discussed in section 4.1. A controlled volume of the GO solution is then to drop-casted onto a flat surface (or directly onto the waveguide channel) using a micropipette. With the natural directional flow in the solution drop during the drying process, the GO flakes will then be stacked into the GOP. This directional flow mechanics and the drying process are discussed in section 4.3. The appearance of GOP is dark brown under transmitted light and almost black in reflection when its thickness is more than 5 μm. The appearance of the GOP can refer to Figure 4.1. Wrinkles are observed over the GO coating and is believed to be due to edge-to-edge overlapping of GO sheets [11]. The amplitude of the wrinkles is found to be dependent on the concentration of GO solution used. A detailed discussion on the occurrence of wrinkles is presented in section 4.3.

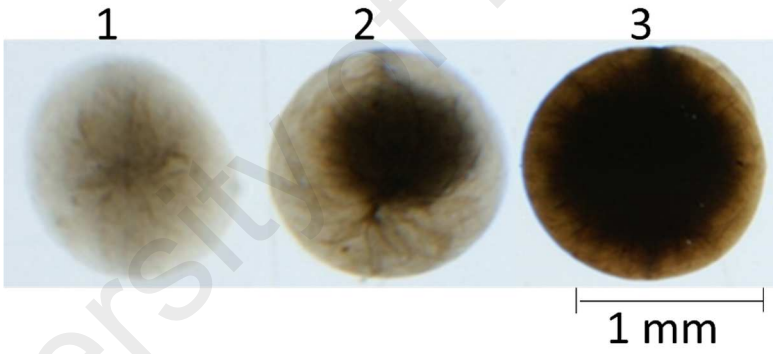

Figure 4.1: Microscope image of different number (ranging from 1 drop on the left to 3 drop) of drop-casted GO.

Figure 4.2 shows the FESEM image of the cut edge of a drop-casted GOP. It can be seen that the GO layers are stacked in an orderly fashion, forming a thick-layered GOP. Physically, the GOP is very strong, with good homogeneity and strong interlayer binding compared to ordinary paper. When the GOP is being stressed beyond its elastic limit, straight and flat fracture cuts were observed and there are no pull-out of its lamellae layers as shown in Figure 4.2. The mechanical strength of the GOP also depends strongly on its

water content. The modulus value of the GOP can increase two-fold for dried sample (at 120 ^{o}C) compared to the hydrated sample (at 40 ^{o}C). This phenomenon is similar to cellulose-based paper where wet sheet has lower strength. The electrical characteristics of the GOP are highly temperature dependent, which determines the amount of reduction of the GOP. In general, GOP show insulator characteristic and its conductivity increases with increasing temperature (degree of reduction) [10, 11].

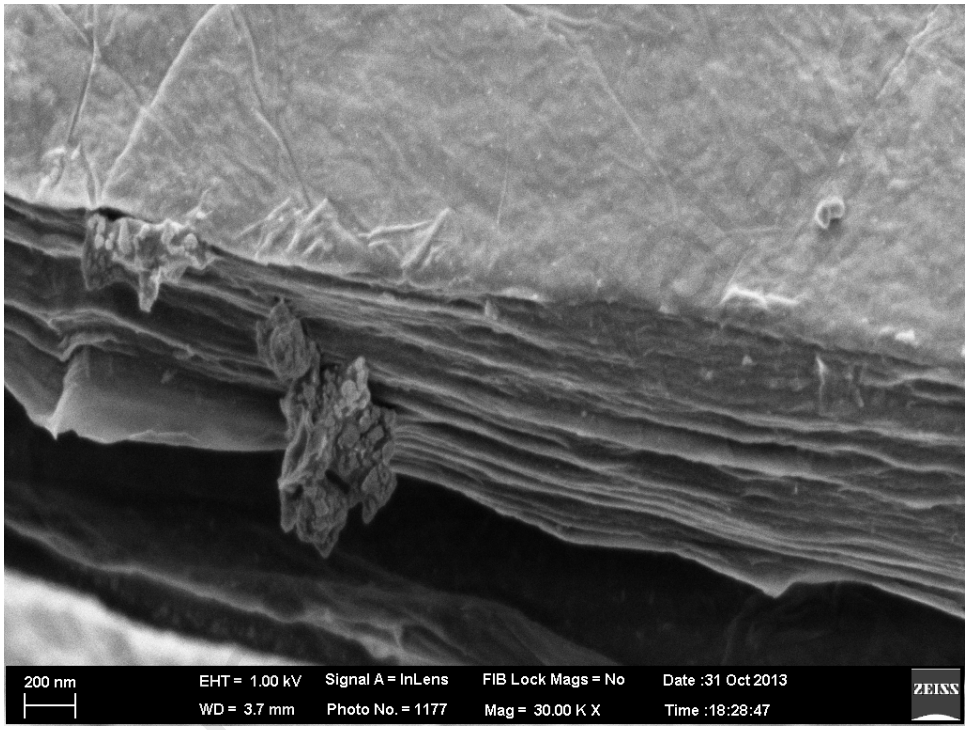

Figure 4.2: FESEM image of cut edge of GOP.

It should be noted that in this thesis, the GOP formed on flat a substrate or directly onto a waveguide channel was not purposely peeled off to form free-standing sheet. This contradicts with the definition of GOP (a free-standing GO sheet), and to avoid confusion, the term GO Film (GOF) instead of the GOP was used in the following discussions. Distinction should also be drawn upon the term single layer GO or few layers GO (less than 10 layers, for example) which was used to describe very thin GO layers, and the term GOF to describe GO with more than 10 layers.

4.1.2 Graphene Oxide Preparation

To date, there are many chemical oxidation methods to produce GO solution such as Hummer's method [12], Staudeumaier's method [13], and Brodie's method [14]. The method used in this work was modified Hummer's method [15] in which the process temperature as well as oxidation duration was lower and shorter, respectively. The synthesis process is as follow. In the beginning, graphite was oxidised to a high degree of oxidation by adding Potassium Permanganate ($KMnO_4$) into concentrated acid such as sulphuric acid under room temperature with constant stirring for 3 days. During this period, the colour of the mixture changed from dark purplish green to dark brown. To end the oxidation process, Hydrogen Peroxide (H_2O_2) solution was added, and the colour of the mixture changed to bright yellow, indicating high oxidation level of graphite. The graphite oxide was then washed several times with Hydrochloric Acid (HCl) and deionized (DI) water until a pH of 4-5 was achieved. The washing process was carried out using simple decantation of supernatant via a centrifugation technique with a centrifugation force of 10,000 g (g-force). During this process, the graphite oxide was exfoliated to formed GO gel. Finally, this gel was diluted using DI water into a suitable concentration for drop-casting. The overall process was summarized in Figure 4.3.

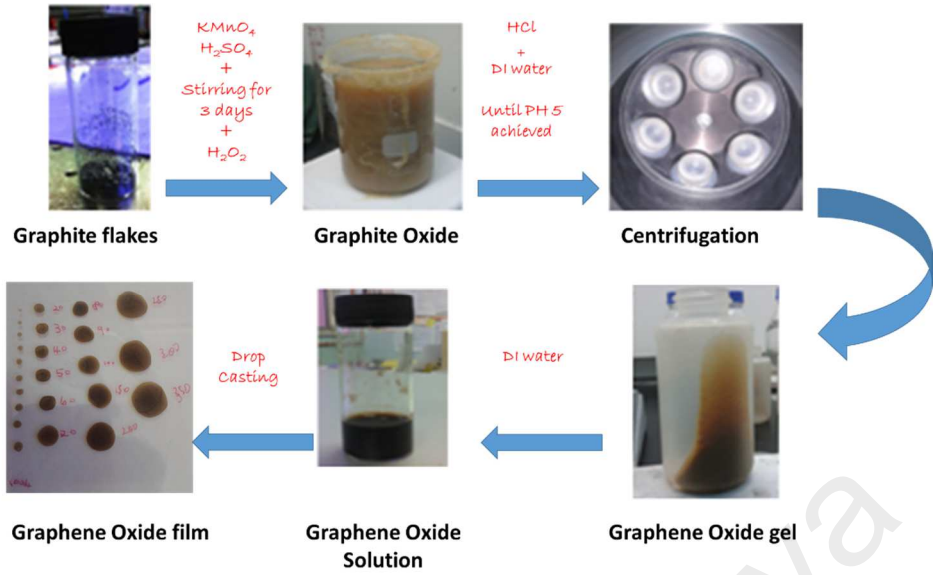

Figure 4.3: Summary of GOF fabrication from Graphite flakes.

4.1.3 Characterization of Graphene Oxide and Graphene Oxide Film

Fourier Transform Infrared Spectroscopy (FTIR), UV-Visible-Near Infrared Spectroscopy (UV-VIS-NIR), Raman Spectroscopy, Atomic Force Microscopy (AFM) and X-ray Diffraction measurement (XRD) were carried out to characterize the GO solution and GOF. GOF was formed using either spin-coating or drop-casting method. These series of characterisation tests showed that single or few layers GO was successfully fabricated. Details of each measurement are discussed in the following sections.

4.1.3.1 Atomic Force Microscopy

Figure 4.4 shows the AFM images (Agilent 5500) of spin-coated GO solution on a silicon substrate. The thickness of the GO flakes produced is about 1.2 nm. This is the value reported by other research groups as the single layer thickness for GO [16, 17]. On the other hand, the lateral size of GO flakes has a large variation, ranging from 0.1 μm to

1 μm. The GO flakes showed little or no symmetrical shape, which is critical in its ability to produce a uniform GOF using drop-casting method.

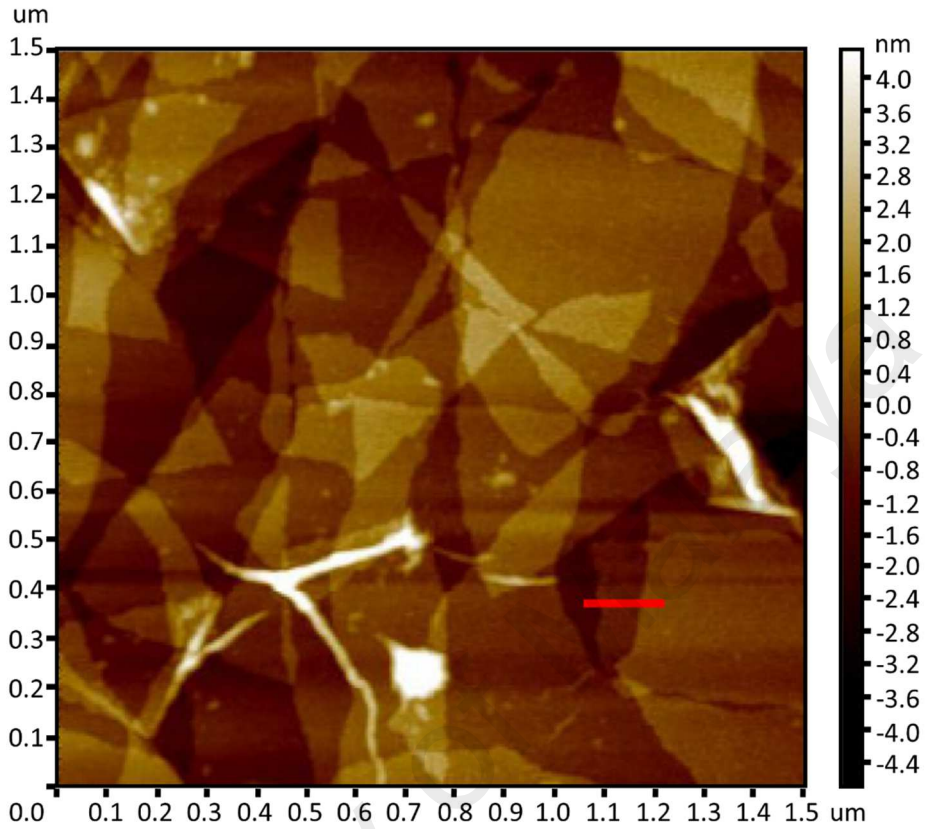

Figure 4.4: AFM image of spin-coated GO solution.

4.1.3.2 UV-Visible-Near Infrared Spectroscopy

Figure 4.5 shows the UV-VIS absorption spectrum (Thermo Scientific Evolution 300 Spectrometer) of the GO solution. GO solution was placed in a standard fused quartz cuvette. An absorption peak was observed around 230 nm, which is due to the strong $\pi \rightarrow \pi^*$ transitions of aromatic $C = C$ bonds. Slightly shift lower (larger) of ~2 nm can be obtained for higher (lower) degree of oxidation with more (less) functional groups on the GO basal plane. A small 'shoulder' observed at ~300 nm can be attribute to the $n \rightarrow \pi^*$ transitions of $C = O$ bonds. Other than these transitions, no obvious band edge absorption up to 1800 nm was observed. This result is in close proximity to the absorption characteristic of graphite oxide as reported in [18, 19]. The plot below 200 nm can be

ignored, due to fluctuations in baseline measurement, which was caused by the absorption of deionized water and air.

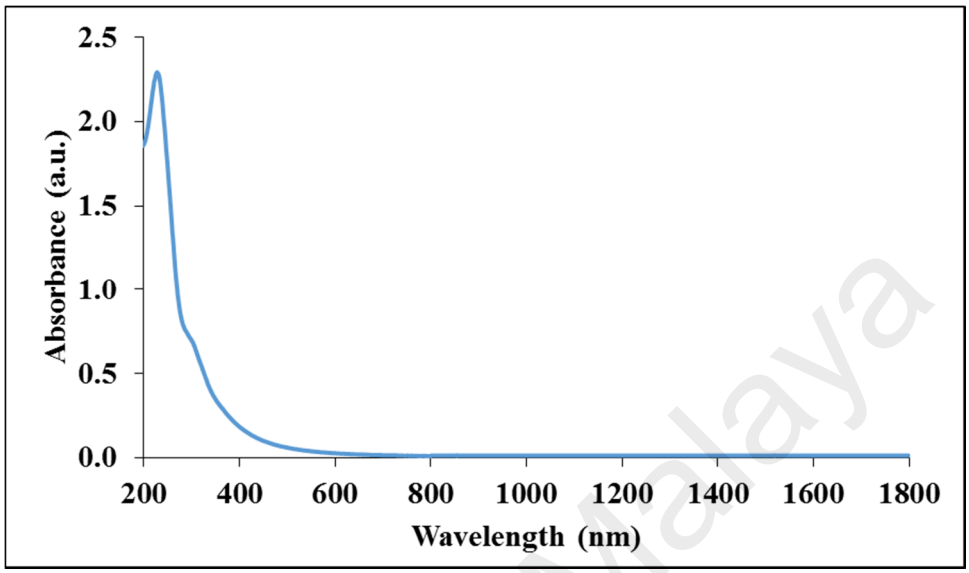

Figure 4.5: UVVIS absorbance spectrum of GO Solution.

4.1.3.3 Raman Spectroscopy

Figure 4.6 shows the Raman spectrum (Renishaw inVia Raman Microscope) of spin-coated GOF. Three main GO characteristic peaks were observed. They are the D peak (at ~1360 cm^{-1}) corresponding to the stretching of C-C single bond, the G peak (at ~1604 cm^{-1}) corresponding to first-order scattering of the E_{2g} phonon of sp^2 C atoms and the 2D overtone peak (at ~2700 cm^{-1}). The prominent D peak indicates significant structural disorder that can be attributed to the incorporation of oxygen [20-22]. The intensity ratio of D to G peak is about 0.85 which is about the reduction level of near to 5 with reference to Figure 4.7, which corresponds to a bandgap of about 2 eV. Note that this figure are obtained from [3] where the bandgap was measured by spectroscopic ellipsometry and parameter fitting to a Lorentz oscillator model. The reduction was made by exposing the GO to hydrazine and ammonia solution with different reduction time. The x-axis in Figure 4.7 refers to the amount of reduction time where larger value

indicates longer exposure time to a chemical mentioned above. These characterizations proved that the solution is GO solution with a high degree of oxidation.

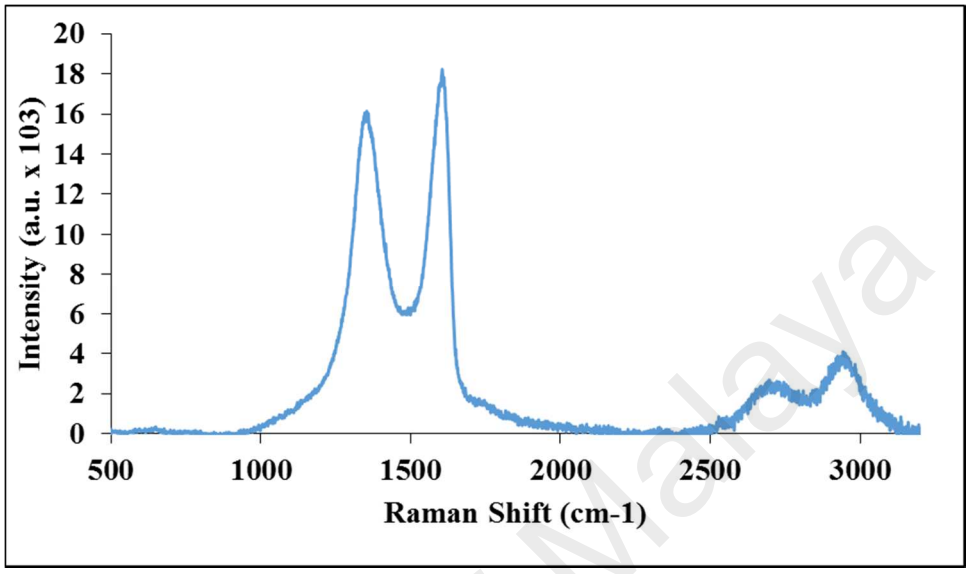

Figure 4.6: Raman spectrum of GOF.

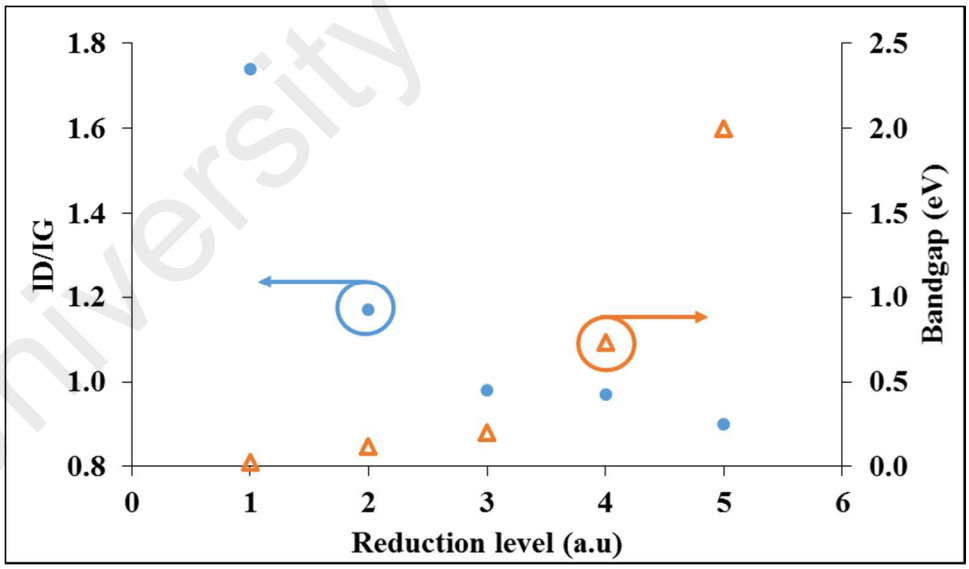

Figure 4.7: Relation of ID/IG and bandgap, where reduction level in x-axis is just an arbitrary unit of time. [3]

4.1.3.4 Fourier Transform Infrared Spectroscopy - Attenuated Total Reflection

The FTIR-ATR of GOF is shown in Figure 4.8. Several major peaks that correspond to Epoxides, Carbonyls, and Hydroxyl group were observed. For easy viewing, each peak that corresponded to each vibrational bonds were summarised in Table 4.1. The table is validated applied for single or multi-layers GOF. With the presence of physisorbed water, it was observed that both OH stretching (3000-3500 cm^{-1}) and scissors (1600-1650 cm^{-1}) modes of H_2O are broadened through hydrogen interactions with C-OH (O-H stretch at 3000-3700 cm^{-1}) and COOH (OH stretch at 3549cm^{-1}). The FTIR spectroscopy results obtained are similar to reports by other research groups [23-26].

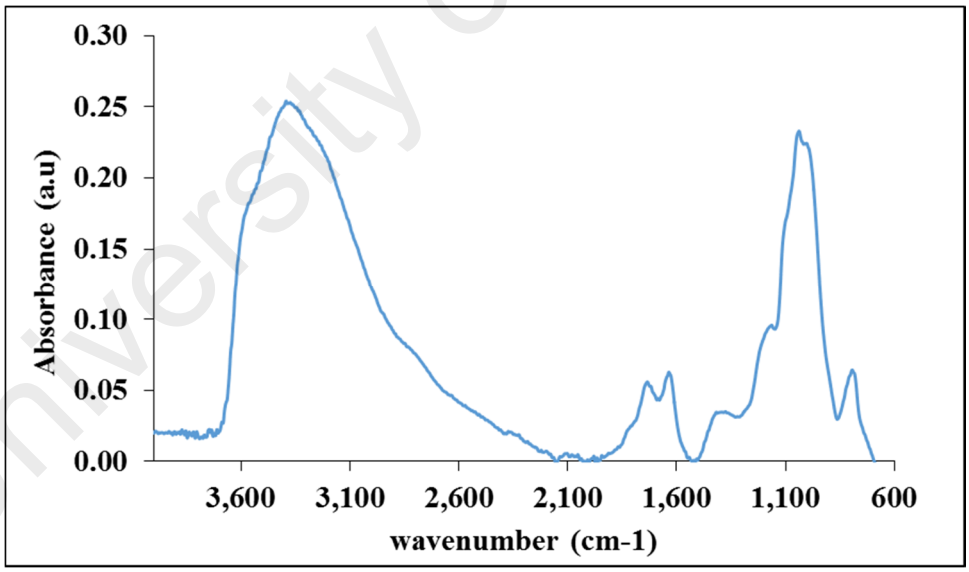

Figure 4.8: FTIR-ATR absorption spectrum of GOF.

Table 4.1: Summary of vibrational modes of GO in FTIR absorption.

Name	**Chemical composition**	**Wavenumber (cm^{-1})**
Epoxides	C-O-C	1280-1320, 800-900
Edge Carboxyl or H_2O	COOH	1650-1750
Carbonyls	C=O	1750-1850
Carbonyls	O-C=O	1500-1750
Asymmetric vibrational stretching of sp2-hybridized	C=C	1500-1600
Edge Carboxyl	C-OH	3000-3700
Stretching of hydroxyl in water include Basel Plane hydroxyls, and Phenol (Edge hydroxyl)	C-OH	3000-3700 With peak at 3400
	Isolated hydroxyl group	Peak at 3610
	C-OH in GO	Peak at 3100

4.1.3.5 X-Ray Diffraction Measurement

Figure 4.9 shows the XRD spectrum of GOF. The interlayer spacing of the GOF, estimated from the diffraction angle (at 8.7^o with wavelength 15.406 nm), was about 1.02 nm which is slightly higher than reported by Dikin [10]. However, it is within the separation range between 0.6 – 1.2 nm, which is dependent on humidity due to water intercalation between the GO layers. A model describing this phenomenon is shown in

Figure 4.10 [27]. Interlayer spacing of about 0.6 nm can be considered as “dry” while for a spacing of 1.2 nm, the GOF is considered to be fully hydrated [28]. The measured thickness indicates that large amount of water molecule is present in between the GO layers, corresponding to a relative humidity of >75%. As GO exhibits hydrophilic characteristic, it is very difficult to completely remove water out of the GOF. On the other hand, there are also areas in the GOF where oxidation cannot occur in the “inner” layers due to low level of oxidation. This is shown as the second peak in the XRD spectrum with a diffraction angle of 16.5^{o} corresponding to 0.54 nm.

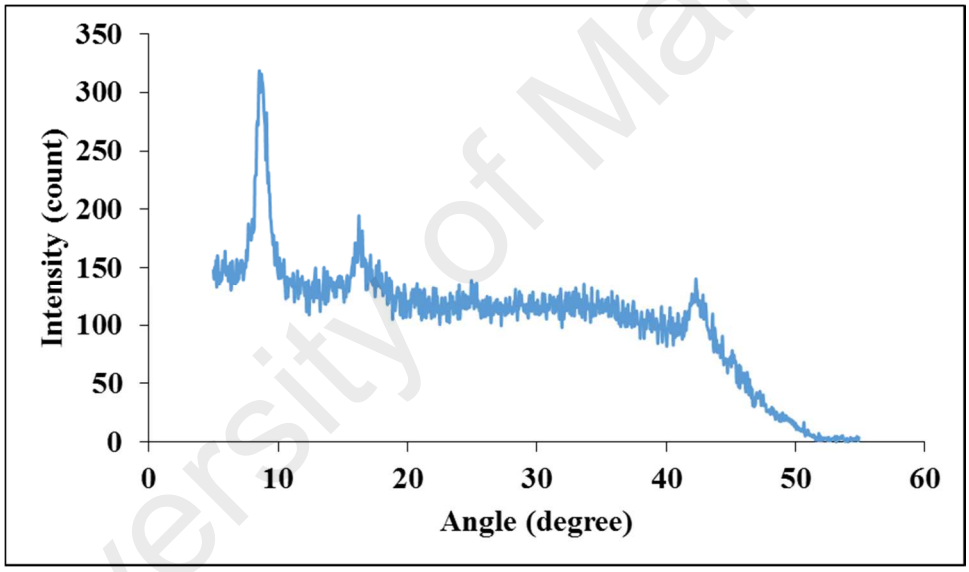

Figure 4.9: XRD spectrum of a thick GOF.

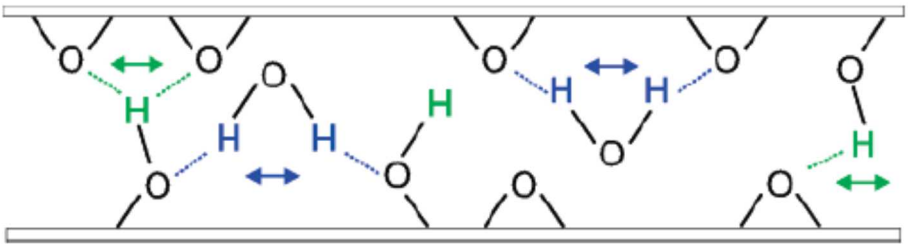

Figure 4.10: Model of the GOF cross section depicting water molecules intercalated between two Graphene Oxide layers. [27]

4.2 Other Unique Properties of Graphene Oxide Film

The structural, chemical and electrical properties of GOF have been discussed in the previous sections. These properties give rise to some interesting properties in GOF, which will be discussed below.

4.2.1 Anisotropic Dielectric Function

A material with anisotropic dielectric property mean either or both the real and imaginary part of a material refractive index depends on light incident direction. This phenomenon usually occur on thin metal film or material having crystalline structure. In general it is related to the material structure. The regular stacking order of GO produced using drop-casted GOF as measured using SEM, though not perfect as in Graphite (Graphite has hexagonal crystal structure), closely resembles its stacking structure. In details, the electron vibration within a GO sheet, parallel to GO plane, is relatively free and easy as compared to electron vibration within 2 or more GO sheet which is perpendicular to GO sheet. Which means that electron conductivity is higher for parallel to GO sheet. In optical point of view, conducting corresponding to damping or absorption of light. This mean that absorption of optical light parallel to GO sheet is expecting to be higher than in perpendicular direction. This unique characteristic of GOF together the ability of selectivity area coating via drop-casting driven it to be applied onto planar waveguide as waveguide polariser. The detailed study of GO based waveguides polariser is discussed in chapter 5.

4.2.2 Graphene Oxide BandGap and Conductivity

Unlike than Graphene where the conductivity is universal and frequency independent, refractive index of GO is depending on the bandgap opening either by chemical doping or electrically doping. Note that the term refractive index that mentioned is referring to the refractive index value parallel to the GO sheet. Through this thesis work, we are lacking of instrument to direct measure the refractive index as well as conductivity of GOF especially at the frequency of interest, 1550 nm. This is because the optical properties of GO can not be measured straightforwardly by the standard measurement system such as ellipsometry due to its small thickness (less than 1 nm) [29-31]. Moreover the real (imaginary) part of the refractive index of GO at visible wavelength can be varied from 1.8 to 2.3 (0.1 to 1.0), depending on its degree of reduction [29], further complicated the GO simulation work. However, bandgap estimation of 2eV from the Raman spectroscopy according to [3] which narrow down the conductivity into few thousand Sm^{-1} (corresponding to about 0.3 in imaginary part of refractive index) according to [32]. This value implied a significant light absorption. Conductivity higher than this value (few ten thousand Sm^{-1}) will induce plasmonic effect as in most of the metal, while the opposite will cause too litter light absorption. This conductivity range narrowing simplify the simulation work in chapter 5 and the conductivity of the GOF in 1550 nm is predicted about 2700 Sm^{-1} which is best fitted with our experimental results. This value is slightly larger than DC or low frequency value given by Stankovich (2420 $S.m^{-1}$) [33], Si (1250 $S.m^{-1}$) and Pantazopoulou (1670 $S.m^{-1}$) [34] (- in her simulation presentation slide in which derived from [35, 36]) but lesser than the value (9000 $S.m^{-1}$) given by Hong [37] at THZ frequency. On the other hand, the real part of the refractive index that best fitted with our experimental results in chapter 5 is about 2. This value also agreed by Vaupel, Stoble [38] and Jung [29] in optical frequency. More discussion on the optical property of GO is included in section 5.1.3.

4.2.3 Hydrophilic and Water Permeation in Graphene Oxide Film

Buchsteiner [27] and Lerf [28] demonstrated GO is hydrophilic and the interlayer spacing of GO is vary with amount of water molecule present. A spacing thickness of 0.6 nm can be considered as “dry” while 1.2 nm is considered to be fully hydrated. Our FTIR and XRD measurements in section 4.1.3 also showing similar water rich phenomenon in GOF. Acik [23] proven by FTIR studies that the Oxidized’ regions in Graphene sheet play an important role of absorbing water while strong H-bond. Later Nair [39] demonstrated that the peculiar characteristic of the GO membrane with strong filtration of even the smallest gas atoms/molecule such as helium and hydrogen but the exceptionally high permeation of water vapour. The interaction between the water molecule and the oxygen functional groups of the individual GO layers will further open up the GO layer bandgap which corresponding decrease in conductivity [40-42]. This is because in this interaction, water act as electro acceptor that redraw electron from the GO sheet. This unique characteristic of GOF driven it to be applied in optical water and humidity sensor by measuring the optical absorption of GOF. The details of this study are discussed in chapter 6.

4.2.4 Reversible Phonon Reduction of Graphene Oxide

Carbonaceous materials including GO have significant capability of self-heating through optical phonon excitation [43-46]. Guo [47] has shown that a 1 μm thick GOF can undergo a significant rise in temperature (> 40 ^{o}C difference compared to a bare substrate without GOF) when exposed to a low power broad band IR light source (with an emission spectrum covering the range from 1000 to 1700 nm). Thermally heated GOF will undergo a de-oxygenation reaction and the GOF will therefore be substantially reduced [23, 43, 47, 48]. A reduced-GOF has a remarkably higher conductivity - and

eventually larger optical absorption is observed [40-42]. However, thermally reduced-GOF is unstable and it can easily oxidise back to its initial state [47, 49]. This unique characteristic of GOF driven it to be applied as optical switch. The details of this study are discussed in chapter 7.

4.3 Drop-Casting of Graphene Oxide

Drop-casting is a simple technique used to coat materials onto a small area with no material waste. It involves applying a drop of solution onto a surface and is allowed to drying with or without controlling the drying environment such as humidity or temperature. The drying process of most solutions will create a coffee-ring effect [50], where the droplet edge will have a higher concentration of solute compare to its centre. This effect can be explained by the difference in evaporation rate of the droplet at different radial position. The effective area of the droplet edge is relatively larger than the centre and hence the solution evaporation rate at the edge is higher. This causes an effective capillary flow towards the droplet edge and brings together solutes than that is contained in the droplet. As a result, there is a gradual drop in the concentration of solute from the centre to the edge, followed by a sudden increase at the edge. Suppression of coffee ring effect has become a field of interest for researchers where the objective is to obtain a uniform coating with uniform concentration distribution within the coating, which is especially important in inject printing as well as spray coating. One of the effective technique to suppress the coffee-ring effect is to use solutes with asymmetry shapes such as ellipsoidal (or mixed ellipsoidal shape particle in ordinary spherical shape particle) [51]. As GO flakes are asymmetrically shaped, GOF produced using drop-casting technique will also have uniform thickness across the coating region with no observable coffee ring effect [9].

4.3.1 Drying Mechanism and Creation of Wrinkle

The suppression of coffee ring effect in GO drop-casting occurs during the drying phase of the drop-casting. Similar to spherical shape solutes, the ellipsoid (in this case, asymmetric GO flakes) suspended in its solution will be carried towards the air-solution interface by the same outward capillary flow. However, a strong, long range inter-particle capillary interaction occurred between ellipsoids and leads to the formation of loosely packed quasi-statics or arrested structures in the air-solution interface. It is worth noting that the magnitude of interaction between ellipsoids is two orders stronger than spherical particles at the interface. Relatively large energy is required to break up these clusters of ellipsoids particles. This interaction between ellipsoids significantly reduces their mobility within the solution droplet and prevents the ellipsoids from reaching the droplet edge and eventually stops the coffee ring effect. As a result, the drying edge or the area of solution droplet reduces progressively during the drying process as shown in Figure 4.11.

Figure 4.12 shows the drying of a drop-casted GO solution over time. It can be seen that once the solution drop was applied, the edge of the droplet was formed (as shown in Figure 4.12a). As water in the solution evaporates, it carries with the GO flakes towards the air-solution interface, causing accumulation of GO flakes and subsequent formation of GOF at the interface. As the droplet edge was pinned at the instants it was drop-casted, the droplet takes the form of a spherical cap. The area of this spherical cap is larger than the area covered by the droplet. When the drying process is completed, the formed GOF will collapse onto its base and form wrinkles as shown in Figure 4.12f.

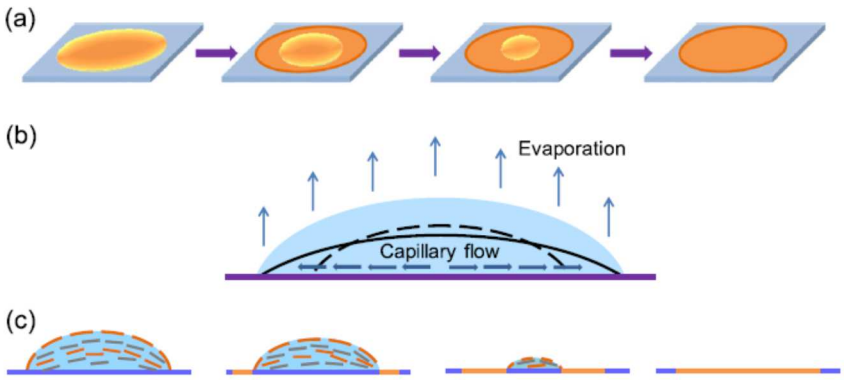

Figure 4.11: Schematic diagrams of a) ellipsoid particle solvent drying process, b) the solvent evaporating process, and c) the distribution of the ellipsoid lamellar cluster within the droplet during evaporation. [9]

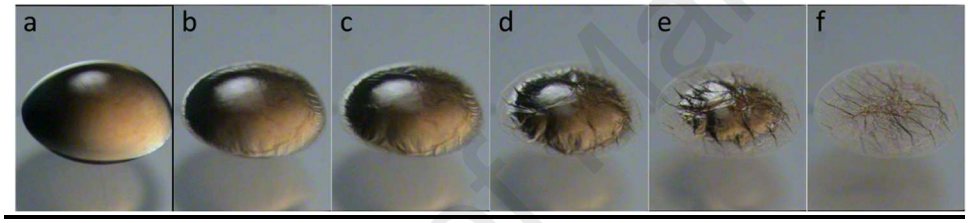

Figure 4.12: Image capture of GO solution drying.

4.3.2 Drop-Casting and Surface Morphology

To begin the drop-casting work, we simply fix the GO concentration to study the effect of volume on the GOF properties. It was found that the coating size increases with the volume of solution used, but the thickness remained about the same as shown in Figure 4.13 and Figure 4.14. The repeatability of coating diameter is not easy to control. For example, a 1 µl drop volume will produce a coating diameter of about 1.8 mm with a standard deviation of 0.15 mm, measured by taking the average of 50 drop-casted GOF. Note that in Figure 4.14, there is a difference in volumetric points interval at 100 µl. This change in volumetric intervals is due to the change of micropipette for different volume range. Hence, both pipette might not be calibrated accordingly. Besides, it was found that the substrate surface condition also effects the coating size. For example, if fuse silica

was used instead of plastic film, the coated diameter for 1 µl is about ~6 mm which is 3.3 times larger than on plastic film. The difference is related to surface tension between the GO solution and the substrate. This difference causes differences in contact angle. Larger contact angle will produce smaller droplet size and vice versa.

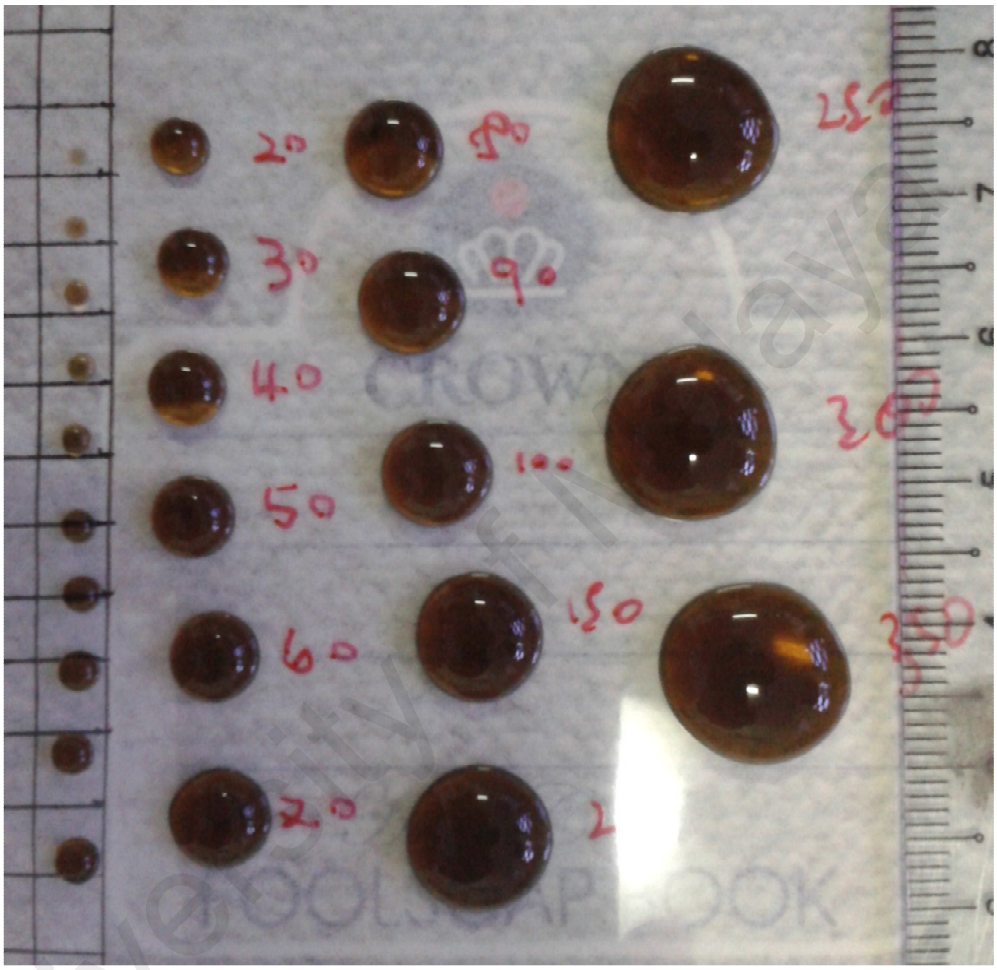

Figure 4.13: Image capture of drop-casted GO with various drop-casted volume.

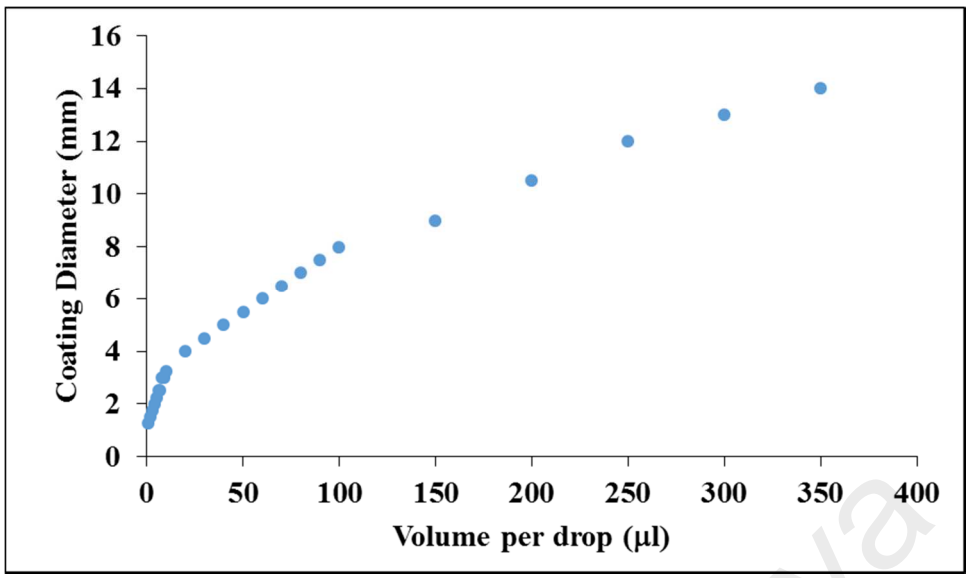

Figure 4.14: Coating diameter against drop-casted volume.

The effect of GO solution concentration on GOF coating was also studied. The GO solution concentration was varied from 12 µg/µl to 0.5 µg/µl. The image of coated GOF with different concentration is shown in Figure 4.15. It can be seen that the transmission of GOF coated using higher solution concentration is lower. This is probably due to the increase in GO layers for GOF coated using high solution concentration. Figure 4.16 shows the average height of GOF produced using 1 drop of GO solution with different solution concentrations. The GOF thickness increases with increasing solution concentration. A second observation is the increase in thickness error bar, which is caused by the thickness different caused by the formation of wrinkles on the GOF. Figure 4.17 shows surface mapping of a GOF coated on SU-8 waveguides. Wrinkling on the GOF presents itself as lines with larger height on the film.

Figure 4.15: Image of drop-casted GOF with various GO concentrations (ranging from left 0.5, 0.75, 1, 1.5, 2, 3, 4, 6, 8, and 12 µg/µl).

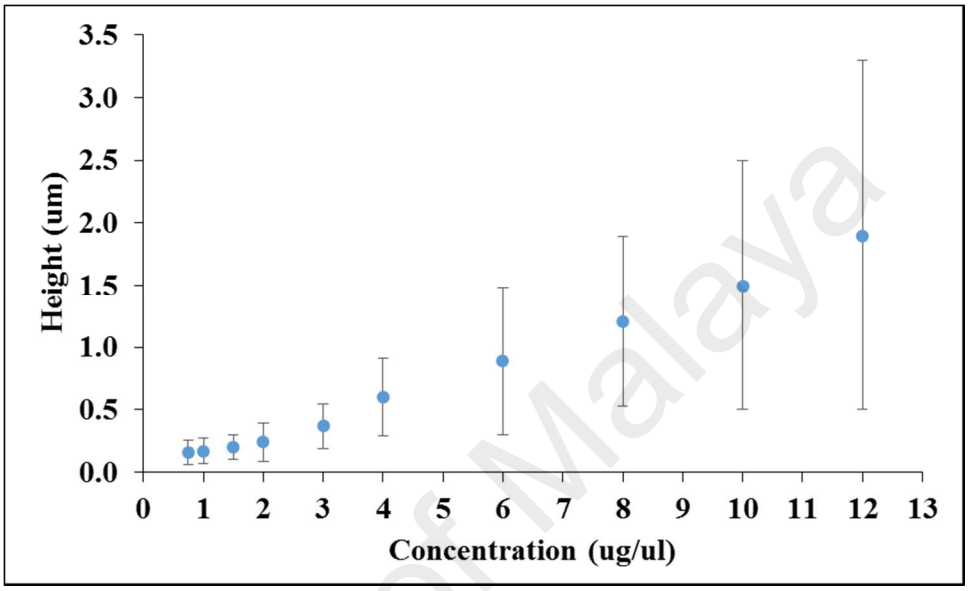

Figure 4.16: Height achieved for different concentration per drop.

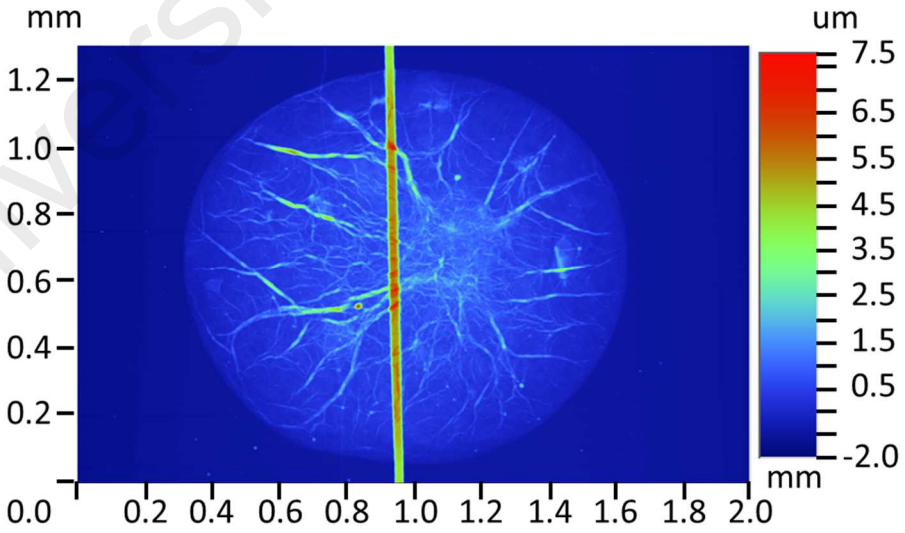

Figure 4.17: Surface mapping of GOF coated on waveguides.

Figure 4.18 shows the height profile across the GOF diameter coated using GO solution with different solution concentration. For high concentration, the coating thickness is not uniform, spherical cap shape was observed with very thick coated height of about 2.1 μm at the centre for concentration 12 μg/μl. For a medium concentration of between 1 - 4 μg/μl, this region give the best uniform coated area with a suitable height gain of 0.15 μm to 0.5 μm per drop, while concentration below that that gives poor uniformity as well as slow height gain. Note that, regardless of solution concentration used, wrinkles was observed due to the drying mechanism.

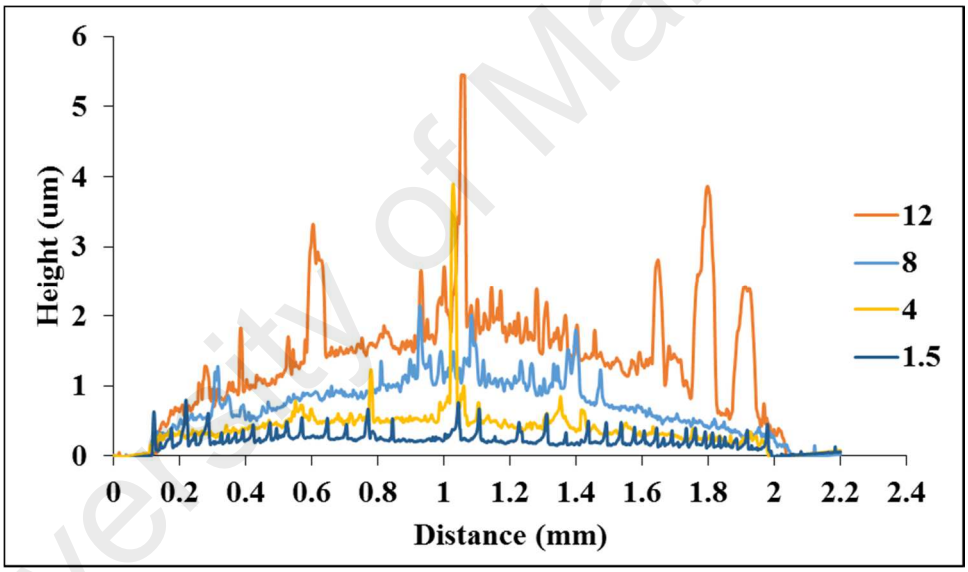

Figure 4.18: Height profile across the diameter of 4 selected concentrations (12, 8, 4, and 1.5 μg/μl).

There are reports showing that by adding ethanol into the GO solution, the formation of wrinkles can be reduced. Addition of ethanol into the GO solution reduces its surface tension, which results in a decrease of contact angle of the solution drop and eventually leads to reduced wrinkling of the GOF. However, the smaller surface tension also results in a larger coated region (when the solution volume used is fixed). Besides, if significant amount of ethanol was added to the GO solution, the overall GOF surface

profile changed from a “hill” to “doughnut” shape as shown in Figure 4.19. Compared with dilution using only DI water, the “hill” profile become flat top. Hence, in terms of coating uniformity in the microscopic level and concentration stability (ethanol evaporate faster), dilution using water is preferable.

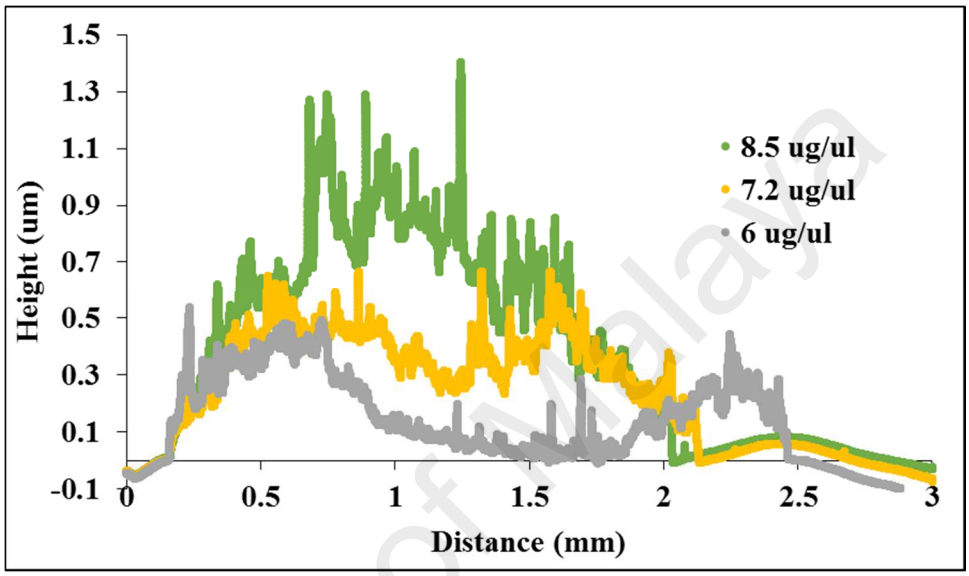

Figure 4.19: Height profile of 3 selected concentrations (8.5, 7.2, and 6 µg/µl) diluted using ethanol from 12 µg/µl GO solution.

Although smaller volume can be used to achieve smaller coating size, the trade-off is a smaller coating thickness. In order to achieve thick coating, multiple-drop-coasting technique was applied. However, multiple-drop-casting has its own drawback. As the droplet size is too small to be seen, there is difficulty in achieving good overlapping between subsequent drop-cast layers due to positioning inaccuracy during the droplet application process. In practice, a droplet was left to dry under room condition before the next droplet was applied onto the same area. As the film growed thicker after multiple-drop-casting, transparency of the GOF decreased as shown in Figure 4.1. Figure 4.20 shows the GOF height for various numbers of droplet application and different GO

concentrations. It was observed that the GOF height increased linearly with the number of droplet solutions applied during multiple-drop-casting process.

In conclusion, with good control of GO solution concentration, volume and number of drop-casting, uniform GOF with variable thickness and drop-casted region can be obtained.

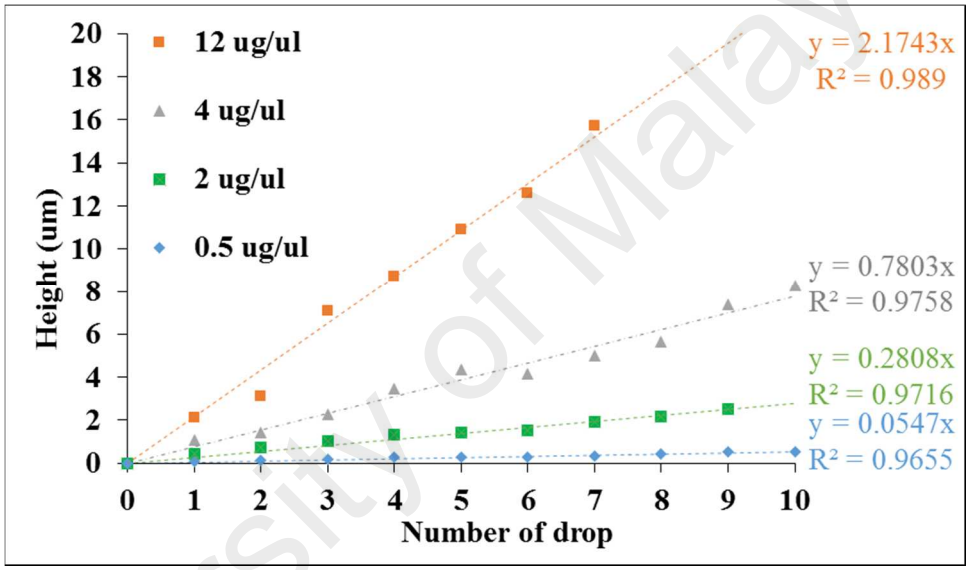

Figure 4.20: Height gain for different number of drops.

References

1. Stauber, T., N.M.R. Peres, and A.K. Geim, *Optical conductivity of Graphene in the visible region of the spectrum.* Physical Review B, 2008. **78**(8): p. 085432.

2. Li, Z.Q., et al., *Dirac charge dynamics in Graphene by infrared spectroscopy.* Nature Physics, 2008. **4**: p. 532.

3. Shen, Y., et al., *Evolution of the band-gap and optical properties of Graphene oxide with controllable reduction level.* Carbon, 2013. **62**: p. 157-164.

4. Bao, Q. and K.P. Loh, *Graphene Photonics, Plasmonics, and Broadband Optoelectronic Devices.* ACS Nano, 2012. **6**(5): p. 3677-3694.

5. Liu, M., et al., *A Graphene-based broadband optical modulator.* Nature, 2011. **474**: p. 64.

6. Bao, Q., et al., *Broadband Graphene polarizer.* Nature Photon., 2011. **5**: p. 411.

7. Kim, J.T. and C.-G. Choi, *Graphene-based polymer waveguide polarizer.* Opt. Express, 2012. **20**(4): p. 3556-3562.

8. Kim, J.T. and S.-Y. Choi, *Graphene-based plasmonic waveguides for photonic integrated circuits.* Opt. Express, 2011. **19**(24): p. 24557-24562.

9. Sun, P., et al., *Suppression of the coffee-ring effect by self-assembling Graphene oxide and monolayer titania.* Nanotechnology, 2013. **24**: p. 07561.

10. Dikin, D.A., et al., *Preparation and characterization of Graphene oxide paper.* Nature, 2007. **448**: p. 457.

11. Xingyi, H., et al., *Temperature-dependent electrical property transition of graphene oxide paper.* Nanotechnology, 2012. **23**(45): p. 455705.

12. Hummers, W.S. and R.E. Offeman, *Preparation of Graphitic Oxide.* Journal of the American Chemical Society, 1958. **80**(6): p. 1339-1339.

13. Staudenmaier, L., *Verfahren zur Darstellung der Graphitsäure.* Berichte der deutschen chemischen Gesellschaft, 1898. **31**(2): p. 1481-1487.

14. Brodie, B.C., *On the Atomic Weight of Graphite.* Philosophical Transactions of the Royal Society of London, 1859. **149**: p. 249-259.

15. Marcano, D.C., et al., *Improved Synthesis of Graphene Oxide.* ACS Nano, 2010. **4**(8): p. 4806-4814.

16. Bertolazzi, S., et al., *Exploring flatland: AFM of mechanical and electrical properties of Graphene, MoS2 and other low-dimensional materials*, in *Microscopy and Analysis*. 2013. p. 21.

17. Nemes-Incze, P., et al., *Anomalies in thickness measurements of Graphene and few layer graphite crystals by tapping mode atomic force microscopy.* Carbon, 2008. **46**(11): p. 1435-1442.

18. Paredes, J.I., et al., *Graphene Oxide Dispersions in Organic Solvents.* Langmuir, 2008. **24**(19): p. 10560-10564.

19. Huang, N.M., et al., *Simple room-temperature preparation of high-yield large-area Graphene Oxide.* Int. J. Nanomed, 2011. **6**: p. 3443.

20. Guo, Y., et al., *One pot preparation of reduced Graphene Oxide (RGO) or Au (Ag) nanoparticle-RGO hybrids using chitosan as a reducing and stabilizing agent and their use in methanol electrooxidation.* Carbon, 2012. **50**(7): p. 2513-2523.

21. Ferrari, A.C. and J. Robertson, *Interpretation of Raman spectra of disordered and amorphous carbon.* Phys. Rev. B, 2000. **61**(20): p. 14095-14107.

22. Pimenta, M.A., et al., *Studying disorder in Graphite-based systems by Raman spectroscopy.* Phys. Chem. Chem. Phys., 2007. **9**(11): p. 1276-1290.

23. Acik, M., et al., *The Role of Intercalated Water in Multilayered Graphene Oxide.* ACS Nano, 2010. **4**(10): p. 5861-5868.

24. Si, Y. and E.T. Samulski, *Synthesis of Water Soluble Graphene.* Nano Letters, 2008. **8**(6): p. 1679-1682.

25. Wang, D.-W., et al., *A water-dielectric capacitor using hydrated Graphene Oxide film.* Journal of Materials Chemistry, 2012. **22**(39): p. 21085-21091.

26. Cerveny, S., et al., *Dynamics of Water Intercalated in Graphite Oxide.* The Journal of Physical Chemistry C, 2010. **114**(6): p. 2604-2612.

27. Buchsteiner, A., A. Lerf, and J. Pieper, *Water Dynamics in Graphite Oxide Investigated with Neutron Scattering.* J. Phys. Chem. B, 2006. **110**(45): p. 22328-22338.

28. Lerf, A., et al., *Hydration behavior and dynamics of water molecules in graphite oxide.* Journal of Physics and Chemistry of Solids, 2006. **67**(5–6): p. 1106-1110.

29. Jung, I., et al., *Characterization of Thermally Reduced Graphene Oxide by Imaging Ellipsometry.* The Journal of Physical Chemistry C, 2008. **112**(23): p. 8499-8506.

30. Riegler, H., *A user's guide to ellipsometry. By Harland G. Tompkins, Academic Press, New York 1993, 260 pp. hardback, ISBN 0-12-603050-0.* Advanced Materials, 1993. **5**(10): p. 778-778.

31. Azzam, R.M.A. and N.M. Bashara, *Ellipsometry and polarized light*. 1977: North-Holland Pub. Co.

32. Peres, N.M.R., T. Stauber, and A.H. Castro Neto, *The infrared conductivity of Graphene.* EuroPhysics Letters, 2008. **84**: p. 38002.

33. Stankovich, S., et al., *Synthesis of graphene-based nanosheets via chemical reduction of exfoliated graphite oxide.* Carbon, 2007. **45**(7): p. 1558-1565.

34. Pantazopoulou, A. *Simulation of Graphene-based Nano-antennas*. Available from: http://www.n3cat.upc.edu/presentations/Anastasia-Simulation_of_graphene-based_nano-antennas.pdf.

35. Carbotte, J.P., V.P. Gusynin, and S.G. Sharapov, *AC Conductivity of Graphene: From Tight-Binding Momel to 2 + 1-Dimensional Quantum Electrodynamics.* International Journal of Modern Physics B, 2007. **21**(27): p. 4611-4658.

36. Hanson, G.W., *Dyadic Green's functions and guided surface waves for a surface conductivity model of Graphene.* J. Appl. Phys., 2008. **103**(6): p. 064302.

37. Hong, J.T., et al., *Terahertz conductivity of reduced Graphene oxide films.* Opt. Express, 2013. **21**(6): p. 7633-7640.

38. Vaupel, M. and U. Stoberl. *Appication note: Graphene and Graphene Oxide*. Accurion solutions for science; Available from: http://www.nanofilm.de/sales-support/downloads/application-notes/applicationnote_graphene.pdf.

39. Nair, R.R., et al., *Unimpeded Permeation of Water Through Helium-Leak–Tight Graphene-Based Membranes.* Science, 2012. **335**(6067): p. 442-444.

40. Jung, I., et al., *Effect of Water Vapor on Electrical Properties of Individual Reduced Graphene Oxide Sheets.* The Journal of Physical Chemistry C, 2008. **112**(51): p. 20264-20268.

41. Yavari, F., et al., *Tunable Bandgap in Graphene by the Controlled Adsorption of Water Molecules.* Small, 2010. **6**(22): p. 2535-2538.

42. Lipatov, A., et al., *Highly selective gas sensor arrays based on thermally reduced Graphene Oxide.* Nanoscale, 2013. **5**(12): p. 5426-5434.

43. Cote, L.J., R. Cruz-Silva, and J. Huang, *Flash Reduction and Patterning of Graphite Oxide and Its Polymer Composite.* Journal of the American Chemical Society, 2009. **131**(31): p. 11027-11032.

44. Pop, E., et al., *Negative Differential Conductance and Hot Phonons in Suspended Nanotube Molecular Wires.* Physical Review Letters, 2005. **95**(15): p. 155505.

45. Begtrup, G.E., et al., *Probing Nanoscale Solids at Thermal Extremes.* Physical Review Letters, 2007. **99**(15): p. 155901.

46. Mohammed, O.F., P.C. Samartzis, and A.H. Zewail, *Heating and Cooling Dynamics of Carbon Nanotubes Observed by Temperature-Jump Spectroscopy and Electron Microscopy*. Journal of the American Chemical Society, 2009. **131**(44): p. 16010-16011.

47. Guo, H., et al., *Preparation of reduced Graphene oxide by infrared irradiation induced photothermal reduction.* Nanoscale, 2013. **5**(19): p. 9040-9048.

48. Acik, M., et al., *Unusual infrared-absorption mechanism in thermally reduced Graphene oxide.* Nat Mater, 2010. **9**(10): p. 840-845.

49. Ryu, S., et al., *Atmospheric Oxygen Binding and Hole Doping in Deformed Graphene on a SiO2 Substrate.* Nano Letters, 2010. **10**(12): p. 4944-4951.

50. Deegan, R.D., et al., *Capillary flow as the cause of ring stains from dried liquid drops.* Nature, 1997. **389**.

51. Yunker, P.J., et al., *Suppression of the coffee-ring effect by chape-dependent capillary interaction.* Nature, 2011. **476**: p. 308.

CHAPTER 5: GRAPHENE OXIDE WAVEGUIDES POLARISER: MOTIVATION

Polarisation control is one of the essential functions required in the realization of Photonic Integrated Circuits (PICs) [1]. In addition, polarisation control is also required in optical fibre communication systems that exploit polarisation diversity to increase capacity [2]. Most high index-contrast optical waveguides currently used as platforms for PIC fabrication exhibit intrinsic birefringence, which limits the sensitivity and coherence, as well as the bandwidth, of the functional circuits required in applications such as optical sensing and optical signal processing [1, 3]. Devices may be needed to control the polarisation state of light propagating in these circuits, either actively or passively. Two approaches have been proposed and demonstrated in an effort to alleviate these limitations. The first is to control the birefringence of the waveguide structure, either by making it birefringence-free or by using polarisation compensation mechanisms [3-5] – while the second approach is to place an integrated polariser at the input of the PIC, in order to allow only one state of polarised light to propagate in the circuit [6-8].

The principal of integrated polariser is to make one polarisation mode "lossier" than the other, either by leakage or absorption loss, thereby achieving a large difference in propagation loss between two orthogonally polarised modes. As a consequence, a large extinction ratio – defined as the ratio of the power in the desired polarisation to the power in the undesired polarisation – can be achieved. Previous approach has used the strong polarisation dependence propagation of plasmonic modes in metal-dielectric waveguides to suppress one of the polarisations [9]. High extinction ratio between orthogonally polarised modes can be achieved using metal-cladding based integrated waveguide polarisers. However, the effect is wavelength dependent, requires complex structures and

the incorporation of resonant buffer layers in order to produce the broadband polarisation response, thus increasing the complexity of PIC fabrication.

In recent years, Graphene has attracted much attention in photonics applications due to its exceptional electronic transport and related optical properties. The conductance of Graphene is defined by the fine structure constant and is independent of frequency over a wide range. Bao et. al. have demonstrated a broadband fibre polariser by replacing the metal thin film in the polarising waveguide with a Graphene layer [10]. Later, Kim et. al. demonstrated a planar waveguide using Graphene core waveguides [11] and subsequently the polarisation-dependent coupling of plasmonic modes at the waveguide-Graphene interface of polymer waveguides [12]. These results represent promising successes towards the realization of PIC devices and show that Graphene photonics plays an important role in optical waveguide device technology.

Coincidentally, it has recently been shown that GOF typically exhibits a strongly anisotropic complex dielectric function [13]. This property was demonstrated in FET-type electronic devices. At optical frequencies, such dielectric anisotropy may be expected to lead to differences in the propagation loss for different polarisation states, which can be used to provide the function of polarisation selection in an optical waveguide. It is therefore logical for these properties of GOF to be explored for applications such as waveguide polarisers. It is worth noting that this work has been published in Optic Express [14].

5.1 Graphene Oxide Waveguide Polariser (GOWP)

5.1.1 Fabrication and Optical Characterization Setup

GOWP uses the anisotropic complex dielectric function of GOF to induce high propagation loss to the TE-mode. The fabrication process is relatively easier than previously reported Graphene-based waveguide polariser. A 5 μm thick of SU-8 was spin coated and patterned using contact photolithography onto the CR-39 substrate to produce SU-8 channel waveguide. The details of sample cleaning, and spin coating process have been discussed in chapter 3. Before the SU-8 channel was covered with NOA overcladding, a controlled volume of GO solution was drop-casted onto the channel and allowed to dry under ambient condition to form GOF. GOF with various thicknesses was coated onto the SU-8 waveguide using GO solution with different solution concentration and by applying additional number of solution drops. All GOWP chip has a similar length of about 0.9 ± 0.05 cm after dicing and polishing as shown in Figure 5.1.

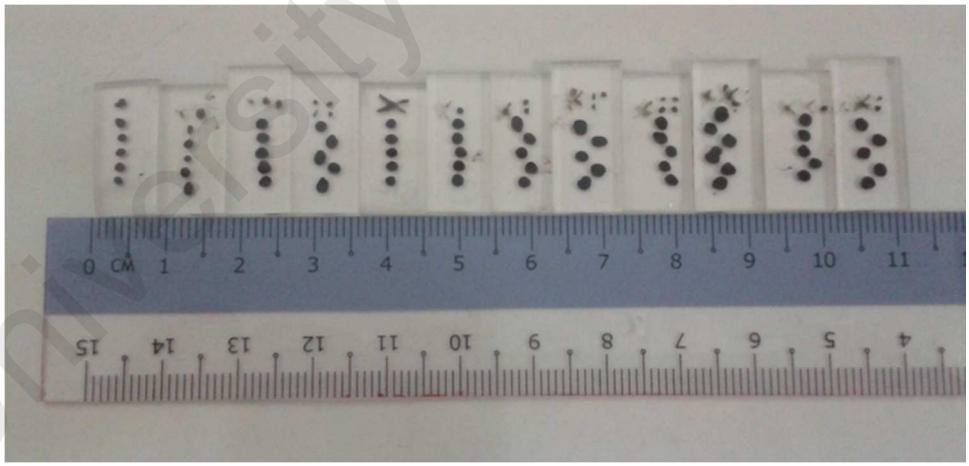

Figure 5.1: Image capture of GOWP chip.

The characterization setup for GOWP is shown in Figure 5.2. The fibre output from Tunable Light Source (TLS) was connected to a Polarisation Controller (PC) to control the light polarisation state in the fibre before it was launched into the GOWP. The output of the GOWP was coupled out to free space (its optical path shown as dotted line

in Figure 5.2a) via an objective lens to a polarimeter to measure its polarisation state. The transmitted power of a particular polarisation state was measured by coupling the GOWP output to an output fibre which was in turn connected to an optical power meter as shown in Figure 5.2b.

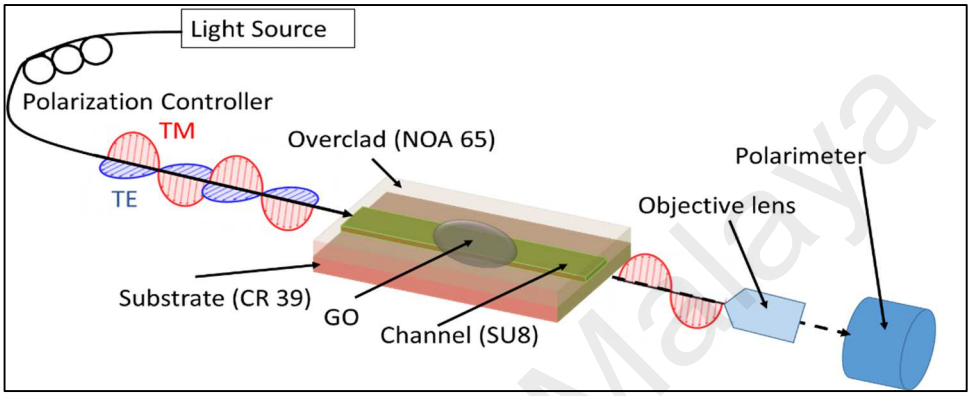

a)

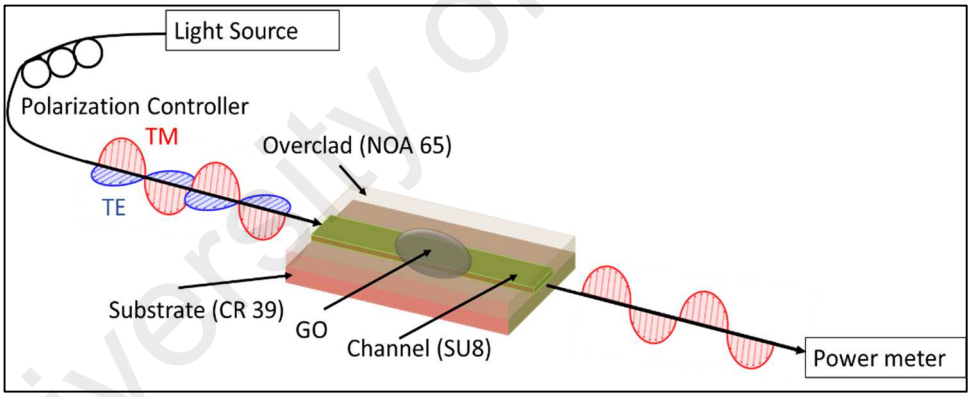

b)

Figure 5.2: Characterization setup for GOWP. a) Polarimeter measurement and b) insertion loss measurement.

5.1.2 Results and Discussion

Figure 5.3 shows the polar plot of the GOWP measured using 1550 nm laser source. The GOF was oriented horizontal with reference to the polar plot. It can be seen that light with polarisation parallel to the GOF (TE-polarised) experienced a very high

insertion loss of more than 40 dB, while the insertion loss of orthogonal polarisation mode (TM-polarised) was ~10dB. This translates into an extinction ratio of more than 30 dB. To visualise the propagation of both polarised modes in the GOF, 650 nm visible laser source was coupled into the GOWP and a long working distance microscope was used to image the GOWP in the light propagation direction. The micrographs were shown in Figure 5.4. When TM-polarised light was coupled into the GOWP, scattering of light from the GOF covered waveguide section was observed. The scattered light from the waveguide was not uniform along the waveguide length due to the existence of wrinkles on the GOF. The polarisation state of the scattered light was analysed by placing a free space polariser between the GOWP and the microscope, and was found to be in the p-polarisation state (i.e. parallel to the plane of incident – the plane defined by the waveguide axis and the direction of the microscope observation). However, when TE-polarised light was coupled into the GOWP, no scattering was observed. This observations indicated that the TM–polarised light was coupled into and propagate partially in the GOF with relatively small propagation loss while TE-polarised light experienced a much larger propagation loss in GOF.

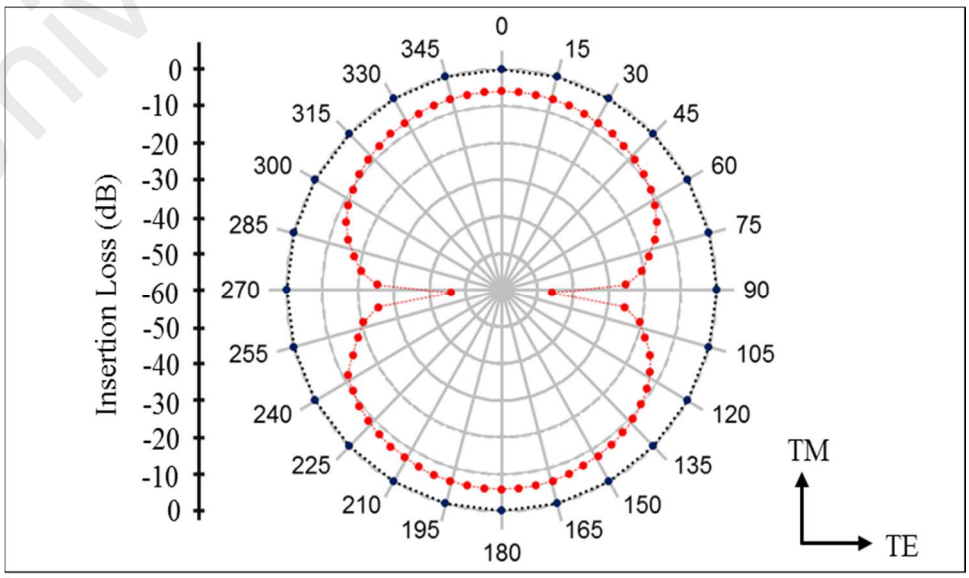

Figure 5.3: Polar plot of GOWP.

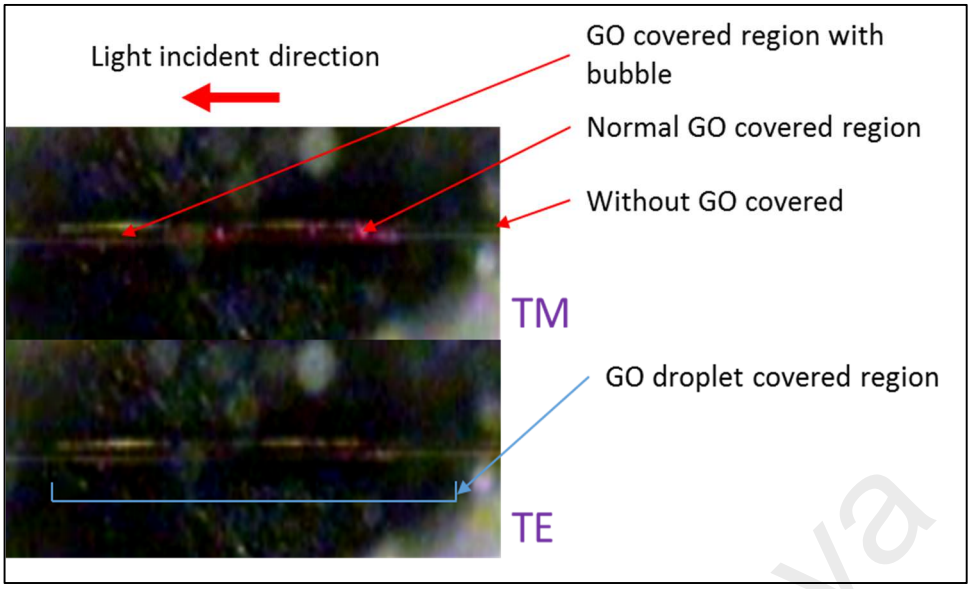

Figure 5.4: Top view of GOWP with TM- and TE-polarised light propagating through the waveguide.

Figure 5.5 shows the insertion loss of both TE- and TM-mode of the GOWP with different thickness of GOF. It was observed that the highest extinction ratio was achieved with a GOF thickness of about 2 μm. The polarisation performance of this sample (with the highest extinction ratio) was then investigated at different wavelengths to assess its broadband response. The result was shown in Figure 5.6. The GOWP showed the highest extinction ratio of 40 dB at 1590 nm, which then gradually decreased to about 8.5 dB at 650 nm. The lower extinction ratio at shorter wavelengths is believed to be a result of the excitation of higher order modes at shorter wavelength and the reduced coupling of these modes into the GOF. Although precaution steps have been taken to ensure only fundamental mode propagation in the GOWP, towards the shorter wavelengths, excitation of higher order modes was inevitable and led to reduced coupling between polymer waveguide and GOF. The decrease in extinction ratio may also be due to decreased conductivity of GOF, which will be discussed in following section.

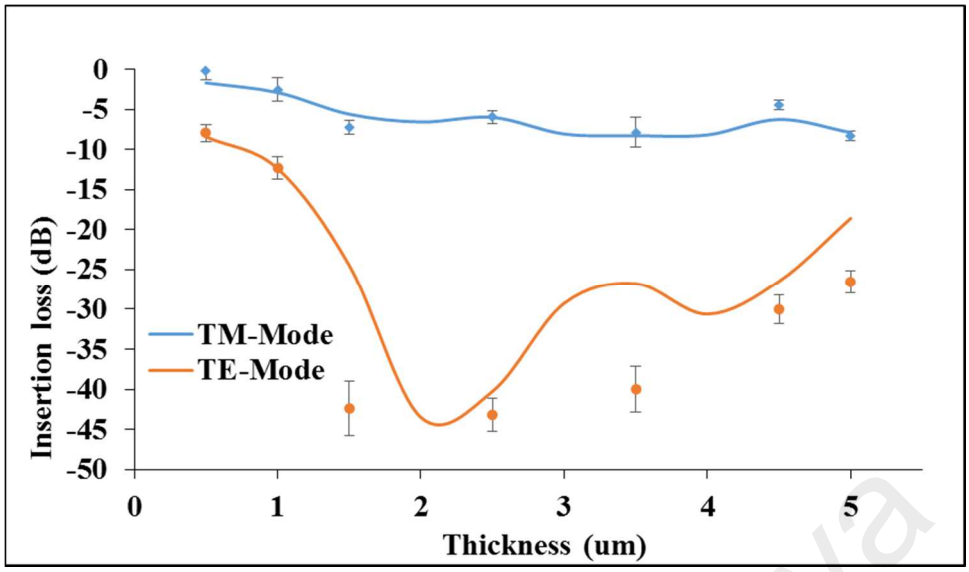

Figure 5.5: Insertion loss of TE- and TM-polarised light of GOWP coated with different film thickness at 1550 nm. The solid line is the simulation results.

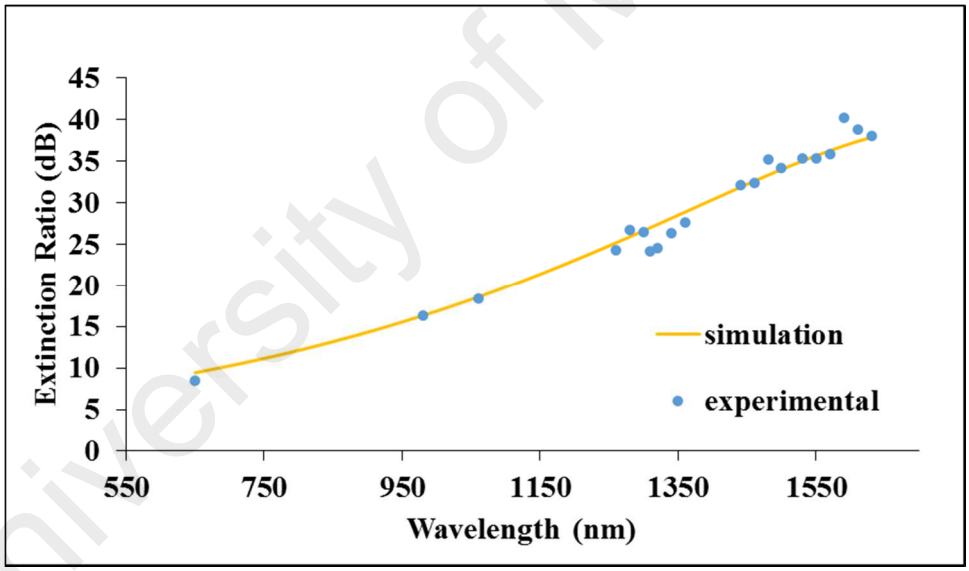

Figure 5.6: Broadband response of GOWP. The solid line is the simulation fitting result.

5.1.3 Simulation Model

5.1.3.1 Simulation Model Setup

Based on the observations above, wave propagation in the GOWP was modelled to provide a better understanding of the polarising effect. Intuitively, TM- and TE-polarised light propagating in the GOWP should encounter similar absorption as the GOF was expected to be in contact with the top surface as well as the sidewalls of the channel waveguide. In this case, TE-polarised light which is also oriented parallel to the GOF on top of the channel and perpendicular to the GOF at the sides of the channel. The opposite applies to TM-polarised light, where it was oriented perpendicular to the GOF on top of the channel and parallel to the GOF at the sides of the channel. In the GOWP, however, the difference in propagation loss between the two orthogonal modes is very large. A look at how the GOF was coated onto the channel waveguide explained this observation. Figure 5.7 shows FESEM images of the GOF coated channel waveguide. From Figure 5.7a, it can be seen that the GOF coating on the SU-8 waveguide was wedge-shaped instead of following the rectangular shape of the waveguide. A closer look at the edge of the GOF coating on the waveguide reveals the existence of air gaps at both sides of the channel sidewall, as shown in Figure 5.7b-c. These air gaps prevent the channel side wall to be in physical contact with the GOF. The air gap was created during the drying phase of the GO drop-casting process. As mentioned in chapter 4, after a drop of GO solution was drop-casted onto a surface, GO flakes will be drawn towards the air – water boundary to form a "blanket-like" GOF. The GOF will eventually collapse onto the surface at the end of the second drying stage. When there exist a "protruding" structure on the surface (in this case the channel waveguide), air gaps will be created between the GOF and the structure sidewall as the GOF collapse onto the surface. To verify this observation, GOF from a GOWP sample with overcladding was removed using sheer force and the surface morphology of the GOF formerly attached to the SU-8 waveguide channel was observed

using FESEM. The image is shown in Figure 5.7d. The indentation at the centre of Figure 5.7d was imprinted by the SU-8 waveguide. It can be seen that the sidewall of the indentation is not at right angle but was a slope. As the SU-8 waveguide sidewall angle was close to 90°, the slope indicates the existence of a void between the SU-8 waveguide sidewall and the neighbouring GOF coating. It was also observed that the air gap formed was consistent along the coating length provided the coating conditions are identical.

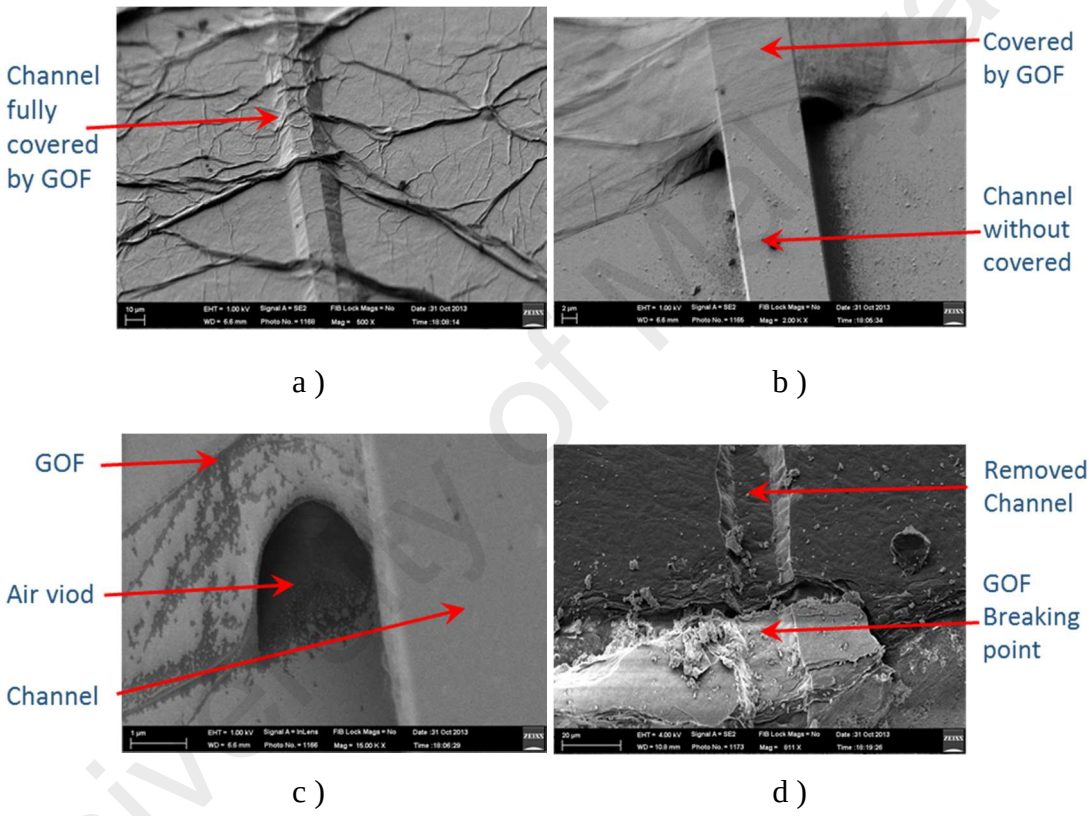

Figure 5.7: FESEM micrograph of GOWP. a) Top view at the middle of GOWP, b) top view at the edge of GOF, c) higher magnification on the channel side wall, an air void was observed, and d) GOF internal surface morphology that was attached to the waveguide surface.

Using the information obtained, the simulation model was created as shown in Figure 5.8. By using Comsol, both real and complex dielectric functions of the waveguide effective modes with various GOF thickness were simulated. Air has a refractive index of 1.000, while the refractive indices of CR-39, SU-8, and NOA65 were obtained using

Prism Coupling measurement to be 1.486, 1.569 and 1.520 respectively, at 1550 nm. To simplify the model, all 4 materials above were assumed to be lossless, where the imaginary part of their refractive index were assumed to be zero. However, it is difficult to measure the optical properties of the GOF for both TM- and TE-mode. To date, there are no literatures reporting on the GOF optical properties at our frequency of interest. Therefore, assumptions were made on these values as follow. The best fitted real part of the refractive index was assumed to be 2, which corresponds to 4 for the real part of the dielectric function. This assumption is in reasonable conformity with the value given by Vaupel and Stoble [15] and is an intermediate value by comparison with refractive index value that would be obtained from the low-frequency value for the dielectric function given by Loh [16].

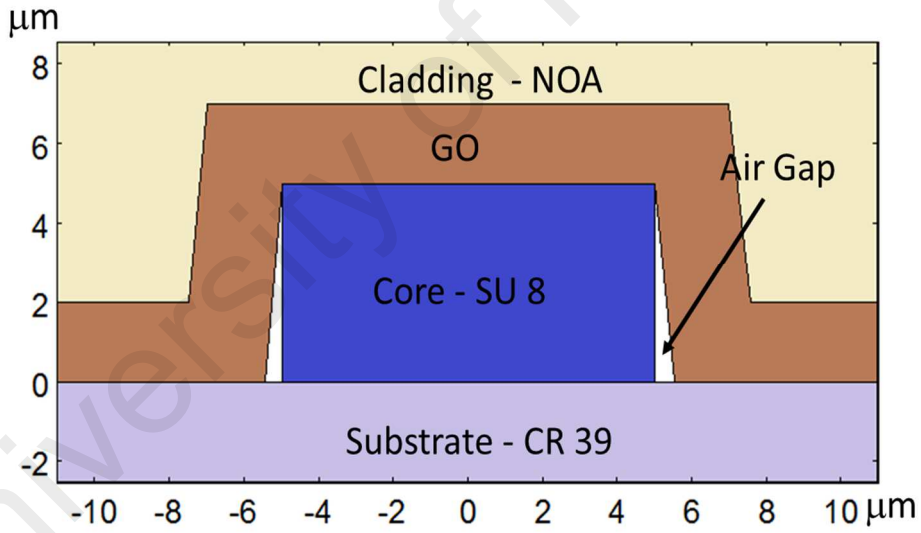

Figure 5.8: Simulation model of cross-section of the GOWP.

The imaginary part of the refractive index – which is related to conductivity, is dependent on the optical electric field component. For incident electric field perpendicular to the GO layers, the GOF is assumed to be perfect dielectric. However, for incident electric field parallel to the GO layers, high conductivity value should be used because the electrons in each GO flakes are being excited. Since GOF are made from

stacking of few hundred layers of GO at sub-wavelength scale, effective or average medium approach is appropriate to be applied in this case. The conductivity of pure Graphene derived from Kubo expression is about 1.8 x 10^5 S.m^{-1}. With doping, like in GO, this conductivity should be lower as predicted by Peres [17] as shown in Figure 5.9. It would not be surprising that for bandgap tuning of upto 2 eV via chemical doping, the conductivity will drop to only 10% of its initial value at the wavelength of 1550 nm (6500 cm^{-1}). The value of σ = 2700 S.m^{-1} was chosen, which best fits the experimental results. This value implied that the absorption coefficient for TE-polarised light is very significant. The chosen value is slightly larger than the DC or low frequency value given by Stankovich (2420 S.m^{-1}) [18], Si (1250 S.m^{-1}) and Pantazopoulou (1670 S.m^{-1}) [19] (in her simulation presentation slide in which derived from [20, 21]), but smaller than the value (9000 S.m^{-1}) given by Hong [22] at THZ frequency.

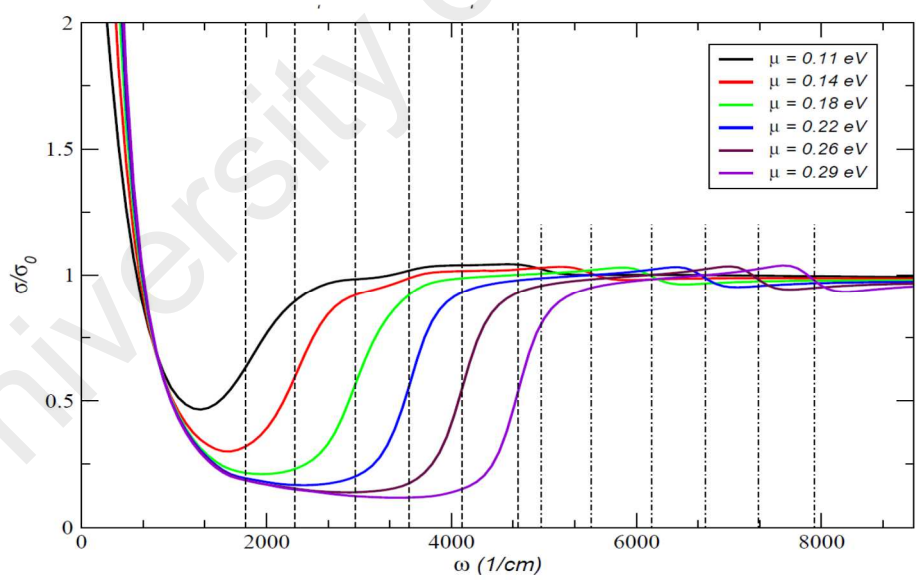

Figure 5.9: Effect of doping (μ) on conductivity of Graphene at infrared frequency. [17]

Another assumption made in the simulation was that the GOF was uniformly coated along the waveguide length. It is worth noting that the value used in the simulation length is obtained from experimental results, taken from the average of several drop-

casted lengths, which is about 1.2 mm. This assumption simplified the model and enabled the insertion loss of the both TM- and TE-mode can be estimated using Beer-Lambert law,

$$I = I_o \exp(-4\pi.n_r\alpha z/\lambda) \ldots. \quad \text{Eqn 5.1}$$

where α = absorption coefficient and n_r = real refractive index, λ = wavelength, and z = coating length.

5.1.3.2 Fitting of Simulation Model

The simulation result, using to the above model and refractive index of 2 and conductivity of 2700 Sm^{-1} for GOF, was shown in Figure 5.10. The GOF itself can be seen as another waveguide core which can support different number of modes with different thickness. It was observed that maximum TE-mode absorption occurred at the same GOF thickness of 0.2 μm, 0.8 μm, ~1.3 μm and so on. The first absorption peak is due to plasmonic effect while other peaks correspond to the guided modes in GOF. For example, absorption peak at 0.8 μm is due to fundamental guided mode, 1.4 μm corresponds to 1st order guided mode in the GOF and so on. Figure 5.11 shows the cross section electric field distribution of the GOWP with 2 μm thick GOF. The model showed that both modes are coupled and guided by the GOF. A relatively high damping was experience by the TE–mode, which led to a high polarisation extinction ratio in the GOWP.

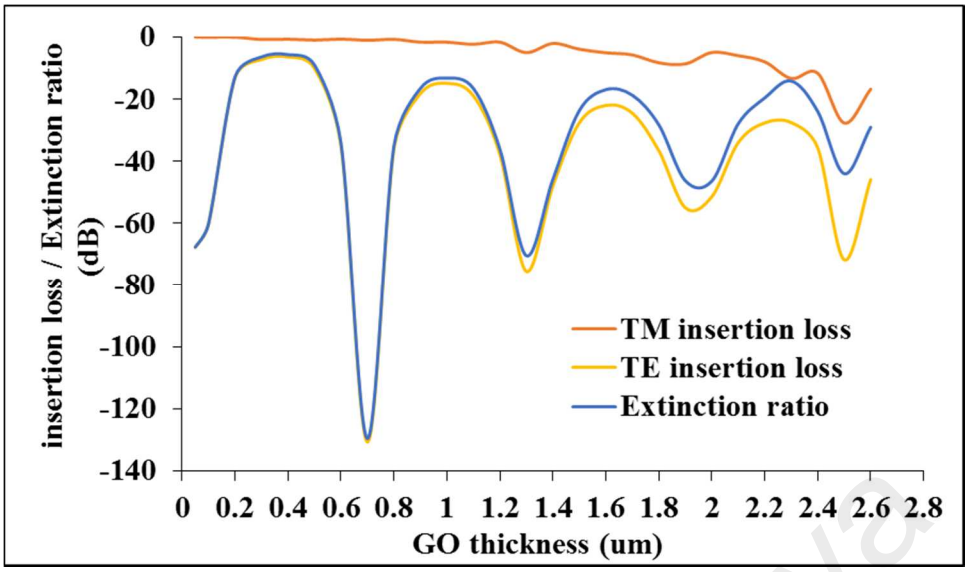

Figure 5.10: Simulation model of GOWP for both TE- and TM-mode propagating loss and their different (extinction ratio).

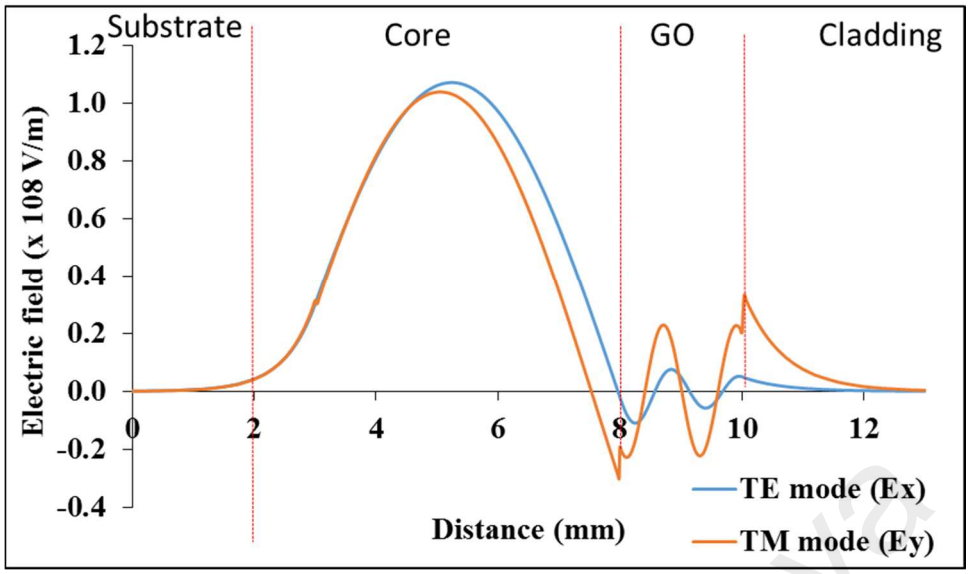

a)

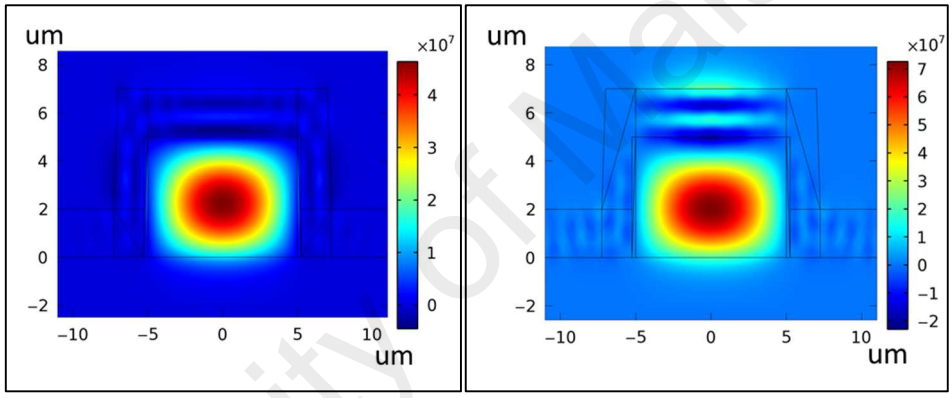

b) c)

Figure 5.11: Simulation model of Electric field component distribution of a) both TE– and TM–mode across the channel axis and b) Ex plot of TE-mode, c) Ey plot of TM-mode at the channel cross section for GOF of 2 µm.

The effect of mode coupling in GOF due to changes of refractive index, conductivity and GOF thickness was then studied. It can be seen from Figure 5.11 that the absorption profile for both TM– and TE–mode is similar, but with different absorption strength (TE-mode experienced significantly larger absorption). Therefore, only TE-mode coupling in the GOF was discussed. Figure 5.12 shows the effect of GOF conductivity - ranging from 1500 to 10,000 Sm^{-1} - on TE-mode absorption, with the refractive index fixed at 2. It was observed that maximum TE-mode absorption occurred

at the same GOF thickness regardless of GOF conductivity. The absorption strength of higher order guided modes are smaller compared to the fundamental guided mode due to smaller energy confinement inside the GOF for higher order modes. Figure 5.13 shows the change in TE–mode absorption with different GOF thickness when the refractive index of GOF was set at 1.9, 2.0 and 2.1. For higher refractive index, the position where maximum absorption occurred shifted towards larger GOF thickness, accompanied by increasing peak-to-peak spacing. This shift is due to changes to the overall effective waveguide mode.

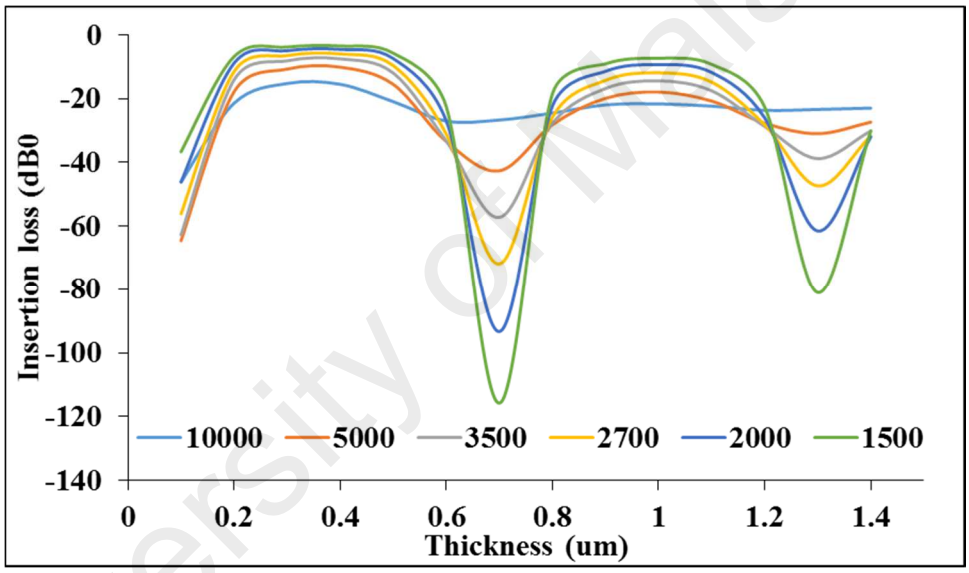

Figure 5.12: Effect of conductivity of GOF on TE–mode absorption.

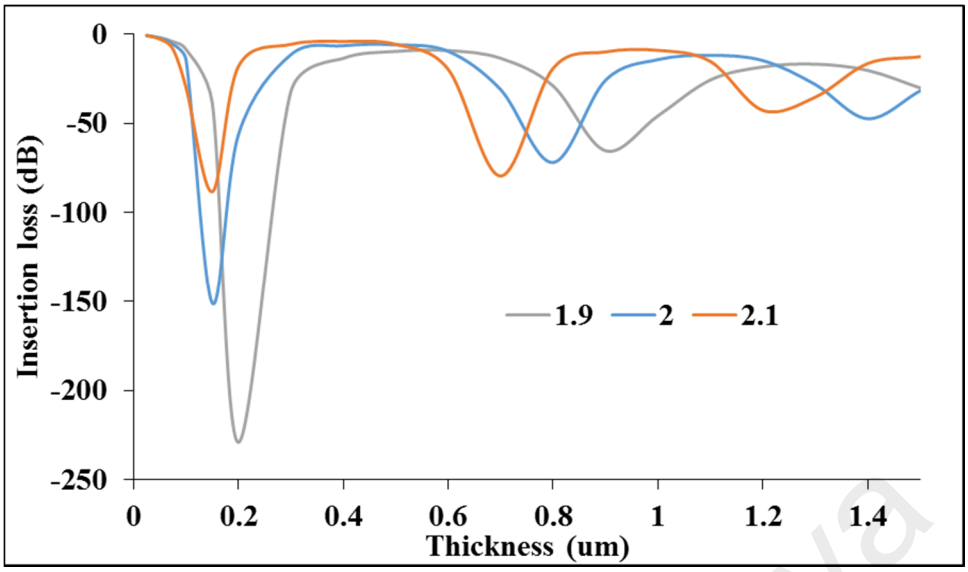

Figure 5.13: Effect of refractive index of GOF on TE–mode absorption.

Using information obtained from the simulation model in Figure 5.10, we repeated the experiment with careful control on the GOF thickness and the best fit results was shown in Figure 5.14. The best fitting parameter of GOF properties were refractive index of 2 and conductivity of < 2700 Sm^{-1}. Note that the simulation results showed larger polarisation extinction ratio of more than 100 dB for the fundamental guided mode. However, the experimental results were limited by the launch power of the laser source (~ 0 dBm) and the sensitivity of the optical power meter used (~ -50 dBm) which limit the maximum measurable extinction ratio to less than 50 dB. In addition, assumptions made in the simulation such as uniform GOF coating also result in a larger TE-mode absorption loss.

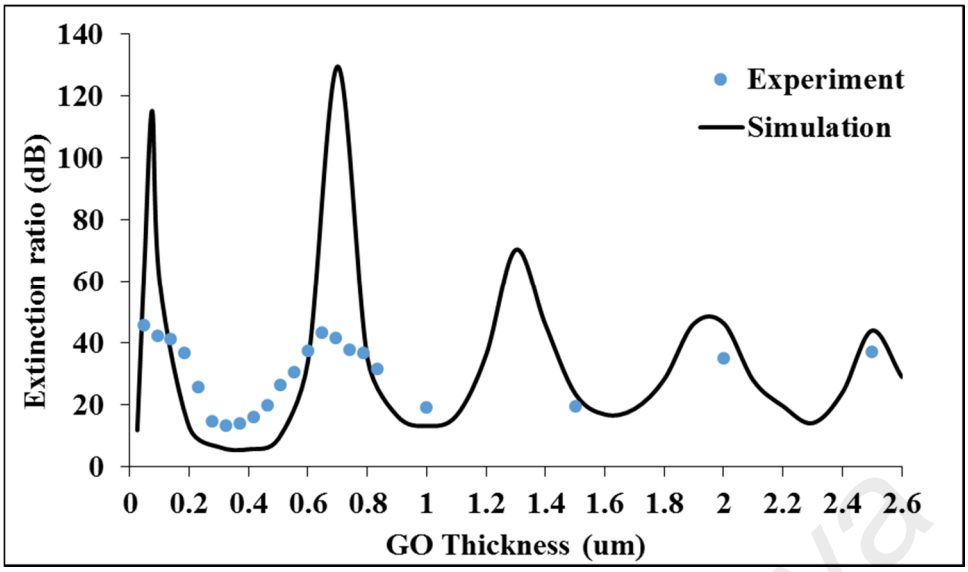

Figure 5.14: Simulation and experimental result of extinction ratio.

To study the wavelength dependency of the GOWP, we make assumption of conductivity dependent in GOF according to [23]

$$\sigma_w = \frac{8\,\mu_c}{hw}\,\sigma \qquad \text{Eqn 5.2}$$

where μ = doping level of the GOF, h = Plank constant and w = angular frequency. With this wavelength dependent coefficient, the imaginary part of the GOF refractive index was simulated and is shown in Figure 5.15. Given a fix GOWP cross section with fix GOF thickness, higher order modes will be supported for lower wavelength. For example, the n^{th} mode occurred at 1600 nm, then the $(n+1)^{th}$ mode occurred at ~1200 nm and so on. The wavelength in between these two modes will undergo mode expansion of n^{th} mode throughout the GOF and mode conversion to $(n+1)^{th}$ mode. Therefore, it will encounter lesser energy confinement and hence lesser optical absorption. Besides, the energy confinement for higher order mode is smaller at shorter wavelengths. Therefore, the optical absorption of longer wavelengths is, in general, higher. However, the simulation result did not show a "linear trend" as in the experimental results as shown in Figure 5.6. This is because during the simulation, the assumption of uniform GOF coating was made. In fact, the surface morphology of the GOF showed a flat-top profile, followed

by tapering in thickness towards the edge, as discussed in section 4.2.2. Hence, the actual mode conversion observed will not be as sharp as in the simulation results. By taking the average of the simulation results, the simulation model shows good agreement with the experimental results.

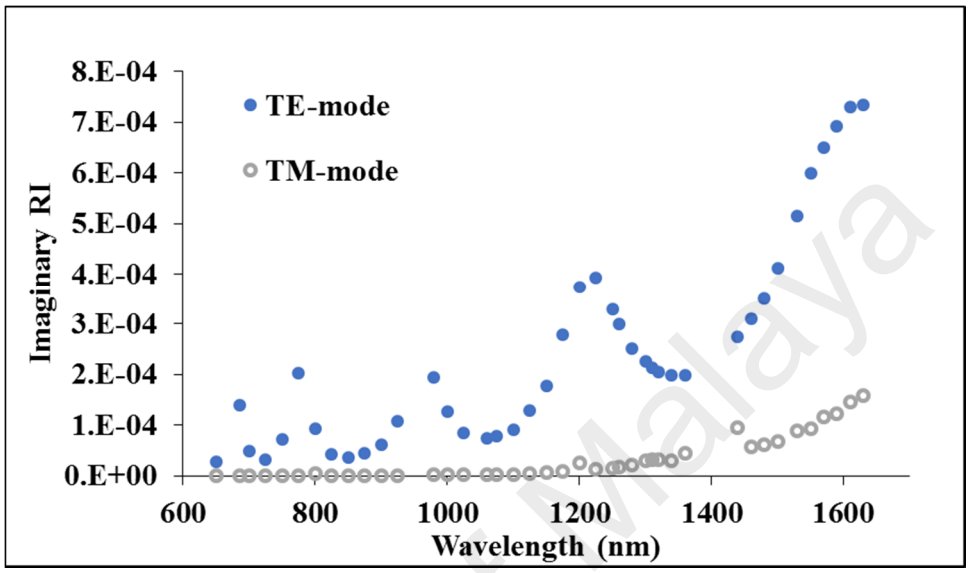

Figure 5.15: Simulation of wavelength dependent imaginary refractive index of the GOWP for both TE- and TM-mode.

5.1.3.3 Effect of Waveguide Dimension

To study the effect of waveguide dimension on the GOWP performance, the waveguide width was varied between 5 μm and 15 μm. It was observed that the polarisation extinction ratio of the GOWP is insensitive to waveguide width variation within this range. With these index contrast and waveguide dimensions, the waveguide can support a number of higher order modes. However, as the GOWP was constructed by a straight channel with a length of less than 5 mm, excitation of higher order modes in the GOWP can be avoided by careful alignment between the input fibre and the GOWP. Excitation of higher order mode is believed to have a large effect on the TE-mode absorption as the energy distribution is pushed outward from the centre of the waveguide core.

Simulation has been carried out and in order for waveguide to operate in single mode, waveguide dimension of less than 3.5 μm in width and height are required. GOWP that with these dimensions was also successfully fabricated and characterised. However, high insertion loss of ~15 dB was observed. The high insertion loss is due to Numerical Aperture (NA) and Mode Field Diameter (MFD) mismatch between the GOWP and SMF-28 fibres. With a launch power of 0 dBm, and sensitivity of power meter about -50 dBm, only 50 dB of dynamic range was available for measurement. If the insertion loss is larger than 10 dB, GOWP that has an extinction ratio higher than 30 dB cannot be measured accurately using the current setup.

Two approaches were considered to improve the measurement dynamic range. The first approach was to increase the launch power either by using a higher power optical source or by amplifying power of the current laser source using an Erbium-Doped Fibre Amplifier (EDFA). However, higher power laser source with high Signal-To-Noise (SNR) ratio was not readily available (current laser source has a SNR of 45 dB). On the other hand, amplification of the launch power with EDFA can push up the total power to about 10 dBm. In this case, the configuration of the input source (the arrangement of EDFA amplifier and PC) is important. If configured in Figure 5.16a, the polarisation extinction ratio of the EDFA output will reduced because other unwanted polarisation modes were being amplified as well. For example, extinction ratio of a tested GOWP dropped from 35 dB - without amplification, to 8 dB when an amplified input source was used. On the other hand, when configured as in Figure 5.16b, only 1 polarisation mode will be amplified. However, the SNR remained about the same as in TLS light source after amplification as shown in Figure 5.17. In other words, the background noise gets

amplified as well, hence SNR remained the same and this limited the polarisation extinction ratio.

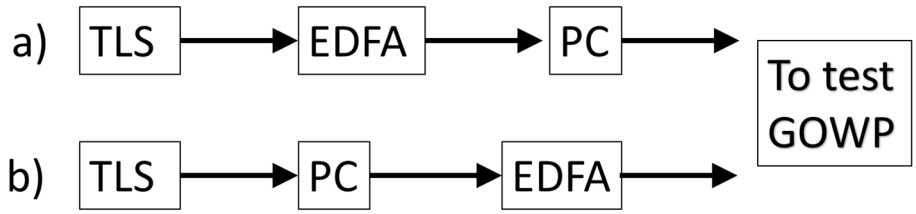

Figure 5.16: Configuration of light source amplification by EDFA.

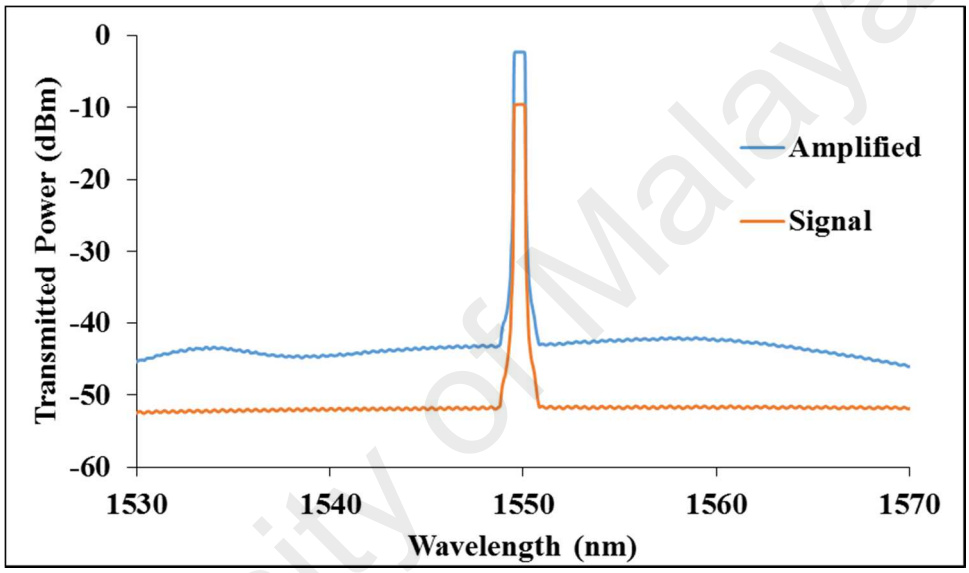

Figure 5.17: EDFA amplification of TLS signal. A 10 dB fix attenuator was placed between the EDFA output and OSA to prevent damage to the OSA.

The second approach was to reduce the coupling loss of the GOWP by matching its NA and MFD using high NA fibre (UHNA 4 with NA of 0.35). This method has successfully reduces the coupling loss by about 12 dB as discussed in chapter 3. When applied on to the small core single mode GOWP, comparable extinction ratio to larger core (5 x 5 μm) GOWP was obtained. Therefore, the production of low insertion loss single mode GOWP is feasible, which in turn enables the incorporation of GOWP into an integrated optical circuit other than just a straight channel waveguide.

5.2 Conclusion and Future Work

A broadband GOWP with high extinction ratio has been demonstrated using a polymer waveguide coated with GOF using drop-casting method. The polarisation effect of the GOWP has been shown to be a result of the anisotropic complex dielectric function of GOF. The extinction ratio of the GOWP was dependent on the GOF thickness. A maximum extinction ratio of 40 dB has been achieved at a wavelength of 1590 nm with only ~1.3 mm of GOF coating length along the propagation direction.

In addition to the current work, it is interesting to fabricate a TE–pass GOWP as a compliment to the current study. It is possible that the principle applied in metal clad waveguides polariser [24, 25] can also be applied in the case of GOWP. According to these references, a thin buffer layer was added between the polarising element (metal-clad) and the waveguide core. By precise control of the buffer thickness, the operation mode of the polariser can be switched from TM-pass to TE-pass.

References

1. Hutchings, D.C. and B.M. Holmes, *A waveguide polarization toolset design based on mode beating.* IEEE Photon., 2011. **3**(3): p. 450.

2. Kikuchi, K. and S. Tsukamoto, *Evaluation of Sensitivity of the Digital Coherent Receiver.* J. Lightwave Technol., 2008. **26**(13): p. 1817-1822.

3. Ohja, S.M., et al., *Simple method of fabricating polarisation-insensitive and very low crosstalk AWG grating devices.* Electron. Lett., 1998. **34**(1): p. 78-79.

4. Nadler, C.K., et al., *Polarization insensitive, low-loss, low-crosstalk wavelength multiplexer modules.* IEEE J. Sel. Top. Quant, 1999. **5**(5): p. 1407-1412.

5. He, J.J., et al., *Integrated polarization compensator for WDM waveguide demultiplexers.* IEEE Photon. Technol. Lett., 1999. **11**(2): p. 224-226.

6. Morand, A., et al., *Integrated optical waveguide polarizer on glass with a birefringent polymer overlay.* IEEE Photon. Technol. Lett., 1998. **10**(11): p. 1599-1601.

7. Lin, H., J. Ning, and G. Fan, *A waveguide polarizer based on Si-coated Ti:LiNbO3 planar structure.* Chin. Opt. Lett, 2004. **2**(2): p. 89.

8. Dai, D., et al., *Compact broadband polarizer based on shallowly-etched silicon-on-insulator ridge optical waveguides.* Opt. Express, 2010. **18**(26): p. 27404-27415.

9. Feth, J.R. and C.L. Chang, *Metal-clad fiber-optic cutoff polarizer.* Opt. Lett., 1986. **11**(6): p. 386-388.

10. Bao, Q., et al., *Broadband Graphene polarizer.* Nature Photon., 2011. **5**: p. 411.

11. Kim, J.T. and S.-Y. Choi, *Graphene-based plasmonic waveguides for photonic integrated circuits.* Opt. Express, 2011. **19**(24): p. 24557-24562.

12. Kim, J.T. and C.-G. Choi, *Graphene-based polymer waveguide polarizer.* Opt. Express, 2012. **20**(4): p. 3556-3562.

13. Eda, G., et al., *Graphene oxide gate dielectric for Graphene-based monolithic field effect transistors.* Appl. Phys. Lett., 2013. **102**(13): p. 133108.

14. Lim, W.H., et al., *Graphene oxide-based waveguide polariser: From thin film to quasi-bulk.* Optics Express, 2014. **22**(9): p. 11090-11098.

15. Vaupel, M. and U. Stoberl. *Appication note: graphene and Graphene oxide*. Accurion solutions for science; Available from: http://www.nanofilm.de/sales-support/downloads/application-notes/applicationnote_graphene.pdf.

16. Loh, K.P., et al., *Graphene Oxide as a chemically tunable platform for optical applications.* Nat. Chem., 2010. **2**: p. 1015.

17. Peres, N.M.R., T. Stauber, and A.H. Castro Neto, *The infrared conductivity of Graphene.* EuroPhysics Letters, 2008. **84**: p. 38002.

18. Stankovich, S., et al., *Synthesis of Graphene-based nanosheets via chemical reduction of exfoliated Graphite Oxide.* Carbon, 2007. **45**(7): p. 1558-1565.

19. Pantazopoulou, A. *Simulation of Graphene-based Nano-antennas*. Available from: http://www.n3cat.upc.edu/presentations/Anastasia-Simulation_of_graphene-based_nano-antennas.pdf.

20. Carbotte, J.P., V.P. Gusynin, and S.G. Sharapov, *AC Conductivity of Graphene: From Tight-Binding Momel to 2 + 1-Dimensional Quantum Electrodynamics.* International Journal of Modern Physics B, 2007. **21**(27): p. 4611-4658.

21. Hanson, G.W., *Dyadic Green's functions and guided surface waves for a surface conductivity model of Graphene.* J. Appl. Phys., 2008. **103**(6): p. 064302.

22. Hong, J.T., et al., *Terahertz conductivity of reduced Graphene Oxide films.* Opt. Express, 2013. **21**(6): p. 7633-7640.

23. Hanson, G.W., *Quasi-transverse electromagnetic modes supported by a Graphene parallel-plate waveguide.* J. Appl. Phys., 2008. **104**(8): p. 084314.

24. Yamamoto, Y., T. Kamiya, and H. Yanai, *Characteristics of optical guided modes in multilayer metal-clad planar optical guide with low-index dielectric buffer layer.* Quantum Electronics, IEEE Journal of, 1975. **11**(9): p. 729-736.

25. Li, G. and A. Xu, *Analysis of the TE-Pass or TM-Pass Metal-Clad Polarizer With a Resonant Buffer Layer.* Journal of Lightwave Technology, 2008. **26**(10): p. 1234-1241.

CHAPTER 6: GRAPHENE OXIDE BASED OPTICAL HUMIDITY AND WATER SENSOR: MOTIVATION

Many studies of the use of Graphene Oxide (GO) or Graphene Oxide Film (GOF) as sensing element in water sensor, humidity sensor [1-7], and gas sensor [8-13] have been reported. The operating principle of these sensors is to measure the conductivity (or more precisely, the capacitance) of the GO or GOF with or without the presence of the stimulus at DC or low AC frequency (up to few KHz). As Graphene-based materials possess broadband response due to their characteristic bandgap properties, it is interesting to study the optical sensing capability of GOF, specifically in the 1550 nm. The objective is to combine the advantages of GOF with the advantages of fibre optic system for sensing applications. As reported in [1-3, 14-16], GO or GOF based sensors have shown ultra-sensitivity (detection at single molecule level demonstrated by Schedin) and ultrafast (~30 ms response and recovery time demonstrated by Borini) capability. On the other hand, fibre optic sensing has the ability of long distance monitoring in remote area such as underground, under-water piping networks and fibre optic cable networks [17-19]. Hence the fusion of GOF and fibre optic is expected to provide ultrasensitive, real-time, and long distance remote sensing. In this work, the design of GOWP discussed in chapter 5 was adopted as sensor for water and humidity. To facilitate interaction between the GOF and the environment, the GOF coated on the SU-8 optical waveguide was not covered with overcladding. In the presence of water or water molecules, the conductivity of the GOF is expected to change and the TE-absorption will change correspondingly. This change was then measured as a change in transmitted power of the GOWP. The structure of this chapter begins with the literature review of the anomalous properties of GOF in the presence of water and to the change in humidity, followed by the performance of GOWP as sensing element for these stimulus.

6.1 Anomalous Unimpeded Water Permeation Through Graphene Oxide Membrane

A number of terms are used to describe Graphene Oxide film with micrometre thickness, most notably Graphene Oxide membrane and Graphene Oxide Paper (GOP). They showed similar chemical, physical and optical characteristics with the difference being the manner that they are formed. GO membrane is coated on a flexi membrane. On the other hand, GOP is a free standing paper-like GO film. As Graphene Oxide films used in this work were coated onto a surface, the term Graphene Oxide film (GOF) will be used.

In 2012, Nair et al. demonstrated the peculiar characteristic of the GO membrane with strong filtration of even the smallest gas atoms/molecule such as helium and hydrogen but exceptionally high permeation of water vapour [20]. The permeation rate of water vapour through a 10 μm thick GO membrane is equal to an open aperture (without GO membrane) at 100% RH but dropped exponentially as the relative humidity reduces. For very thin GO membrane that has only about ten GO layers or in very humid condition, liquids such as IPA, ethanol, and methanol can permeate through the GO membrane. However, thick GO membrane or GOP in dry condition is impermeable for both liquid and gas molecules other than water, including alcohol. Nair et al. explained that this anomalous water permeation in GO membrane is related to the GO structure.

GO membrane consists of thousands of layers of orderly stacked GO sheets. The GO sheets or flakes would typically have a size of several nanometres. In between two pristine-Graphene sheets, there are pristine and oxidized regions as shown in Figure 6.1. The ‘Oxidized’ regions play a role of absorbing water through strong hydrogen bondings [21]. This absorbed water molecules act as spacers that keep neighbouring Graphene

planes between 7 to 10 Å apart, depending on the amount of water absorbed ("dry" GO membrane has a spacing of 6 Å). With this spacing between two GO sheets, other unbounded water molecules can form a 2-Dimensional network between hydrophobic pristine-Graphene sheets. These monolayer water molecules are expected to have high mobility similar to water formed in small-diameter carbon nanotubes. As a result, in a GO membrane saturated with water, water molecules are able to slide between two GO sheets and eventually permeate through the entire thickness of the GO membrane. It is worth noting that the permeation rate of water molecules between two GO sheets is different in different areas of the GO membrane. Due to hydrogen bonding and a narrower space available for diffusion, water is expected to be less mobile within the oxidized regions that are randomly covered with epoxide, hydroxyl, etc. In the absence of water molecules in the GO membrane, the nanocapillaries become narrow in both oxidized and pristine regions. This narrowing of pristine-Graphene nanocapillaries results in the blocking of water transport as well as all other molecules including Helium gas [20]. Later, Danil [22] and Wei [23] both performed simulation of water transport in GO. Although there are some slight contradictions between their results, they generally support Nair's initial model. The additional hypothesis made in their model is that the water molecules are sliding between two GO sheets in ice-like structure. Water in liquid phase is aggregated in cluster form, but becomes crystalline when it solidify into ice [24]. The term ice-like structure refers to the periodic arrangement of water molecules when sliding between two Graphene sheets, similar to a 2D ice sheet sliding between the GO sheets. According to their models, the arrangement of water molecules is slightly different for mono or bi-layers water transport as well as sliding direction as shown in Figure 6.2. The bonding between the water-water molecules are mainly hydrogen bond, but bonding between Graphene-water molecules is due to van der Walls interaction. This means that when water molecules enter the GO membrane, some of the hydrogen bonds will be

broken and bond with the smooth carbon atom surface via van der Walls interaction. As a results, water is able to slip in between two layers of GO sheets and it is expected that the slip length decreases as the solvents become more hydrophobic (non-polar solvent) [25, 26]. In additional, Wei pointed out that the oxygen-containing groups tend to cluster in GO and form patches of pristine and oxidized regions. Naturally, oxidized regions will most likely form at the edges of individual GO flakes and hence there exist a side-pining effect (due to hydrogen bonds) that reduced the enhancement of water permeation. The abnormal water permeation ability in GO membrane has been further explored for its application in salt filtration [27] and water desalination [28].

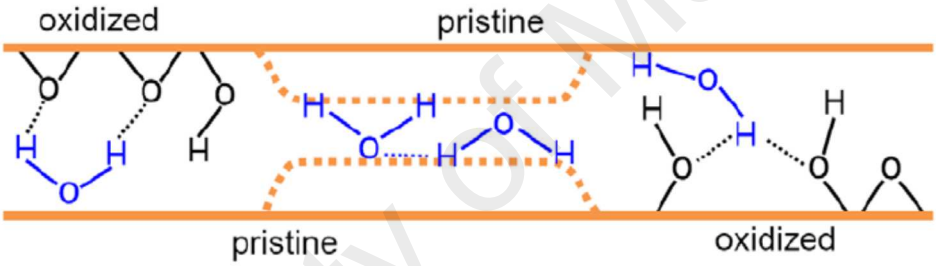

Figure 6.1: Model of two GO sheet.

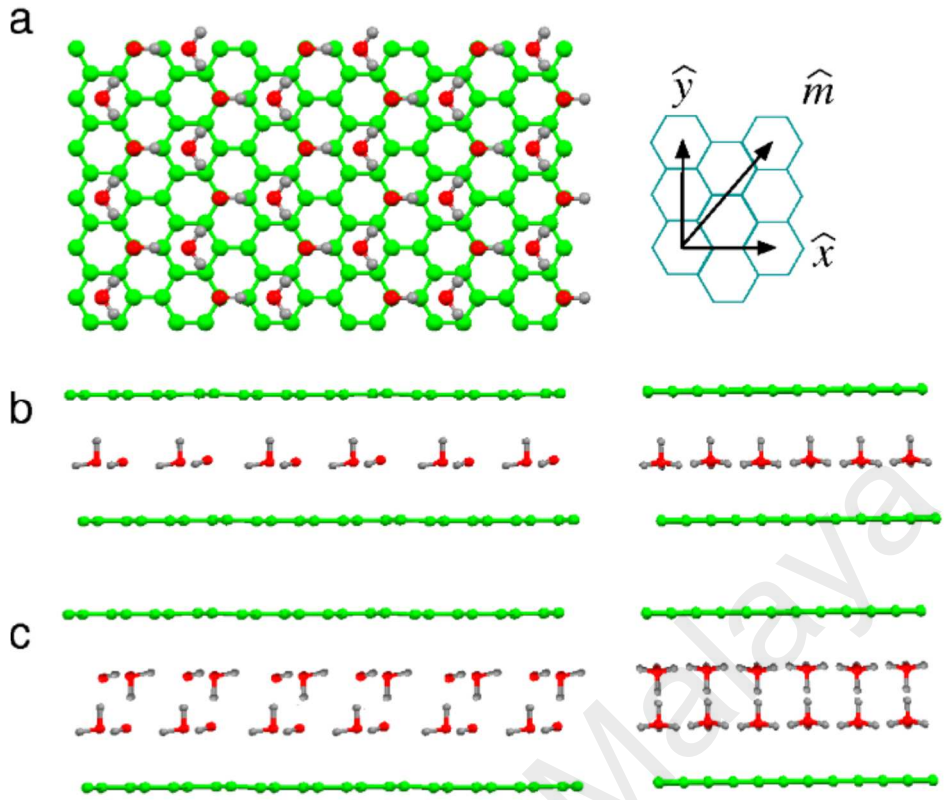

Figure 6.2: Transport mechanism of water molecules between two GO sheets. [22] a) Top view of optimised atomic structure of ice monolayer between the layers of Graphite. Oxygen, hydrogen, and carbon atoms are denoted by red, grey and green colour. The ice layer can slide along x-, y- and m-direction. b, c) Side view of ice mono- and bilayers along y (left) and along x (right) direction.

6.2 Water Dependent Dielectric Properties of Graphene Oxide

In the above section, fast water permeation in GOF was discussed. Incidentally, the presence of water molecules will alter the dielectric properties of GOF. FTIR studies showed that there exist a physical hydrogen bond between the physisorbed water molecules [21]. Absorption of water molecules by the Graphene or GO layers will break the lattice symmetry. As the Graphene band structure is sensitive to lattice symmetry, an opening of bandgap may result [29]. Water molecules absorbed by GO may act as electron acceptor that will eventually cause hole doping in GO [30]. A larger bandgap in GO means the dielectric strength of GO is enhanced, resulting in an increase in resistivity. The increase in resistivity (in DC or low AC regime) of the GOF in the presence of water

molecules was reported in [3, 5, 29]. As a result the amount of water molecules absorbed by GOF has significant impact on its dielectric properties by altering it resistivity. In optical frequencies, higher resistivity translates into lower optical absorption, and hence allows a larger fraction of light to pass through the GOF.

6.3 Graphene Oxide Based Optical Water Sensor: Motivation

Underground or under-water pipe network [31, 32] and fibre optic cable network [33] is one of the largest infrastructure assets of industrial society nowadays. Installed in the 1980s or earlier, these high cost infrastructures are now suffering from aging effects that leads to water leaks. Real time monitoring allows immediate repair to be undertaken to prevent further damage that may lead to disaster. Due to the capability of long distance remote monitoring of fibre optic, various optical fibre-based water sensors have been developed. The sensing technique used include micro-strain [17, 18] and side-polished fibre [19]. The first technique is based on swelling of a suitable optical fibre coating material in the presence of water to induce micro-strain. However, the low water permeability of the "swelling material" results in slow response to the presence of water and it is also difficult for this material to restore back to its initial state [33]. On the other hand, although the side-polished fibre allow immediate response due to changes in boundary condition of the exposed waveguide core, adhesion of other pollutants in the exposed region will result in a change of the response characteristics which is usually irreversible. Although protective layer can be applied on the exposed region, but this will reduce the sensitivity as well as causes delay in sensing due to low water permeation.

As GOF allows fast water permeation and the change in amount of water content in the GOF will alter its optical properties, it was expected that the presence of water will

change the transmission characteristics of a GO-coated optical waveguide. As discussed in chapter 5, GOF exhibits strong anisotropic complex dielectric function. As a result, a GO-coated waveguide polarizer (GOWP) which induces high loss for TE-mode propagation while maintaining high TM-mode transmission was demonstrated [34, 35]. It was found that in the presence of water, this polarization selective capability of GOF was suppressed, and the proposed sensor will encounter an increase in optical power transmission. These behaviours of GOF formed the operating principle for the proposed water detection sensor.

6.3.1 Water Sensor Design and Experimental Setup

The schematic diagram of the experimental setup is shown in Figure 6.3. The waveguide design was slightly different from GOWP, where the GO-coated region of the optical waveguide was exposed to the surroundings. CR-39 was replaced by BCB on silicon substrate. The use of silicon as substrate material allowed the use of "cleaved and break" technique to produce optical quality edge sufficient for low loss fibre coupling after patterning of optical waveguide structures. Else, the use of CR-39 as substrate material will require dicing and polishing processes to prepare the samples for optical characterization, which will introduce pollutants from the resulting debris and coolant used onto the exposed waveguide and corresponding high insertion loss. The BCB undercladding layer had a thickness of 6.1 μm with a refractive index of 1.5538 measured at 1550 nm - using Sairon Technology SPA-4000 prism coupler. The samples were prepared into chips about 1 cm in length and their input and output were permanently bonded to SMF-28 fibres. 2 drops of 0.5 μl GO solutions with concentration of 4 μg/μl were then applied onto the polymer waveguides via drop-casting method. The samples were then allowed to dry in ambient condition for several hours. The average thickness

of the GOF was measured to be about 0.75 μm using Dektak D150 surface profiler. The GOF thickness value was selected based on mode field distribution simulation using Comsol that ensure high TE-mode absorption. For comparison, samples with GOF thickness of about 0.3 μm were fabricated and showed similar response but with much lower TE-mode absorption which agreed well with the simulation results. It is worth noting that the adhesion of GOF on the sample surface was very strong where it can only be removed by strong physical scratching. The polymer waveguide area that was not coated with GOF was coated with NOA-65 UV-sensitive resin to ensure that only the GOF region was exposed to the stimulus such as water.

The optical polarization state supported by the waveguide sensor was measured using a polarimeter (Thorlabs PAX 5710). It was found that the transmission of TE-polarized light is suppressed by the waveguide sensor by more than 30 dB with reference to TM-polarized light. Suppression of TE-mode is due to absorption of the electric field parallel to the GO layers in the GOF as discussed in the previous chapter. Throughout the optical measurement, the polarization of the incident light was set to be a TE-polarized using a Polarization Controller (PC). Extra care in the handling of the launch fibre was taken to ensure that the linear polarization state of the incident light was not scrambled by minor disturbance to the fibre. To simulate the presence of water, 1 μl of water droplet was applied onto the GOF using a micro-pipette and the change in transmission power of the sensor was recorded at 0.5 second intervals and the results was analysed. Visual observation of the GOF was done using a long working distance microscope (Nikon SMZ 1000).

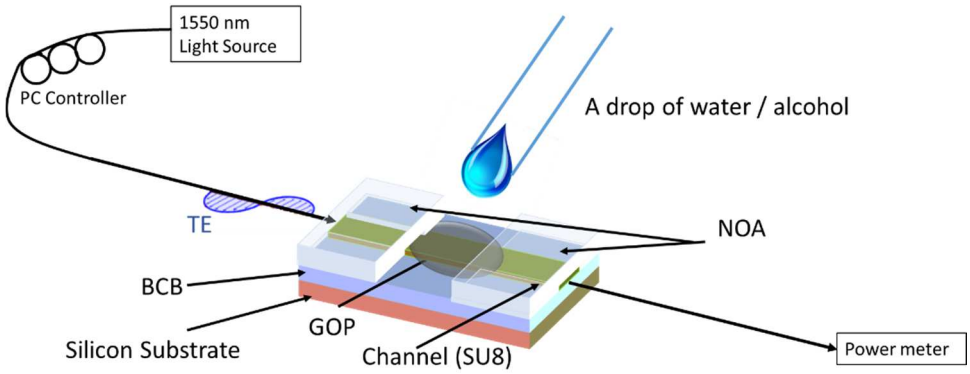

Figure 6.3: Schematic diagram of GO-coated waveguide sensor and the experiment setup for water detection.

6.3.2 Performance of Proposed Water Sensors

The response of the proposed sensor when a 1 µl water droplet was applied onto the GOF is shown in Figure 6.4. When water was applied, the transmitted power of the sensor increased by 32 dB instantaneously, approaching its TM-polarized light power level. As the water droplet evaporated, the transmitted power reduced to its initial value before the application of water droplet at the ~12th minute. The increase of transmission power when water droplet was applied is due to the change in the GOF optical properties where the GOF no longer absorbs the TE-polarized light power. This phenomenon was verified by observing the polarization state of the transmitted light using the polarimeter. When the incident light was set to TE-mode using the PC, the polarimeter measured a low optical power with TM-polarized state. This is the small amount of the TM-polarized light not filtered by the PC due to its performance limitation. However, when water droplet was applied onto the GOF, the transmitted power increased and the polarization state measured from the polarimeter was strongly TE-polarized. Rotating the PC will only rotate the polarization state of the transmitted light with no significant variation in the transmission power as long as the water droplet was still covering the GOF.

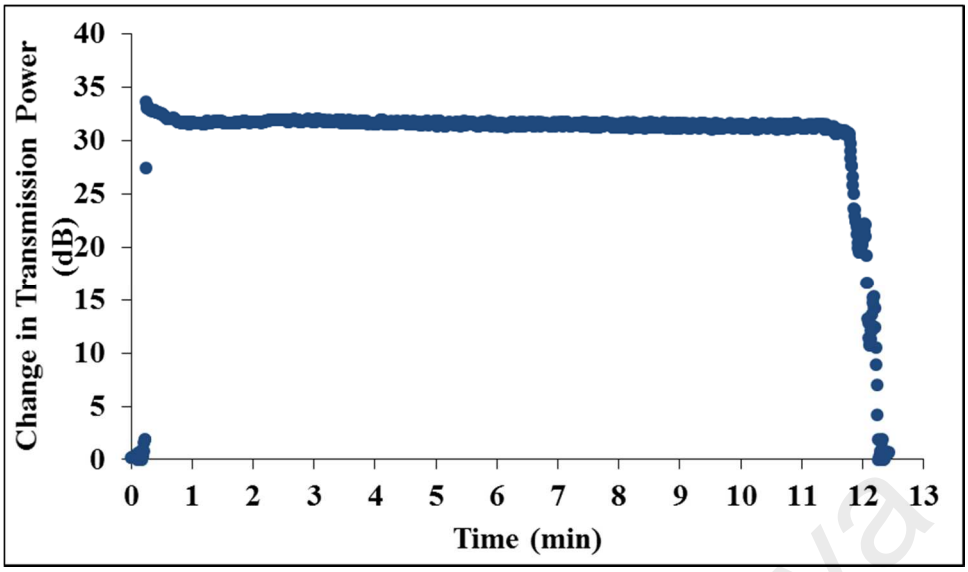

Figure 6.4: The response (change in transmission power) of the proposed sensor to a drop of water.

The suppression of TE-mode absorption by the GOF in the presence of water is still being studied. The possibility of the GOF being detached from the sample surface, particularly the top of the core waveguides, after the water droplet was applied was considered. The consistent lower power level after every test cycles also alleviated this possibility. Scrambling of the polarization state of light by the dipole moment of water within the GOF was also considered. However, this contradicts with the ice-like model discussed earlier and the polarization state of the waveguide output measured using polarimeter did not show random polarization – polarization state of the output was changed only when the PC was used to rotate the polarization state of the incident light. Hence, the most probable contributing factor is believed to be the change in dielectric properties of the GOF in the presence of water. Water permeated into the GOF will interact with the oxygen functional groups of individual GO layers [4, 21, 23]. This interaction will increase the GO layers bandgap and decrease its conductivity [3, 5, 29]. Henceforth, the propagation loss of the TE-polarized light in the GOF is reduced, resulting in the increase of the transmission of the TE-polarized light.

The significant change in transmission power (32 dB) of the waveguide sensor when only 1 μl of water droplet was applied on the GOF indicated that the sensor was sensitive to even smaller volume of water. To achieve a smaller fraction of water content with the same droplet volume, water-alcohol solution with different mixture ratio were used and the change in transmitted power over time were measured. The alcohol used was Iso-Proponol (IPA). Selected mixture ratio of water-alcohol solution (above 30 vol. %) is plotted in Figure 6.5. When water-alcohol mixture solutions with water content of more than 30 volume % (vol. %) were applied on the GOF, the transmitted power remained low initially before increasing to the maximum achievable transmitted power (when pure water was applied). This was then followed by a decrease in transmitted power to its initial value when the mixture solution dried off the GOF. We believed the initially insignificant response from the sensor can be explained by the filtration characteristic of GOF where larger alcohol molecules were not able to permeate into the GOF. In addition, the amount of "free" water molecules in a water-alcohol mixture solution was smaller than the total water content because water tends to form ice-like structures around alcohol molecules [36-38]. Upon drying, IPA evaporates faster than water due to its higher partial pressure compared to water [39, 40]. As a result, increasing amount of water molecules were "freed" from the water-alcohol bonding and were able to permeate into the GOF, with the effect eventually became large enough to be measured. The time taken for the transmitted power to decrease to the initial value after the application of mixture solution droplet increased linearly from 47.5 seconds to 714 seconds with increasing water content from 30 vol. % to 100 vol. % respectively, as shown in Figure 6.6. This relationship between water content in a fixed volume of water-alcohol solution and its drying time can be used to measure water content of more than 30 vol. % in a droplet volume of 1 μl.

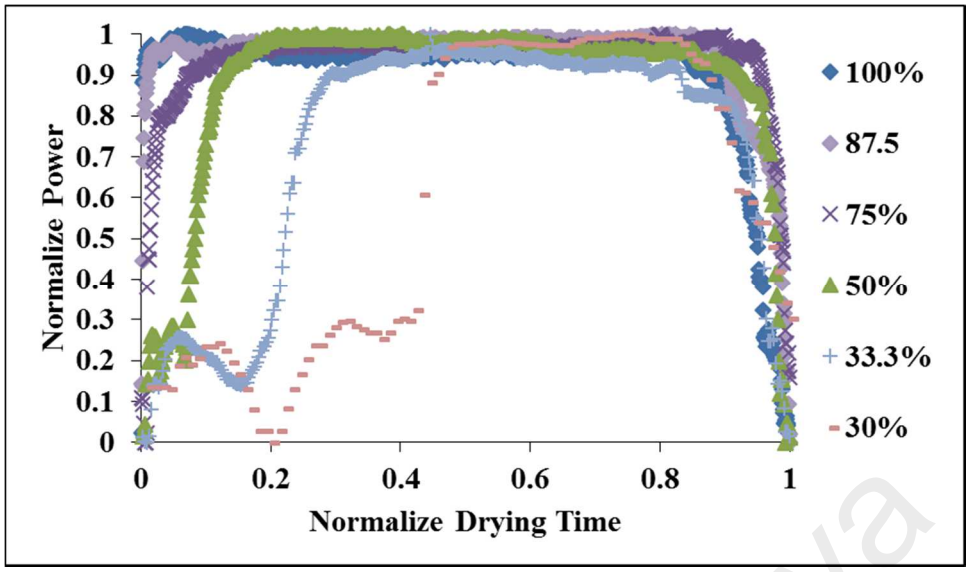

a)

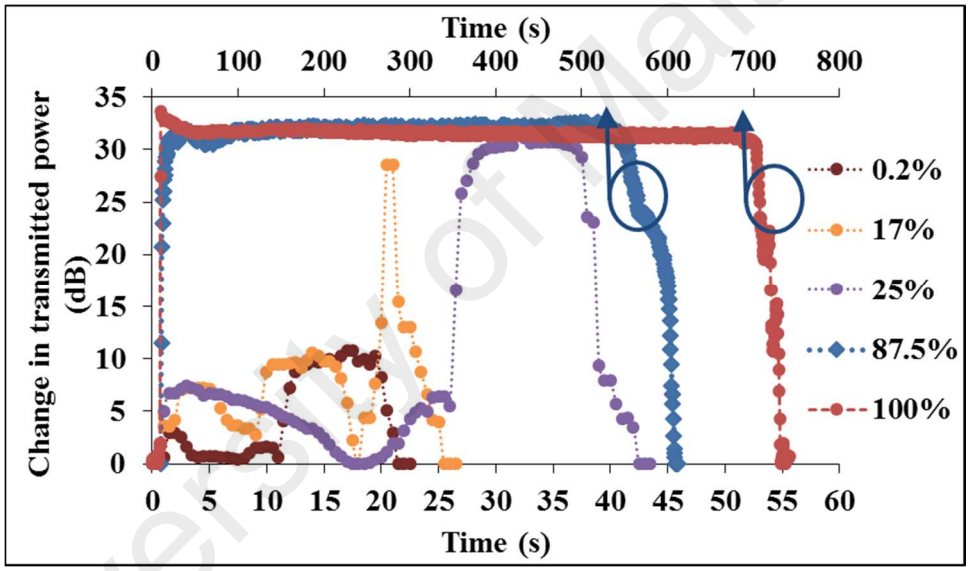

b)

Figure 6.5: Performance of water sensor toward water-alcohol mixture a) above 30% and b) selected mixture.

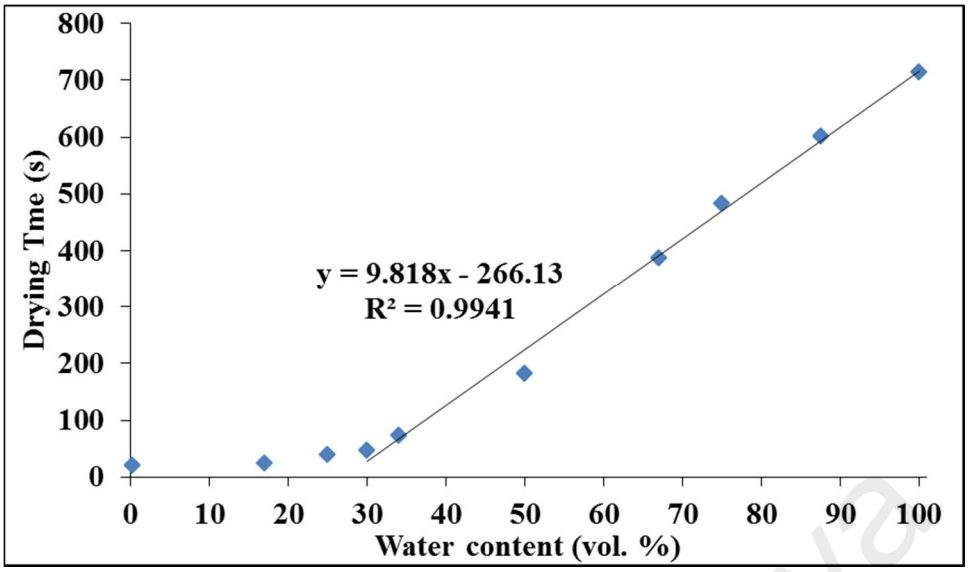

Figure 6.6: The change in drying time measured by the proposed sensor toward various water-alcohol mixture solution with different water content was applied.

This showed that the sensor has very high sensitivity to minute amount of water. The reproducibility of the sensor performance was tested by taking multiple measurements for each droplet solution mixtures over a period of more than one month and was found to be consistent over the test period. The large variation in the change in transmitted power will allow the development of high sensitivity water detection sensor.

6.3.3 Conclusion

An all-optical water detection sensor using GO as functional element was demonstrated. The sensor made use of the unique characteristics of GOF – the variable TE-polarized light transmission loss in the presence of water and its highly selective water permeability. When a water droplet was applied onto the GOF, water molecules permeate easily into the GO layers and reduce the TE-polarized light absorption, which leads to a significant increase in the transmitted optical power. A reduction in the transmission loss of more than 30 dB was obtained when a water droplet of 1 μL in volume was applied onto the GO-coated waveguide and the response was instantaneous. The strong adhesive

property and highly selective filtering characteristics of GOF allows it to act as a good protective layer to prevent contaminations of the waveguide core from physical pollutants while maintaining its fast response characteristic. The sensor can be used for long distance remote water detection.

6.4 Graphene Oxide Based Optical Humidity Sensor: Motivation

Extra demand for fast response and short recovery time other than the basic needs of high sensitivity and wide detection range humidity sensors are necessary to meet industry requirements. Consequently, research on humidity-sensitive nanomaterials such as silicon nanostructures, ceramic nanomaterials, semiconductor nanoparticles and metal oxide nanowire have attracted much attention due to its high surface to volume ratio [1, 14]. Lately, monolayer or few layers Graphene followed by Graphene Oxide (GO) have received increasing attention due to their inherent electrical and mechanical properties, holding great potential for ultrasensitive sensor application [1, 2]. Schedin demonstrated that Graphene has single molecule detection sensitivity due to its low thermal noise properties [15]. On the other hand, GO has many oxygen functional groups bonded in its two-dimensional network of sp^2 and sp^3 hybridized carbon atoms arranged in a honeycomb structure. These functional groups include hydroxyl, epoxy and carboxylic acid [1, 2]. The sp^3 hybridized carbon atoms turn GO into an insulator by decreasing its conductivity, and enhances its hydrophilic properties [2, 3, 16]. Besides, oxygen functional groups in GO also allow fast water permeation within the GO layers as reported by Nair [20], which enables fast water molecules diffusion (in and out) of GO during humidity change. The motivation of this work is similar to section 6.3 above, where we further explored the use of GOF to detect humidity in optical frequency.

6.4.1 Humidity Sensor Design and Experimental Setup

The GO based optical humidity sensors shared the same design as water detection sensor discussed in the previous section. Likewise with the experimental setup. A gas tube providing controlled humidity vapour was placed about 1 cm above the GO-coating on the waveguide (sensing region) as shown in Figure 6.8. Humid nitrogen gas was produced by bubbling pure nitrogen gas through water before flowing out from the gas tube. The response time of the sensor to humid air (~90% RH) was measured using a photodiode and a mechanical shutter was placed between the vapour source and the sensing region to control the exposure intervals. Measurement of the change in transmitted power to different relative humidity was carried out by placing the proposed sensor in a humidity control box as shown in Figure 6.8. Relative humidity in the box was controlled by mixing pure nitrogen gas and humid nitrogen gas with different flow rates before flowing into the box. Before each optical measurement, relative humidity of the gas flow or inside the humidity control box was measured using a hygrometer from Hanna Instruments, HI 8562. A long working distance optical microscope (Nikon SMZ1000) was used to monitor the sensing region during the experiment. The optical measurement setup was similar to section 6.3.1, the polarization of the incident light was set to be TE-polarized using a PC.

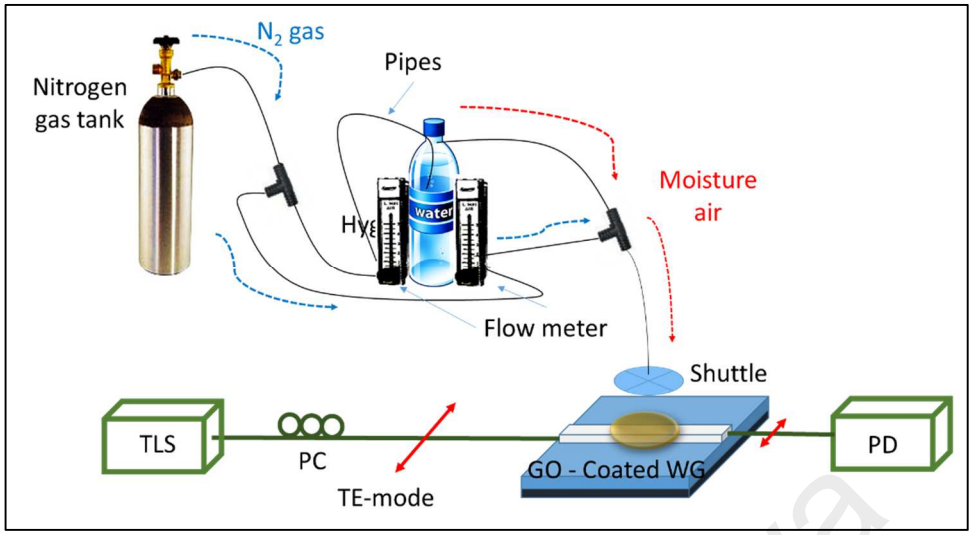

Figure 6.7: Schematic diagram of the proposed humidity sensor for fast response measurement.

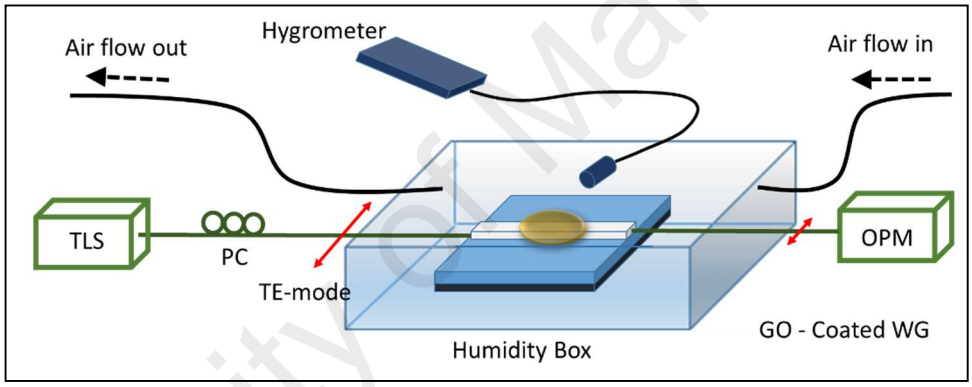

Figure 6.8: Schematic diagram of the proposed humidity sensor for humidity measurement.

6.4.2 Performance of Optical Humidity Sensors

Figure 6.9a shows the response of the sensor in ambient condition (~50% RH) to a breeze of humid nitrogen gas (100% RH) over time. The breeze was introduced directly onto the sensing region of the sensor, and sustained from the 6th to 9th second. The transmitted power increased instantaneously to its maximum (equivalent to the transmitted power of TM-polarized light). It remained at maximum for 6 seconds before returning to its initial minimum transmitted power level, starting at the 13th second till the 14th second. Optical micrographs of the sensing region at different stages in Figure 6.9a are shown in Figure 6.9b to Figure 6.9g. Prior to the introduction of humid air (up to the

6th second), no water condensation was observed on both the GOF and the substrate, as shown in Figure 6.9b. When humid air was first introduced at approximately the 6th second, corresponding to the increase in transmitted power, small water droplets were formed on the substrate surface and a change in the GOF brightness contrast was observed (Figure 6.9c). This indicated fast water permeation into the GOF, which reduced the propagation loss of TE-polarised light induced by the GOF. Sustained humid air flow onto the sensor for a further 3 seconds created larger water droplets on the substrate surface (Figure 6.9d). A layer of water was also observable on the GOF but this did not affect the transmitted power. When the humid air flow was stopped, two drying stages were observed. The first drying stage involves the drying of water moisture droplets on the substrate and GOF surface (Figure 6.9e – 9th – 13th second). At this stage, water in the GOF still remained, indicated by the difference in brightness contrast of the GOF between Figure 6.9b and Figure 6.9e and the constant transmitted power of the proposed sensor. The second drying stage (13th to 14st second) involved the drying or reduction of water content in the GOF from the edge towards the centre of the film, observed as the restoration of brightness contrast from the edge towards the centre of the GOF (Figure 6.9f and Figure 6.9g). This corresponded to the decrease of transmitted power to its initial value, and the GOF looked similar to Figure 6.9b after the 14th second. These observations showed that humid air can easily permeate into the GOF and results in a change of the transmitted power of the sensor. The experiment was repeated 5 times and the sensor showed a similar response.

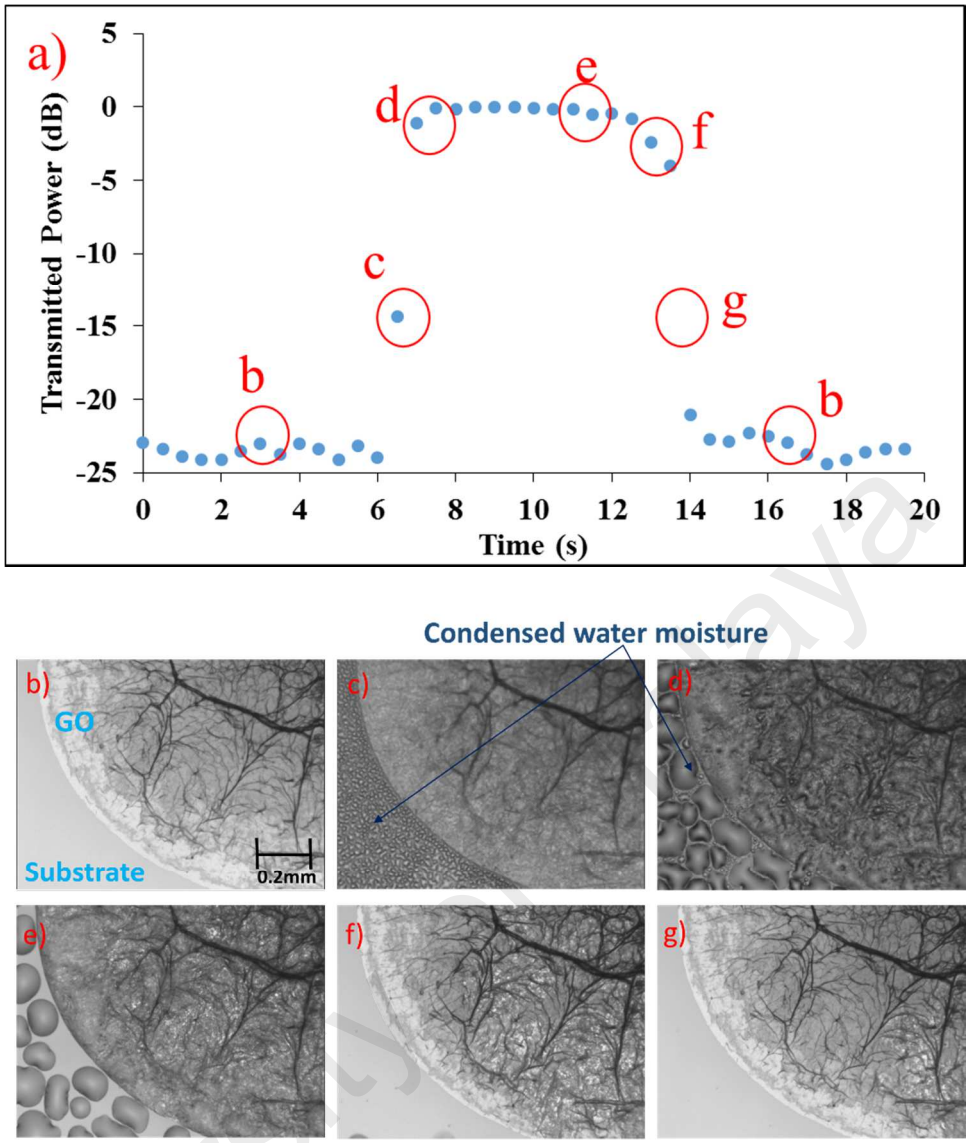

Figure 6.9: a) Change in transmitted power over time when humid air was introduced onto the GOF, from the 6th second to 9th second, and corresponding optical micrographs of the GOF at the marked times: b) before humid air was introduced; c) the beginning of the flow of humid air at the 6th second; d) the end of the humid air flow; e) first drying stage of the GOF with water droplets on substrate; f) second drying stage, where water droplets on substrate and GOF has evaporated; and g) final stage of drying where water content in the GOF recedes rapidly from the edge to the centre.

To study the response time of the sensor, the output of the sensor was connected to a photodiode and the transmitted power was observed using an oscilloscope, and the results are shown in Figure 6.10. Humid air flow onto the sensing region was controlled using a mechanical shutter with flow intervals of 5 seconds and a flow time of 1 second. The sensor exhibited a fast response to the presence and absence of humid air flow as shown in Figure 6.10a. The gradual increase in maximum transmitted power for subsequent breeze of humid air flow indicated that the GOF was not saturated with water during the first few breezes of humid air flow. When the flow interval was reduced to ~0.67 seconds, the proposed sensor was still able to provide a distinction between the presence and absence of humid air flow, as shown in Figure 6.10b. Shorter flow intervals will result in the saturation of the GOF with water and the transmitted power of the sensor will eventually remain at the maximum after a few flow intervals. This is also verified by the visual inspection of the GOF using microscope.

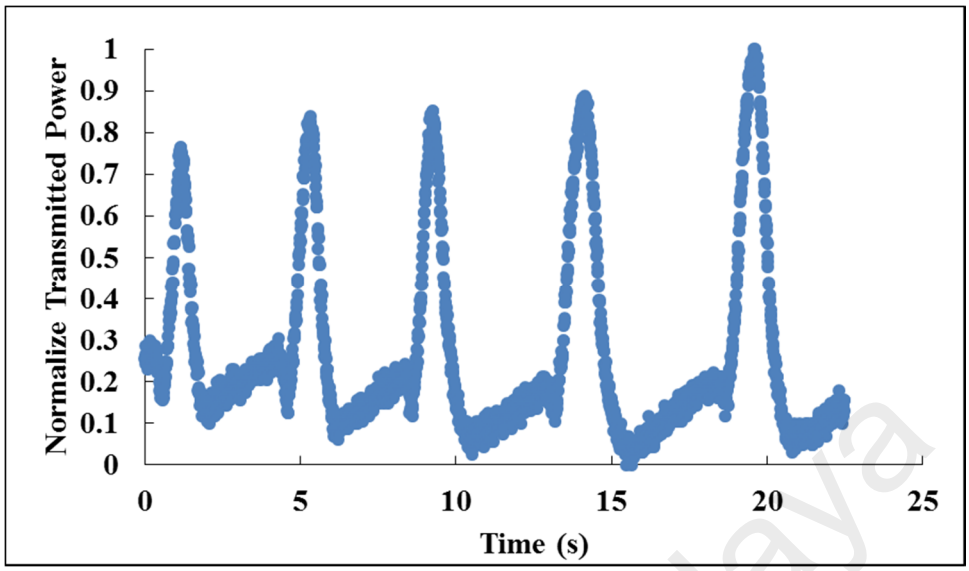

a)

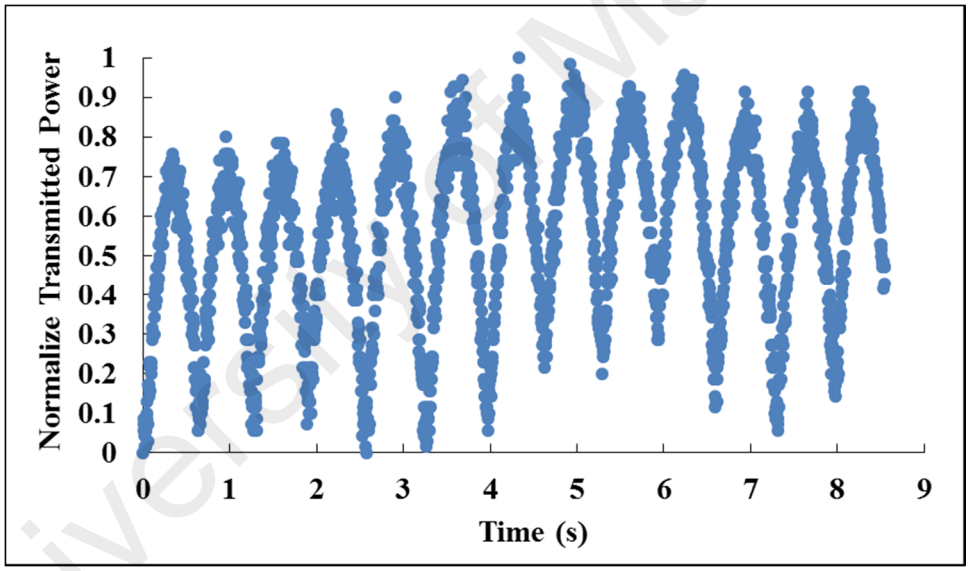

b)

Figure 6.10: Changes in the normalized transmitted power when humid air (100% RH) was introduced onto the proposed sensor periodically at a) 5.0 seconds intervals and b) 0.67 seconds intervals.

Figure 6.11 shows the transmitted power of the proposed sensor at different humidity levels. Basically, 2 characteristics were observed. For humidity level below 60% RH, the transmitted power of the sensor remained low and did not show any changes while a linear response was observed for humidity level between 60 to 100% RH with the transmitted power increased linearly from -42 dBm to 19 dBm respectively. Due to range limitation of the calibration hygrometer, relative humidity from 95% to 99% RH was not measured, while 100% RH was determined by the observation of water condensation on the surface of the sensing region. The response of the proposed sensor was calculated from the gradient of Figure 6.11 to be 0.553 dB/% RH in the humidity range between 60 to 100% RH.

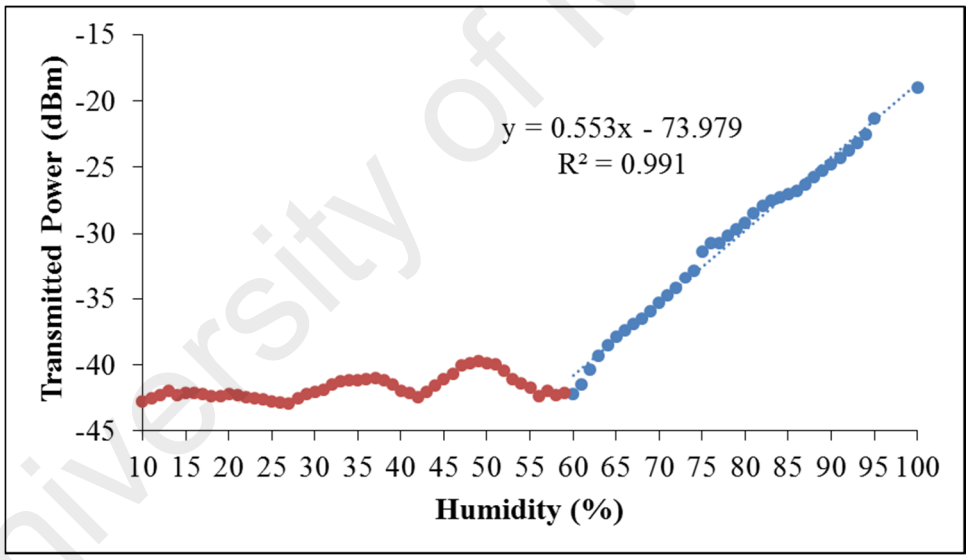

Figure 6.11: Linear response to humidity in the range of 60% RH to 100% RH.

The polarization state of the transmitted light was measured when the sensor was exposed to a relative humidity of 100% RH and was TE-polarized, which was the same observation when water was directly applied onto the sensing region. The water saturated GOF seems to lose its polarization capability and became transparent to both TE- and TM-polarized light. There are reports showing that, at high relative humidity, water

molecules can easily permeate in and out of the GOF of up to 10 μm in thickness [20]. The permeated water molecules readily interact with the functional groups of the individual GO layer eventually change the dielectric properties of the GOF due to changes in energy bandgap, which was discussed earlier. Therefore, the propagation loss of the TE-polarized light in the GOF was reduced, resulting in the increase of the transmission of TE-polarized light. When the relative humidity surrounding the sensor was increased, the amount of water permeated into the GOF will increase in order to achieve equilibrium with the surrounding air. The result was the increase in transmitted power of the sensor with the increase of relative humidity. Below 60% RH (plotted as brown coloured points in Figure 6.11) the sensor showed a flat response, which indicates that water permeation into the GOF was not significant for relative humidity below 60% RH. This phenomenon is consistent with [20], where the increase of water permeation rate through GOF with increasing relative humidity only becomes significant at high relative humidity.

6.4.3 Aging in Graphene Oxide

When the reproducibility of the sensor was tested, an aging effect on its sensitivity to relative humidity was observed. Initially, the sensor began to response to relative humidity above 60% RH. However, the sensitivity decreased over time and the sensor only responded to higher relative humidity as shown in Figure 6.12. It was believed that the aging effect involved the reduction of the GOF hydrophilic characteristic and higher humidity level was required to initiate water permeation into the GOF and trigger the optical response.

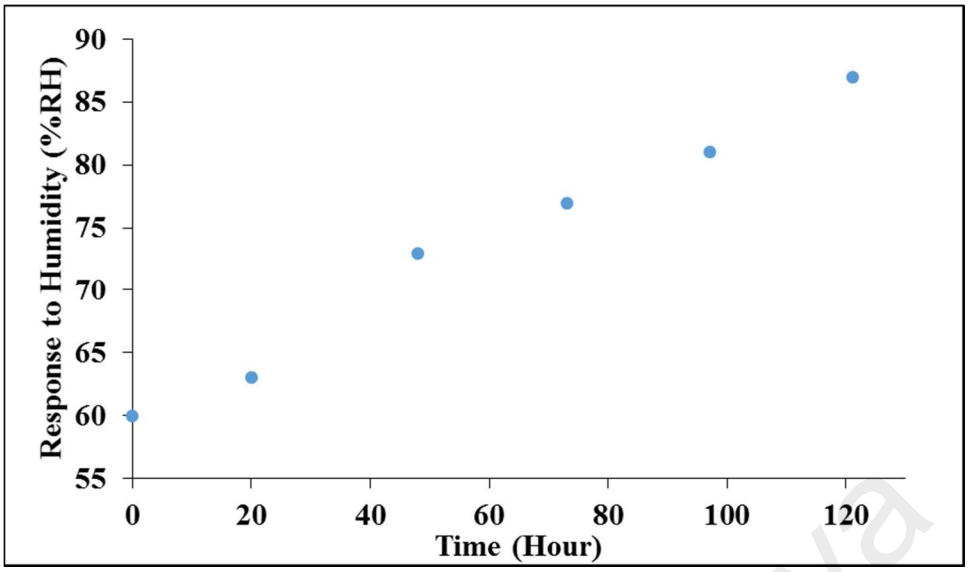

Figure 6.12: The aging effect of the proposed sensor.

To further investigate the reason behind this aging effect, multiple GOF with similar thickness were drop-casted on to a transparency sheet at different time. FTIR measurement was then carried out on the drop-casted films and the result is shown in Figure 6.13. The chemical bonding represented by each peak in the FTIR spectrum was discussed in section 4.1.3.4. Two interesting characteristic peaks were observed. Firstly, the broad peak between 3000 cm^{-1} to 3700 cm^{-1} was weakened over time. This peak corresponds to the stretching of hydroxyl in the presence of water, indicating a loss of hydroxyls and intercalated water between the GO layers. Secondly, the peak intensity of Carbonyls, C = O (highlighted in red box) was found to be deprived over time, which meant that the C = O that exist in the GO was being reduced to hydroxyl groups. Kim [41] stated that this is due to the natural meta-stability of multilayer GOF at room temperature. This structure deprivation of epoxide groups is driven by the availability of H^+ species in the GOF. In a freshly drop-casted GOF, the excess H^+ species were initially rich in epoxide and follow by hydroxyl groups to form water molecules which than evaporate out from the GOF. To quantify the significant loss of C = O bonds, the ratio of peak intensity between 1735 cm^{-1} to 1650cm^{-1} was plotted as shown in Figure 6.14. This ratio plot shows that the characteristic relaxation time of structure deprived of epoxide

groups was about 40 hour. It is worth nothing that the relaxation time of the GOF used in the current work was much faster compared to Kim which is about one month. This differences may be due to the difference in GO preparation process (different in Hummer's method), and drying conditions of GOF (which was dependent on the substrate material used and ambient environment conditions during drop-casting).

The reduction of epoxide groups in GO can be related indirectly to its hydrophilic properties using observations in [42]. You et al. compared the properties GOF produced by GO solution synthesised using both Hummer's and Brodie methods. Both GOFs reacted differently with water with different degree of hydrophilicity, corresponding to different interlayer spacing when they were completely immersed in water. When both GOFs were measured using FTIR, C = O bonding can only be found in GOF produced by GO solution synthesised using Hummer's method, which caused the GOF to have a higher degree of hydration/solvation. Moreover, C-OH was less abundant in Hummer's GOF compared to Brodie GOF, as Brodie GOF exhibited better ordering and thus better crystallinity. Hummer's GOF has the capability to undergo osmotic swelling – insertion of more than one water monolayer at the same time; while Brodie GOF will undergo crystalline swelling - insertion of water by distinct monolayer steps. As a conclusion, You et al. pointed out that Hummer's GOF has better hydrophilic properties than Brodie GOF due to the existent of C = O. In the present work, the C = O bonding was reduced due to meta-stability phenomenon, hence the GO hydrophilic properties was expected to decrease and eventually lead to the aging effect in the humidity sensor. It is worth noting that the hydrophilic properties mentioned here refers to the ability of GOF to attract and absorbed water molecules from humid air. Hence, the performance of the GO based water sensor discussed in section 6.3.2, where liquid phase water molecules are directly applied on to the GOF, was not affected by the same aging effect.

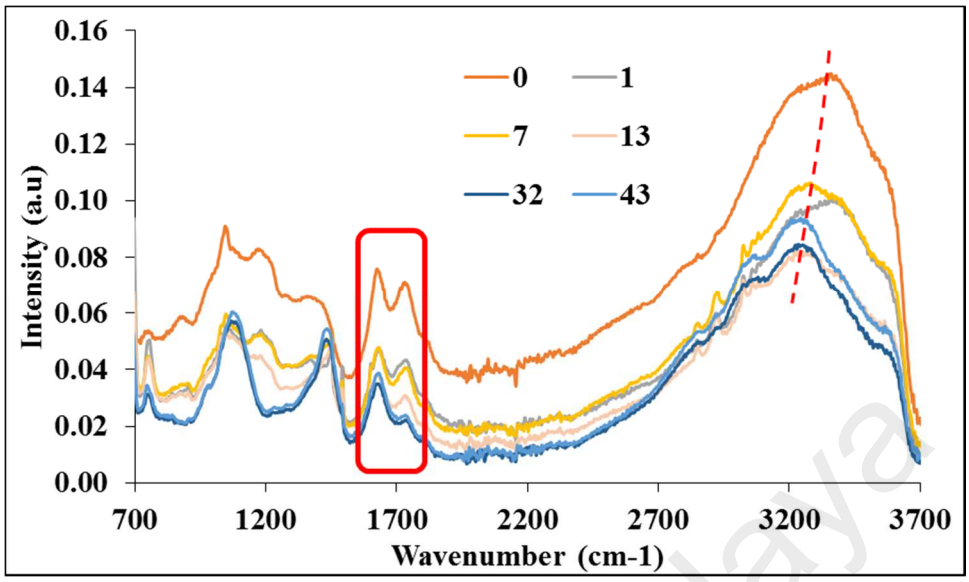

Figure 6.13: FTIR characterization of GOF at different time (hour).

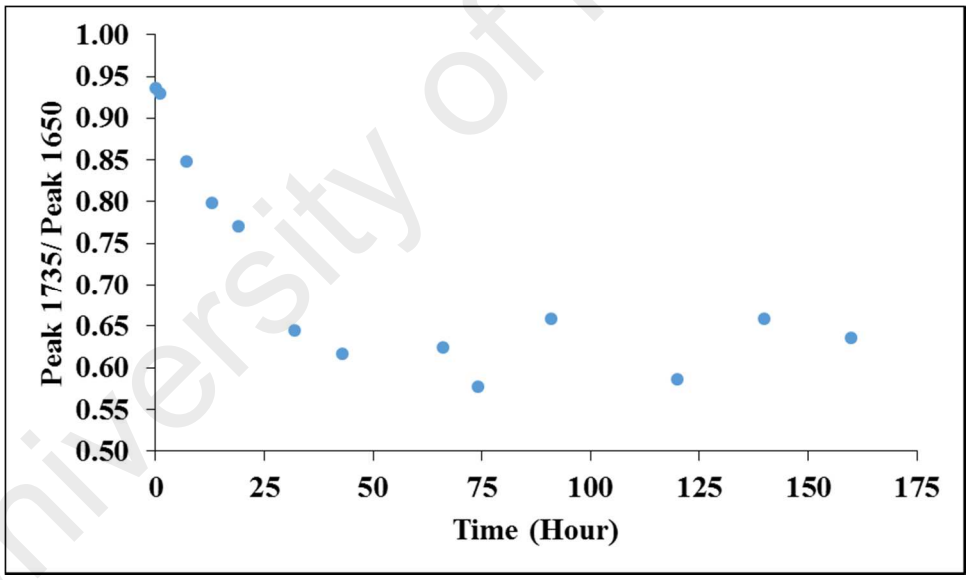

Figure 6.14: FTIR ratio of peak intensity 1735 to 1650 of GOF at various time.

6.4.4 Conclusion

The humidity sensing ability of a GO-coated optical waveguide has been studied. Optical transmission characteristic of the proposed sensor is found to be affected by the relative humidity of its surrounding. The increase in transmitted power at higher humidity is due to a change in the dielectric properties of the GOF where the conductivity of the GOF is reduced in the presence of water molecules. The proposed sensor exhibits fast response of less than 1 second to humid air breezes. In addition, it shows a good linear response of 0.553 dB/% RH in the humidity range from 60% to 100% RH. However, the sensor encounters a fast aging effect. FTIR characterization review that the aging effect is due to the deprivation of C = O in GOF which has significant impact on the GOF hydrophilic properties. We believe this deprivation can be prolonged by optimising the GO preparation method.

References

1. Bi, H., et al., *Ultrahigh humidity sensitivity of Graphene Oxide.* Scientic Reports, 2013. **3**(2714).

2. Yao, Y., et al., *The effect of ambient humidity on the electrical properties of Graphene Oxide films.* Nanoscale Research Letters, 2012. **7**(1): p. 363.

3. Jung, I., et al., *Effect of Water Vapor on Electrical Properties of Individual Reduced Graphene Oxide Sheets.* The Journal of Physical Chemistry C, 2008. **112**(51): p. 20264-20268.

4. Wang, D.-W., et al., *A water-dielectric capacitor using hydrated Graphene Oxide film.* Journal of Materials Chemistry, 2012. **22**(39): p. 21085-21091.

5. Lipatov, A., et al., *Highly selective gas sensor arrays based on thermally reduced Graphene Oxide.* Nanoscale, 2013. **5**(12): p. 5426-5434.

6. Cheng-Long, Z., Q. Ming, and H. Qing-An. *Humidity sensing properties of the sensor based on Graphene Oxide films with different dispersion concentrations*. in *Sensors, 2011 IEEE*. 2011.

7. Zhang, D., J. Tong, and B. Xia, *Humidity-sensing properties of chemically reduced Graphene Oxide/polymer nanocomposite film sensor based on layer-by-layer nano self-assembly.* Sensors and Actuators B: Chemical, 2014. **197**(0): p. 66-72.

8. He, Q., et al., *Graphene-based electronic sensors.* Chemical Science, 2012. **3**(6): p. 1764-1772.

9. Robinson, J.T., et al., *Reduced Graphene Oxide Molecular Sensors.* Nano Letters, 2008. **8**(10): p. 3137-3140.

10. Basu, S. and P. Bhattacharyya, *Recent developments on Graphene and Graphene Oxide based solid state gas sensors.* Sensors and Actuators B: Chemical, 2012. **173**(0): p. 1-21.

11. Yavari, F. and N. Koratkar, *Graphene-Based Chemical Sensors.* The Journal of Physical Chemistry Letters, 2012. **3**(13): p. 1746-1753.

12. Yang, G., et al., *Flexible Graphene-based chemical sensors on paper substrates.* Physical Chemistry Chemical Physics, 2013. **15**(6): p. 1798-1801.

13. Lu, G., et al., *Toward Practical Gas Sensing with Highly Reduced Graphene Oxide: A New Signal Processing Method To Circumvent Run-to-Run and Device-to-Device Variations.* ACS Nano, 2011. **5**(2): p. 1154-1164.

14. Mogera, U., et al., *Ultrafast response humidity sensor using supramolecular nanofibre and its application in monitoring breath humidity and flow.* Sci. Rep., 2014. **4**(4103).

15. Schedin, F., et al., *Detection of individual gas molecules adsorbed on Graphene.* Nat mater, 2007. **6**(9): p. 652-665.

16. Borini, S., et al., *Ultrafast Graphene Oxide Humidity Sensors.* ACS Nano, 2013. **7**(12): p. 11166-11173.

17. Lu, P., L. Men, and Q. Chen, *Tuning the sensing responses of polymer-coated fiber Bragg gratings.* Journal of Applied Physics, 2008. **104**(11): p. 116110-116110-3.

18. Liyin, H., et al. *FBG moisture sensor system using SOA-based fiber laser with temperature compensation.* in *Communications and Photonics Conference and Exhibition, 2011. ACP. Asia*. 2011.

19. Sohn, K.-R., K.-T. Kim, and J.-W. Song, *Optical fiber sensor for water detection using a side-polished fiber coupler with a planar glass-overlay-waveguide.* Sensors and Actuators A: Physical, 2002. **101**(1–2): p. 137-142.

20. Nair, R.R., et al., *Unimpeded Permeation of Water Through Helium-Leak–Tight Graphene-Based Membranes.* Science, 2012. **335**(6067): p. 442-444.

21. Acik, M., et al., *The Role of Intercalated Water in Multilayered Graphene Oxide.* ACS Nano, 2010. **4**(10): p. 5861-5868.

22. Boukhvalov, D.W., M.I. Katsnelson, and Y.-W. Son, *Origin of Anomalous Water Permeation through Graphene Oxide Membrane.* Nano Letters, 2013. **13**(8): p. 3930-3935.

23. Wei, N., X. Peng, and Z. Xu, *Understanding Water Permeation in Graphene Oxide Membranes.* ACS Applied Materials & Interfaces, 2014.

24. Tokmachev, A.M., A.L. Tchougréeff, and R. Dronskowski, *Hydrogen-Bond Networks in Water Clusters (H2O)20: An Exhaustive Quantum-Chemical Analysis.* ChemPhysChem, 2010. **11**(2): p. 384-388.

25. Majumder, M., et al., *Nanoscale hydrodynamics: Enhanced flow in carbon nanotubes.* Nature, 2005. **438**(7064): p. 44.

26. Hummer, G., J.C. Rasaiah, and J.P. Noworyta, *Water conduction through the hydrophobic channel of a carbon nanotube.* Nature, 2011. **414**(6860): p. 188.

27. Joshi, R.K., et al., *Precise and Ultrafast Molecular Sieving Through Graphene Oxide Membranes.* Science, 2014. **343**(6172): p. 752-754.

28. Huang, H., et al., *Ultrafast viscous water flow through nanostrand-channelled Graphene Oxide membranes.* Nature Communications, 2013. **4**(2979).

29. Yavari, F., et al., *Tunable Bandgap in Graphene by the Controlled Adsorption of Water Molecules.* Small, 2010. **6**(22): p. 2535-2538.

30. Ryu, S., et al., *Atmospheric Oxygen Binding and Hole Doping in Deformed Graphene on a SiO2 Substrate.* Nano Letters, 2010. **10**(12): p. 4944-4951.

31. Morais, D.C. and A.T. de Almeida, *Group decision-making for leakage management strategy of water network.* Resources, Conservation and Recycling, 2007. **52**(2): p. 441-459.

32. Poulakis, Z., D. Valougeorgis, and C. Papadimitriou, *Leakage detection in water pipe networks using a Bayesian probabilistic framework.* Probabilistic Engineering Mechanics, 2003. **18**(4): p. 315-327.

33. Jung, S.-H., et al., *Water sensor using macrobending-sensitive fiber for real-time submersion monitoring.* Optics Communications, 2006. **260**(1): p. 105-108.

34. Eda, G., et al., *Graphene Oxide gate dielectric for Graphene-based monolithic field effect transistors.* Appl. Phys. Lett., 2013. **102**(13): p. 133108.

35. Lim, W.H., et al., *Graphene Oxide-based waveguide polariser: From thin film to quasi-bulk.* Optics Express, 2014. **22**(9): p. 11090-11098.

36. Frank, H.S. and M.W. Evans, *Free Volume and Entropy in Condensed Systems III. Entropy in Binary Liquid Mixtures; Partial Molal Entropy in Dilute Solutions; Structure and Thermodynamics in Aqueous Electrolytes.* The Journal of Chemical Physics, 1945. **13**(11): p. 507-532.

37. Dixit, S., et al., *Molecular segregation observed in a concentrated alcohol.* Nature, 2002. **416**: p. 829-832.

38. Soper, A.K. and J.L. Finney, *Hydration of methanol in aqueous solution.* Physical Review Letters, 1993. **71**(26): p. 4346-4349.

39. Liu, C., E. Bonaccurso, and H.-J. Butt, *Evaporation of sessile water/ethanol drops in a controlled environment.* Physical Chemistry Chemical Physics, 2008. **10**(47): p. 7150-7157.

40. Innocenzi, P., et al., *Evaporation of Ethanol and Ethanol−Water Mixtures Studied by Time-Resolved Infrared Spectroscopy.* The Journal of Physical Chemistry A, 2008. **112**(29): p. 6512-6516.

41. Kim, S., et al., *Room-temperature metastability of multilayer Graphene Oxide films.* Nat Mater, 2012. **11**(6): p. 544-549.

42. You, S., et al., *Effect of synthesis method on solvation and exfoliation of Graphite Oxide.* Carbon, 2013. **52**(0): p. 171-180.

CHAPTER 7: GRAPHENE OXIDE BASED OPTICAL SWITCH: MOTIVATION

Waveguide-based optical modulators and switches are essential devices in optical communications such as on chip optical signal processing, integrated optoelectronic circuit, network protection and as the fundamental building-blocks of optical logic gates [1-4]. The ability to achieve all-optical modulation has advantages in optical signal processing compared to electro-optic or acousto-optic modulation techniques. To date, many all-optical approaches have been reported, and these approaches have good modulation depth with high speed response [5-8], which are the two figure of merits for an optical modulator. Most, if not all modulators demonstrated have narrow operating bandwidth and require sophisticated design for broadband applications. An alternative approach towards broadband optical modulation is the use of materials possessing broadband response [9].

Graphene Photonics has become an important research field due to the unique characteristics of Graphene which extends to the optical frequencies [10, 11]. Graphene based devices such as broadband polarisers and modulators have been developed [10, 12-14]. The broadband frequency response of Graphene is a result of its universal fine structure constant in which its conductance is independent of frequency over a wide range [11-16]. Moreover, the strong light-Graphene interaction and high carrier mobility properties of Graphene are additional advantages for optical modulation applications [11-16]. Besides, GO has significant capability of self-heating through optical phonon excitation [17-20] as discussed in section 4.3.4. Thermally heated GOF will undergo a de-oxygenation reaction [17, 21-23]. However, this effect is reversible when the heat is removed, especially in a closed (sealed) environment [21, 24]. During the de-oxygenation

reaction, a remarkable increase in film conductivity and eventually larger optical absorption is observed [25-27]. This reversible phonon reduction phenomenon is the basic block of the proposed optical inverted switch to be discussed in this chapter.

The organization of this chapter begins with the discussion of optical switch design and fabrication. This is followed by optical characterization setup and performance characterization of the optical switch. Finally, an analysis on the performance of the proposed optical switch will be presented.

7.1 Fabrication and Optical Characterization Setup

The design of the GO based optical waveguide switch is similar to the GO waveguide polarizer discussed in chapter 5. A 6 µm thick BCB layer was spin-coated onto a silicon substrate as undercladding. A 3 x 3 µm SU-8 core was fabricated onto the BCB layer using fabrication steps discussed in chapter 3. The GOF coating was done by drop-casting. A total of 2 drops of 1 µg/µL GO solution were used. The first GO solution drop were allowed to dry before the application of the second drop directly on top of the first drop. The GOF was allowed to dry at room temperature for another thirty minutes before it was covered using optical resin (NOA 68) as overcladding. The overcladding was applied not only onto the GOF region, but the entire channel waveguide to avoid exposure of the channel waveguide to the external environment.

The optical characterization of the GO based optical switch was more complex as shown in Figure 7.1. High numerical aperture fibres (UHNA-4) were used for butt-coupling of light into the GO based waveguide switch. High numerical aperture fibres were used instead of ordinary SMF-28 fibre to minimise the coupling loss of the SU-8

waveguide as discussed in section 3.9. It is worth noting that a 3 x 3 µm SU-8 core size in this waveguides design can ensure single mode operation in the 1550 nm region. Two laser sources were used as control and signal. The control-laser was a Fabry-Perot laser diode operating at 1480 nm (Sumitomo SLA5600) while the signal-laser was a tunable laser source operating between 1530 - 1580 nm (LD - Santec ECL-210). A broadband 1550 nm superluminescent diode source (SLD - Acterna OBS-15) was also used as the signal source to measure the response bandwidth of the GO-coated waveguide in the 1550 nm wavelength band. Both control and signal sources were combined using a 1480/1550 Wavelength Division Multiplexer (WDM) device, while a second WDM device with the same filtering characteristic was used to separate the two laser wavelengths at the output for convenience of analysis. Polarisation Controllers (PC) were placed between the laser sources and the input of the WDM in order to allow control over the polarisation state of both laser sources before they were coupled into the GO-coated waveguide. It is worth noting that the WDM device did not have any polarisation-dependent loss. The output power levels at both wavelengths were analysed using an Optical Power Meter (OPM - ILX Lightwave OMM-6810B), while the spectrum of the output was measured using an Optical Spectrum Analyser (OSA - Yokogawa AQ6370). A Polarisation Analyser (Thorlabs PAN5710IR3) was used to analyse the polarisation state at both wavelengths and the modulation speed was measured using a fast photodetector (PD - Thorlabs DET-36).

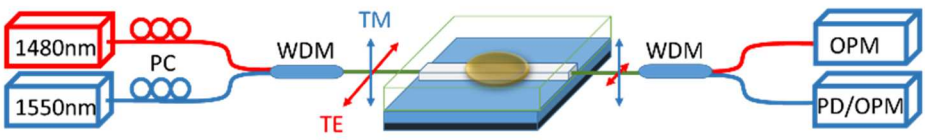

Figure 7.1: Experimental setup for optical modulation measurement.

To measure the temperature of the GOF when light is injected, a second GO-coated waveguide was fabricated with the GO-coated waveguide region left uncovered. A mini-hypodermic T-type thermocouple (HYP-0, Omega) was carefully placed at a distance of less than 1 mm from the GO-coated waveguide near the input end - and in physical contact with the GOF. A third optical waveguide without GO coating was also fabricated as a reference sample.

7.2 Performance of Proposed Optical Switch

Figure 7.2 shows the transmission characteristic of the 1550 nm Laser Diode (LD) output with TM-polarisation state through the GO-coated waveguide at different control-source power levels. The LD output is highly polarised and hence control of its polarisation state was straightforward using a PC. The 1480 nm control-source was operated in a continuous-wave mode and was TE-polarised, which was highly absorbed by the GO-coated waveguide. The measurement wavelength range was limited to 1525 – 1580 nm by the transmission window of the WDM used. It was observed that the attenuation of the LD spectrum increased as the control-source power level was increased. Attenuation of the LD spectrum was observed over the entire measured transmission spectrum from 1525 nm to 1580 nm, as the signal to noise ratio (SNR) of the 1550 nm signal was maintained, indicating a broadband response of the optical switch. When the reference sample (optical waveguide without GO coating) was tested, this effect was not observed. Instead, a small increase in power level was measured from the signal-source WDM output at high control-source power level due to the imperfection of the WDM filtering. To verify this effect, a broadband SLD with maximum power level at 1550 nm was used to replace the single wavelength LD in the same configuration (where the control source was launch in TE-mode and signal source launch in TM-mode). The result was shown in Figure 7.3 and similar phenomenon was observed. On the other hand, when

the polarisation of the control-source was changed from TE-mode to TM-mode, no suppression effect was observed. As TM-polarised light is less absorptive by the GOF, the two observations above indicate that the suppression effect is caused by the absorption of TE-polarised light by the GOF. In addition, when the polarisation of the signal-source was changed to TE-mode, the measured transmission was always low and the suppression effect, if any, was not observable.

The switching performance of the optical switch was next examined. The SLD was replaced with the single wavelength 1550 nm LD to provide a signal-source with higher polarisation extinction ratio and power stability. Figure 7.4 shows the time-dependent variation of the signal-source power level, measured using a photodiode. The control-source was modulated at three different frequencies, but at a fixed pulse duration of 100 μs, limited by the modulation bandwidth of the 1480 nm control-source laser diode. The control-source modulation starts at 0^{th} second. It can be seen that the optical switch was able to respond to the set optical pulse at these frequencies. For modulation frequency of 1 kHz, the pulse-to-pulse modulation depth was stable and no significant change to the maximum and minimum power levels were observed. When a higher modulation frequencies (4 kHz and 5 kHz) were used, a drop in the maximum power level was observed over time, and this power drop resulted in progressively lower modulation depth before it stabilised after about 2 ms.

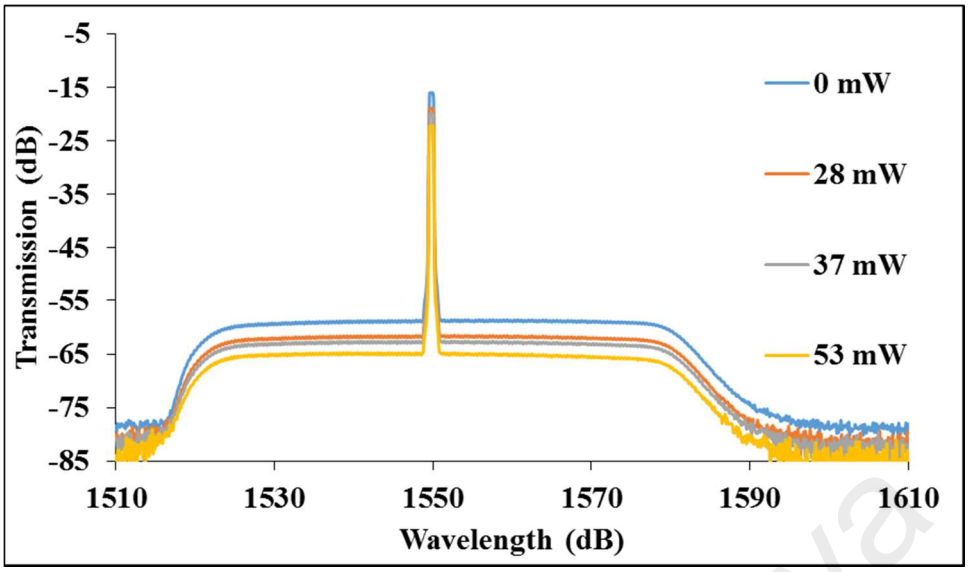

Figure 7.2: Broadband attenuation of the signal-source power by the GO optical switch at 1550 nm with different 1480 nm CW control-source power. Signal source was TM-polarised while control-source was TE-polarised.

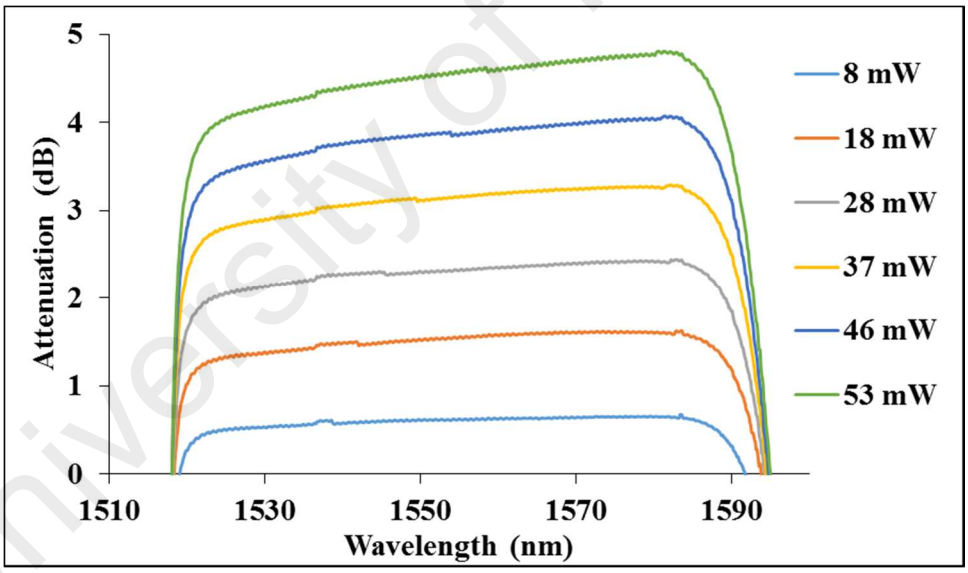

Figure 7.3: Broadband attenuation of 1550 nm broadband signal-source power by the GO optical switch with different 1480 nm CW control-source power.

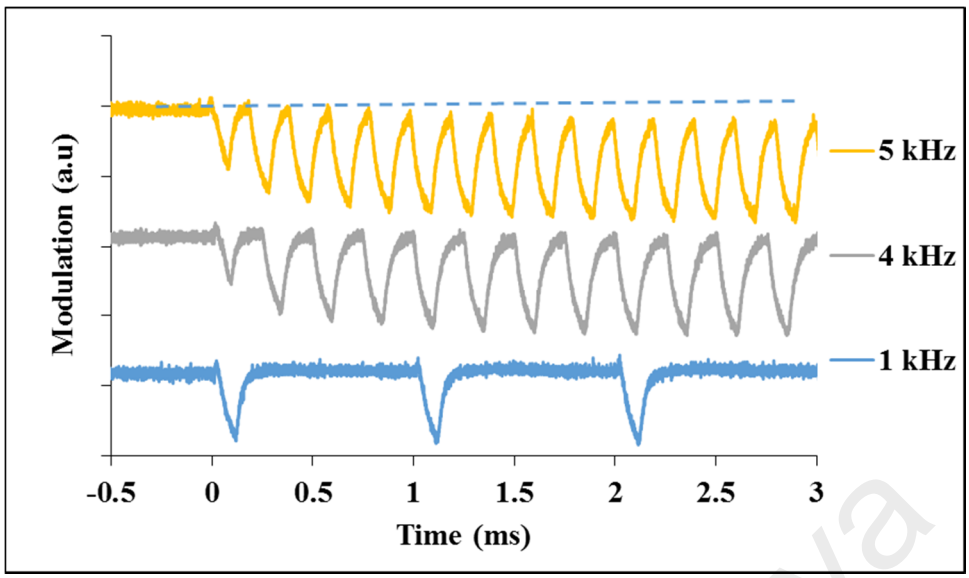

Figure 7.4: Modulation depth of the optical switch measured using a photodiode at 3 different modulation frequencies with fixed pulse duration of 100 µs. The trace for 4 kHz and 5 kHz was shifted up for ease of viewing.

The modulation efficiency was further studied by modulating the control-source at different frequencies, power levels and pulse durations. Figure 7.5 shows the modulation efficiency of the proposed optical switch at low modulation frequency (50 Hz) with the pulse duration varied over the range from 100 µs to 1000 µs. When modulated with short optical pulses, a slight increase in the modulation efficiency of the optical switch with control-source peak power was measured. The modulation efficiency was also relatively low, with a maximum efficiency of 15% when the control-source power level was set at 57 mW. As the pulse duration increased, so did the modulation efficiency. At the same time, the gradient of the modulation efficiency with the peak power level of the control-source also increased and saturated for pulse durations longer than 400 µs, though the overall modulation efficiency still increased with longer pulse duration. The optical switch shows a linear response to control-source power, indicating that the optical power suppression effect observed is not likely to be due to a non-linear effect in the GOF.

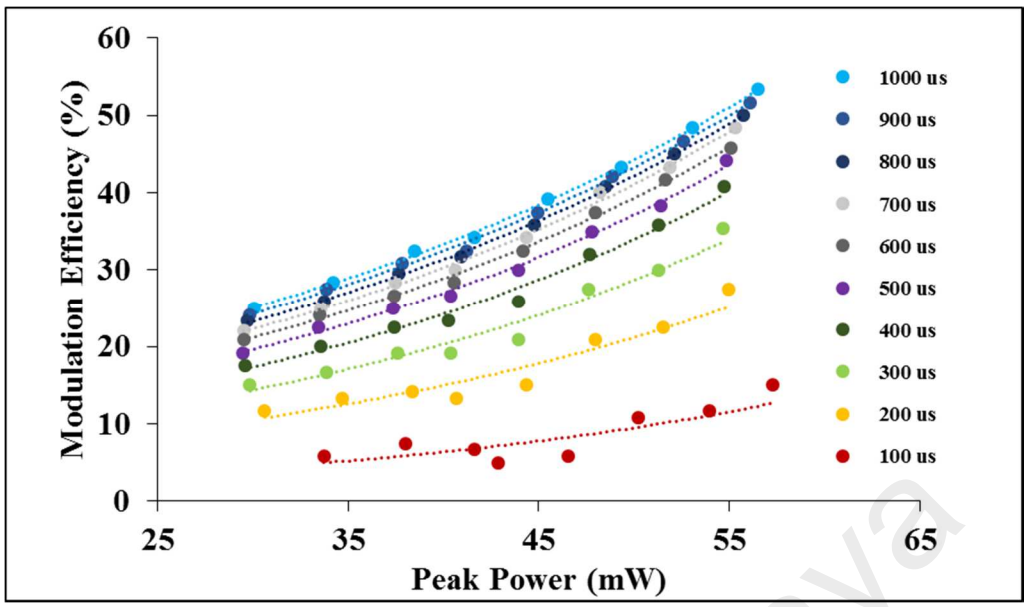

Figure 7.5: Modulation efficiency of the switch at various pulse durations, modulated at 50 Hz. The dotted line was included for easy viewing.

The performance of the optical switch was also studied at higher modulation rates. Figure 7.6 shows the modulation efficiency of the optical switch for modulation frequencies ranging from 0.5 kHz to 5 kHz, at a fixed duty cycle of 50%. The linear response of modulation efficiency to control-source power appears to be retained. However, while there is almost no difference in modulation efficiency for different modulation frequencies at low control-source power levels, modulation efficiency seems to be frequency dependent when higher control-source power were used. Lower modulation efficiency was observed for higher modulation frequency. This result led us to suspect that the suppression mechanism is caused by thermal effects in the multilayer GOF.

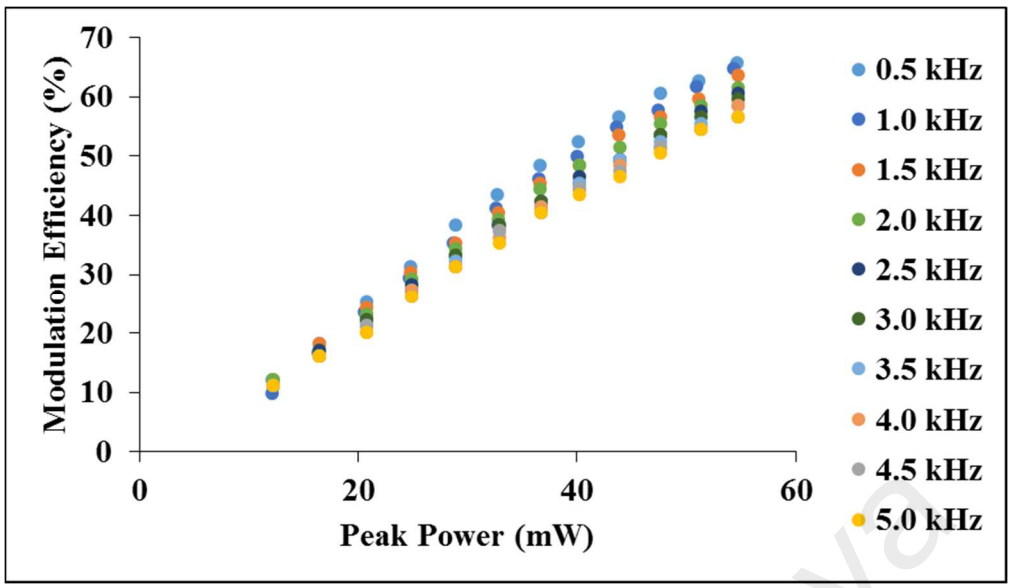

Figure 7.6: Modulation efficiency of the proposed switch for modulation frequency in the range from 0.5 kHz to 5 kHz with fixed 50% duty cycle.

To verify the above hypothesis, the variation in the modulation efficiency of the optical switch with the Continuous Wave (CW) control-source power level was measured and the result is shown in Figure 7.7. A modulation efficiency of 72% (limited by the maximum control-source power level) has been achieved with 57 mW of control-source power and a 1 mW signal-source power level. It is worth noting that the modulation efficiency is independent of the signal-source power level (signal-source power was varied between 0.3 - 1 mW). At the same time, the temperature of the GOF in a GO-coated waveguide without top cover was measured during control-source power injection. The temperature change for a varying control-source power level was also plotted in Figure 7.7. The temperature of the GOF increased linearly with increasing control-source power, with a maximum change of 3 ^{o}C when CW control-source power was set at 57 mW. The measured temperature profile shares the same trend with the modulation efficiency. A relatively fast change in the GOF temperature was observed when the control-source source power was varied. It is expected that the absolute temperature of the GOF in contact with the SU-8 waveguides is much higher compared to the measured

temperature due to heat dissipation and temperature probe position from the waveguide channel (kept at less than 1 mm from the waveguide channel, which is still a large distance compared to the width of the waveguide channel of 3 μm).

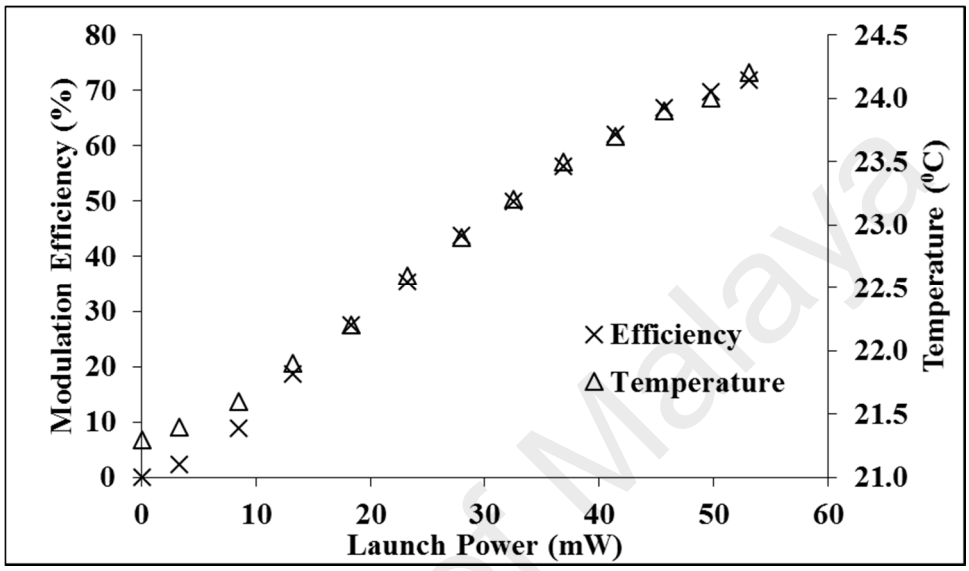

Figure 7.7: Modulation efficiency and GOF temperature at various control laser power.

Carbonaceous materials have significant capability of self-heating through optical phonon excitation [17-20]. Guo [21] has shown that a 1 μm thick GOF can undergo a significant increase in temperature (> 40 ^{o}C difference compared to a bare substrate without GOF) when exposed to a low power broad band IR light source (with an emission spectrum covering the range from 1000 to 1700 nm). Thermally heated GOFs will undergo de-oxygenation reaction and the GOF will therefore be substantially reduced [17, 21-23]. It is worth noting that the thermal stability of the oxygen functional groups can be ranked in the order of epoxide < carbonyl < hydroxyl [28]. A reduced-GOF, therefore, has a remarkably higher conductivity and consequently results in a larger optical absorption [25-27]. In our optical switch, the control-laser was launched in TE-mode which was then strongly absorbed by the GOF, creating a photo-thermal effect. The heated GO-film then has a greater attenuation at the signal-laser source wavelength and

eventually a suppression effect is induced. Thermally reduced-GOF is unstable and it can easily be oxidised back to its initial state [21, 24]. This re-oxidation is especially apparent in the present optical switch configuration, where the GOF was shielded by the NOA overcladding. The oxygen molecules that were released during the photo-thermal process cannot escape and will eventually bond back into the GO layers, causing reversible changes in the suppressive effect when the control-source was switched off.

This suppression phenomenon was not observed when light from the control-source was launched in TM–mode, due to the fact that the absorption cross-section of GOFs for light polarised in TM-mode is much lower compared with that of TE–mode and hence photo-thermal effect is less significant. Similar reasoning applies for signal-source light that was launched in TM–mode, which has no significant effect on suppression. It is worth noting that the control-source can be in other wavelength due to the broadband response characteristic of GO. For example, when a 980 nm light source was used as the control signal, similar observation was obtained (suppression effect with ~100 μs response time), but the modulation depth was much lower.

The difference in the modulation efficiency is due to the change in interaction cross section of the GOF with its thickness. The GOF in the optical switch itself can be considered as another waveguide core, the amount of light guided in the GOF will depend on the GOF thickness as well as the wavelength. For example, 980 nm control-source has lower coupling ratio and eventually lessen the suppression effect as shown in Figure 7.8. In a separate test, we swapped the polarisation states of the control- and signal-source, where 1550 nm act as control-source. Similar suppression phenomenon with almost equal response time was observed on the 1480 nm signal-source, with the modulation efficiency obtained limited by the peak power of the 1550 nm laser diode of 3.7 mW. The

wavelength-independent response time obtained is due to the photo-thermal effect. As long as the environmental condition of the GOFs remained unaltered, the response and relaxation time of the GOF should remain.

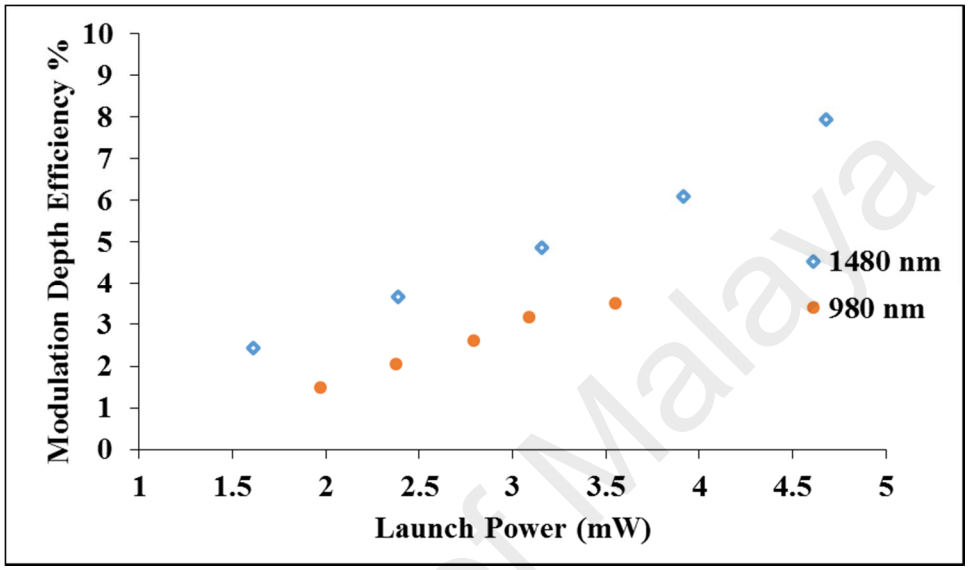

Figure 7.8: Modulation efficiency of the GO switch with 1480 nm and 980 nm control source.

7.3 Conclusion

An inverted optical switch was designed and fabricated. An inverted modulation depth of 72% (limited by the maximum modulation power level) has been measured between 1520 and 1590 nm (limited by the available wavelength range of the probe source). The modulation effect is due to reversible photothermal reduction of GOF with the thermal energy generated by strong TE-polarised light absorption in the GOF. The response time of 100 μs is limited by the heat dissipation rate of the GO-coated waveguide. The results obtained indicate that GO-coated waveguide has great potential to be used as an all optical waveguide modulator and as a basic building block of optical logic gate.

References

1. Della Corte, F.G., et al., *Electro-optical modulation at 1550 nm in an as-deposited hydrogenated amorphous silicon p-i-n waveguiding device.* Optics Express, 2011. **19**(4): p. 2941-2951.

2. Reed, G.T., et al., *Silicon optical modulators.* Nat Photon, 2010. **4**(8): p. 518-526.

3. Li, Q., et al., *Optical logic gates based on electro-optic modulation with Sagnac interferometer.* Applied Optics, 2014. **53**(21): p. 4708-4715.

4. Jeong, J.M. and M.E. Marhic, *All-optical logic gates based on cross-phase modulation in a nonlinear fiber interferometer.* Optics Communications, 1991. **85**(5–6): p. 430-436.

5. Heber, A., M. Selmke, and F. Cichos, *Metal Nanoparticle Based All-Optical Photothermal Light Modulator.* ACS Nano, 2014. **8**(2): p. 1893-1898.

6. Wu, C.-L., S.-P. Su, and G.-R. Lin, *All-optical modulation based on silicon quantum dot doped SiOx:Si-QD waveguide.* Laser & Photonics Reviews, 2014. **8**(5): p. 766-776.

7. Takeda, H., *All-optical modulation and amplification resulting from population inversion in two-level systems using a photonic-crystal cavity.* Physical Review A, 2012. **86**(1): p. 013803.

8. Venkataraman, V., et al., *Few-Photon All-Optical Modulation in a Photonic Band-Gap Fiber.* Physical Review Letters, 2011. **107**(19): p. 193902.

9. Narayanan, K., A.W. Elshaari, and S.F. Preble, *Broadband all-optical modulation in hydrogenated-amorphous silicon waveguides.* Optics Express, 2010. **18**(10): p. 9809-9814.

10. Bao, Q., et al., *Broadband Graphene polarizer.* Nature Photon., 2011. **5**: p. 411.

11. Bao, Q. and K.P. Loh, *Graphene Photonics, Plasmonics, and Broadband Optoelectronic Devices.* ACS Nano, 2012. **6**(5): p. 3677-3694.

12. Liu, M., et al., *A Graphene-based broadband optical modulator.* Nature, 2011. **474**: p. 64.

13. Hao, R., et al., *Ultra-compact optical modulator by Graphene induced electro-refraction effect.* Applied Physics Letters, 2013. **103**(6): p. -.

14. Yang, L., et al., *Ultracompact optical modulator based on Graphene-silica metamaterial.* Optics Letters, 2014. **39**(7): p. 1909-1912.

15. Liu, Z.-B., et al., *Broadband all-optical modulation using a Graphene-covered-microfiber.* Laser Physics Letters, 2013. **10**(6): p. 065901.

16. Li, W., et al., *Ultrafast All-Optical Graphene Modulator.* Nano Letters, 2014. **14**(2): p. 955-959.

17. Cote, L.J., R. Cruz-Silva, and J. Huang, *Flash Reduction and Patterning of Graphite Oxide and Its Polymer Composite.* Journal of the American Chemical Society, 2009. **131**(31): p. 11027-11032.

18. Pop, E., et al., *Negative Differential Conductance and Hot Phonons in Suspended Nanotube Molecular Wires.* Physical Review Letters, 2005. **95**(15): p. 155505.

19. Begtrup, G.E., et al., *Probing Nanoscale Solids at Thermal Extremes.* Physical Review Letters, 2007. **99**(15): p. 155901.

20. Mohammed, O.F., P.C. Samartzis, and A.H. Zewail, *Heating and Cooling Dynamics of Carbon Nanotubes Observed by Temperature-Jump Spectroscopy and Electron Microscopy.* Journal of the American Chemical Society, 2009. **131**(44): p. 16010-16011.

21. Guo, H., et al., *Preparation of reduced Graphene Oxide by infrared irradiation induced photothermal reduction.* Nanoscale, 2013. **5**(19): p. 9040-9048.

22. Acik, M., et al., *Unusual infrared-absorption mechanism in thermally reduced Graphene Oxide.* Nat Mater, 2010. **9**(10): p. 840-845.

23. Acik, M., et al., *The Role of Intercalated Water in Multilayered Graphene Oxide.* ACS Nano, 2010. **4**(10): p. 5861-5868.

24. Ryu, S., et al., *Atmospheric Oxygen Binding and Hole Doping in Deformed Graphene on a SiO2 Substrate.* Nano Letters, 2010. **10**(12): p. 4944-4951.

25. Jung, I., et al., *Effect of Water Vapor on Electrical Properties of Individual Reduced Graphene Oxide Sheets.* The Journal of Physical Chemistry C, 2008. **112**(51): p. 20264-20268.

26. Yavari, F., et al., *Tunable Bandgap in Graphene by the Controlled Adsorption of Water Molecules.* Small, 2010. **6**(22): p. 2535-2538.

27. Lipatov, A., et al., *Highly selective gas sensor arrays based on thermally reduced Graphene Oxide.* Nanoscale, 2013. **5**(12): p. 5426-5434.

28. Wang, D.-W., et al., *A water-dielectric capacitor using hydrated Graphene Oxide film.* Journal of Materials Chemistry, 2012. **22**(39): p. 21085-21091.

CHAPTER 8: THESIS CONCLUSION AND FUTURE WORK

There are several achievements made during the course of this research study. The successful coating of GOF onto planar waveguide using drop-casting technique became the foundation for the rest of the works. Broadband (from 1530 nm to 1630 nm) polarization dependent loss of > 30 dB was achieved in a GO-coated optical waveguide channel using GO drop-casting. The polarisation effect is attributed to the anisotropic dielectric properties of GOF which is related to its stacking structure. The regular stacking of GO was created due to the GO droplet drying mechanism. As a result, GOWP was successfully demonstrated using this concept. Besides, the unique characteristic stacking structure of GOF also leads to high water molecule permeation. This property has enabled water and humidity sensing with just a minor change in the initial GOWP design. In-situ water sensing capability and humidity sensing in the range of 60% RH to 100% RH was demonstrated. The sensing mechanism is due to the change of GOF dielectric property when the water content within the GOF was varied. Last but not least, the GOWP can be used as an active inverted optical switch due to the photo-thermal reduction effect of GOF. Modulation depth as high as 72% with 100 μs modulation speed was achieved.

Although the versatility of GOF in photonics applications was demonstrated, a number of improvements should be conducted to realise its potentials. However, these improvements were not carried out in the current study due to time limitation, instrument constraint and the need for a more comprehensive material study, which will cause deviation from the objectives of the current work. Instead, these improvements were discussed in following section as future works.

Waveguide Structure

As discussed in chapter 5, air void was consistently created during the GO drop-casting due to its drying mechanism. However, the size of the air void is difficult to control. When smaller waveguide core was used, smaller air void will be created, which may enable light coupling to GOF adjacent to the sidewall of the waveguide channel, across the air void. This will increase the device insertion loss due to the increase propagation loss in TM-mode. To overcome this problem, embedded or strip waveguide instead of rib waveguide can be used. An embedded waveguide means only the top surface of the core is exposed to air during fabrication and hence the GOF will not cover the side of the channel during drop-casting.

Graphene Oxide Coating

There are two issues with the current GOF drop-casting technique. Wrinkles formation and flexibility in thickness control. First of all, wrinkle is unavoidable using the current coating technique, while the thickness gain of the GOF is "discrete" for a given concentration. As mentioned in chapter 4, wrinkling can be improved by adding alcohol to reduce the surface tension of the droplet solution and its contact angle. However, reducing the contact angle also enlarges the GO coating area. To achieve smaller coating area, more precise and advance control system in solution droplet volume is required; currently the smallest droplet size is limited to 1 μl with a mechanical micro-pipette. The advance system not only need to dispense solution in the nano-liter range, it also needs to have an imaging system for precise dispensing onto the waveguide (essentially, an automated GO solution dispensing system). Moreover, with smaller dispensing volume, thinner GOF can be achieved and will eventually lead to better control of the GOF thickness.

Comprehensive Study on Graphene Oxide Film

As mentioned in chapter 7, GOF suffers from aging effect, where the film lost its hydrophilic characteristic over time. To date, the aging phenomenon is still being studied. Kim et al. state that the aging effect is a natural metastable characteristic of GO [1]. When comparing their results with ours, their GOF seems to have a longer aging (or relaxation) time of about 1 month. When the GO preparation method was compared, it was observed that there are some differences such as oxidation time, preparation temperature, and the oxidation agent used. Hence, a deeper material study to understand the aging effect and then to stabilise or prolong the C = O decompose time is required.

Towards Optical Circuit

GOWP, water and humidity sensing and modulator/switch are a few of many basic building blocks for optical circuit for advance application. For example, optical logic gate can be achieved by expanding the modulator design with Y-branch and directional coupler. An example of a NAND gate is shown in Figure 8.1. The signal (i.e. 1550 nm) was launched in continuously at both input 1 and 2 in TM-polarized mode. The control (i.e. 1480 nm) was launched in TE-polarized mode with modulation. On the output port, a polarization filter is used to filter the control TE-polarized mode and allow only TM-polarized light to pass through. When both of the control inputs are “off”, the signal on both arms were allowed to transmit and hence the output is in “on” state. When either 1 of the control signal is in “on”, the signal in the arm where the control signal is “on” will be suppressed, while the signal on the other arm, in which the control signal is “off”, will be transmitted. As a result, the output will remained “on”. The output will only be in “off” state when both the control signal is in “on” stage. This operation is essentially a NAND structure.

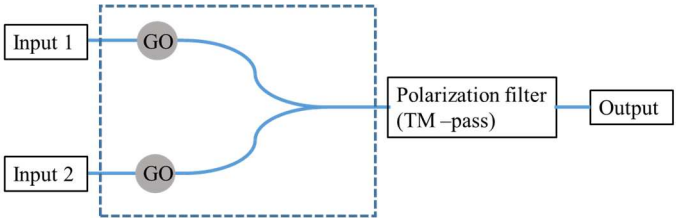

Input 1	Input 2	Output
1	1	0
1	0	1
0	1	1
0	0	1

Figure 8.1: Optical NAND gate design based on GO switch principle.

References

1. Kim, S., et al., *Room-temperature metastability of multilayer Graphene Oxide films.* Nat Mater, 2012. **11**(6): p. 544-549.

LIST OF PUBLICATIONS AND PAPERS PRESENTED

Journal Publication From This Study

Published Journal paper

1. Lim, W.H., Y.K. Yap, W.Y. Chong, C.H. Pua, N.M. Huang, R.M. De La Rue, and H. Ahmad, *Graphene Oxide-based waveguide polariser: From thin film to quasi-bulk.* Optics Express, 2014. **22**(9): p. 11090-11098.

2. Lim, W.H., Y.K. Yap, W.Y. Chong, and H. Ahmad, *All-Optical Graphene Oxide Humidity Sensors.* Sensors, 2014. **14**(12): p. 24329-24337.

Accepted Conference Paper and Poster

1. Lim, W.H., Y.K. Yap, W.Y. Chong, and H. Ahmad, *Graphene Oxide Coated Optical Waveguide for Humidity Sensing.* In 4th International Conference on Mutifunctional, Hybrid nanomaterials, Spain on 2015.

2. De la Rue, R.M., W.H. Lim, Y.K. Yap, W.Y. Chong, C.H. Pua, N.M. Huang, and H. Ahmad. *Graphene Oxide multilayer structures for polarisation selection and other functionalities in planar waveguide based integrated photonics*. in *Transparent Optical Networks (ICTON), 2014 16th International Conference on*. 2014.

Submitted under review

1. W.Y. Chong, W.H. Lim, R. M. De La Rue and H. Ahmad, *Photo-induced reduction of Graphene Oxide coating on optical waveguide and consequent optical intermodulation.*

Other Publications

1. Kam, W., Y.S. Ong, W.H. Lim, and R. Zakaria, *Laser ablation and waveguide fabrication using CR39 polymer.* Optics and Lasers in Engineering, 2014. **55**(0): p. 1-4.

2. H.Z. Yang, K.S. Lim, X.G. Qian,W.Y. Chong, Y.K. Cheong, W.H. Lim, W.S. Lim, and H. Ahmad, *Reflection spectra of etched FBGs under the influence of axial contraction and stress-induced index change.* Optic Express, 2013. **21**(12):14808-14815.

3. Yahya, N.A.M., W.H. Lim, K.D. Dambul, S.W. Phang, H. Ahmad, R. Zakaria, and F.R. Mahamd Adikan, *Fabrication and characterization of a dual layer multiple refractive index benzocyclobutene polymer platform for integrated optical devices.* Optical Materials, 2012. **34**(11): p. 1735-1741.

4. Chong, W.Y., K.S. Lim, W.H. Lim, S.W. Harun, F.R.M. Adikan, and H. Ahmad, *Spreading profile of evaporative liquid drops in thin porous layer.* Physical Review E, 2012. **85**(1): p. 016314.

5. Cheong, Y.K., K.S. Lim, W.H. Lim, W.Y. Chong, R. Zakaria, and H. Ahmad, *Note: Fabrication of tapered fibre tip using mechanical polishing method.* Review of Scientific Instruments, 2011. **82**(8): p.

APPENDIX A: LASER DIRECT WRITING

Waveguide channel definition or patterning is important in PLC design and fabrication because the pattern of a waveguide defines the function of the circuit. In chapter 3, an established patterning method, photolithography was discussed. Photolithography is a common and developed technique used in the semiconductor industry for mass production due to its high repeatability. However, this technique is not suitable for research purposes and proof of concept applications. This is because conventional photolithography method involves expensive and high operating cost tools. Besides, a photomask is needed for the pattern transfer in photolithography. The photomask pattern design is fixed and new design would require fabrication of a new photomask which is both expensive and time consuming for the "design-fabricate-characterize" cycle typical in optical waveguide research. On the other hand, direct writing of optical waveguide without the need of a photomask provides very high flexibility in the fabrication of optical waveguide functions with different circuit designs and a very low cost per design. The only drawback of direct writing method is the low throughput in mass production and the quality of the fabricated circuits may not perform as well as photolithographically fabricated samples [1-5].

The principle of direct writing is simple. Basically, it shares the same principle as drawing the circuit design on a paper with a pen. In most direct writing configurations, it is usually the "paper" that is moving while the "pen" is hold in a fixed position. In laser direct writing, the pen is replaced by a focused laser beam, while the paper is replaced by a layer of photosensitive waveguide material. When this "pen" writes, the light source will stamp its "footprint" on the "paper" - waveguide material. This footprint usually refers to changes in the material properties. This effect is dependent on the waveguide materials used and the wavelength of the light source. In a typical laser direct writing

process, optical mirrors and lenses are used to route and focus the laser beam. The waveguide layer is placed on a translation stage and the focused laser beam is focused into this layer. A computer controlled multi-axis stage is used to control the translation of the waveguide layer with reference to the optical design.

Direct laser writing is not a new technique, it has been commercially used in photomask fabrication via e-beam direct writing. In this case, the “pen” is electron beam and the “paper” is photoresists. E-beam writing has very high resolution, but it suffers from long production time. Besides, vacuum system is required which results in a more complex and expensive system. In silica glass direct waveguide writing, the “pen” can be either a UV laser light source or femtosecond laser source. These laser light will induce a positive refractive index change in the silica glass being irradiated and eventually forms a waveguide channel [3-5]. However, both methods also suffer from their own shortages. UV laser required the sample to be photosensitive while femtosecond laser writing usually formed a non-uniform channel due to it being an ablation process [6, 7]. Both methods also require high start-up and maintenance cost of bulk laser.

Another type laser direct writing, which was used in this work, is polymer based laser direct writing. The polymer material itself is UV photosensitive. A UV laser is used to create polymer cross-linked in this photosensitive layer. This layer will then undergo chemical etching (usually known as developing) to remove those un-cross-linked (UV un-irradiated) area. The advantages of this technique is that it does not require customized photosensitive polymeric materials. Instead, normal commercially available UV photoresists are sufficient. The limitation of this technique is that it is more suitable to work with negative tone photoresists [8].

System Setup

In Photonics Research Center, UM, we have developed a laser direct writing system as shown in Figure A.1. The system consists of several modifications over conventional laser direct writing setup that are more user-friendly. In general, it consists of a 405 nm laser diode source, Suruga 6-axis stepper motor stage, real time monitoring CCD camera (DC1545 CNOS with 50x magnification), and a self-developed translation program based on LabVIEW. The major part of the direct writing system is covered with a plastic Perspex box which is tinted with yellow paper to avoid sample exposure to ambient UV light from fluorescent lamps and sunlight. The system is placed in a class 100k clean room to reduce particle contamination. The advantages of the system are discussed in detail in the following subsections.

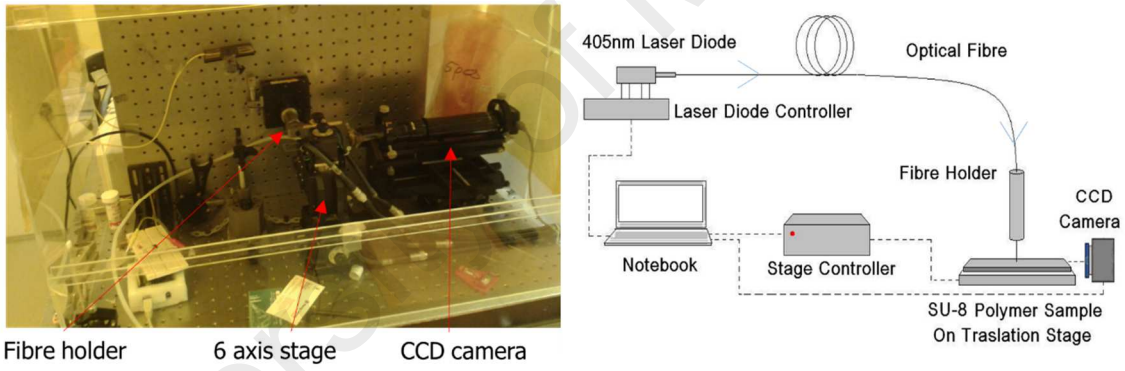

a) b)

Figure A.1: a) Photo and b) schematic diagram of all-fibre laser direct writing system.

405 nm Blue Laser and All Fibre Delivering System

There are 2 wavelength choices of semiconductor laser commercially available, which are 375 nm and 405 nm. It is worth noting that they are no distinct boundary between blue and UV light, but the light source above 400 nm is classified as blue. At the beginning setup stage of this writing system back in 2008, only 405 nm blue laser diodes are commercially available in the market - QPhotonics (QLD-405-20s) with 20 mW single mode fibre output, and mode field diameter of 3.6 μm. Besides, we adopted the

full fibre delivery method instead of free-space beam steering in traditional writing system. A single mode fibre coupled laser diode output can ensure a good Gaussian mode profile with stable power distribution. We then coupled the fibre into SM-300SC fibre which can further reduce the mode field diameter to about 2.5 μm which is perfectly matched with the width required for medium index contrast waveguide. Further laser beam focusing and spatial filtering are not required. The laser beam size is controlled by adjusting the distance between the fibre tip and the sample and do not require additional lenses for magnification.

Choices of Polymer

Most of the commercial available I-line photoresists has absorption spectrum as shown in Figure A.2 (taken from ref [9]). This is because the polymer itself is not photosensitive, which mean that it do not have any response to UV light to make any cross-link or decomposition reaction. However, by adding photoacid generator into these polymers, photoacid will be released when the polymers are irradiated with UV light. The photoacid then acts as catalyst in the polymer for crosslinking reaction. In SU-8, the photoacid generator used is Triaryl-sulfonium salt, which is a common photoacid generator in most of the I-line photoresists. As a result, most of the I-line photoresists shared the same UV absorption spectrum [9-11].

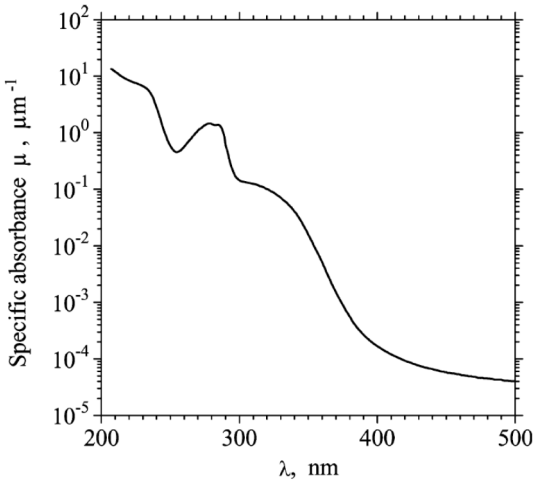

Figure A.2: Specific absorbance of SU-8. [9]

Although 405 nm is not located at the polymer peak absorption (about 1/20 times less absorption compared to I-line at 365 nm), this can be compensated by using higher laser intensity during the writing process. The energy required for polymerization is measured in terms of fluence which is a product of intensity and exposure time. Which means that besides controlling the laser power, we also can control the exposure time to obtain fluence that exceed its minimum threshold for polymerization.

Real Time Monitoring Control

Spin coating is a developed technique to ensure large area uniform coating onto a substrate. However, the substrate itself may have bowing effect – the centre is slightly higher/lower than the edge. Therefore, before each writing process, the tilt and pitch of the sample need to be aligned so that any part of the sample would not touch the fibre tip. Scratching of the fibre tip on the sample surface during a writing process may contaminate the tip and affect the laser output profile, which will affect the remaining writing process. To avoid this, a real time monitoring CCD camera, placed perpendicular to the fibre tip and sample surface, was used. An example of the CCD image is shown in Figure A.3. During alignment, we observe the image of the fibre tip (on top) does not touch or scratch

on the sample (the bottom). Besides, by measuring the gap size (calibrated using the vertical axis of Sugura motor), the spacing between the fibre tip and sample surface can be estimated. This estimation is useful to determine the expansion of the laser beam in which it has a direct effect on the written channel width.

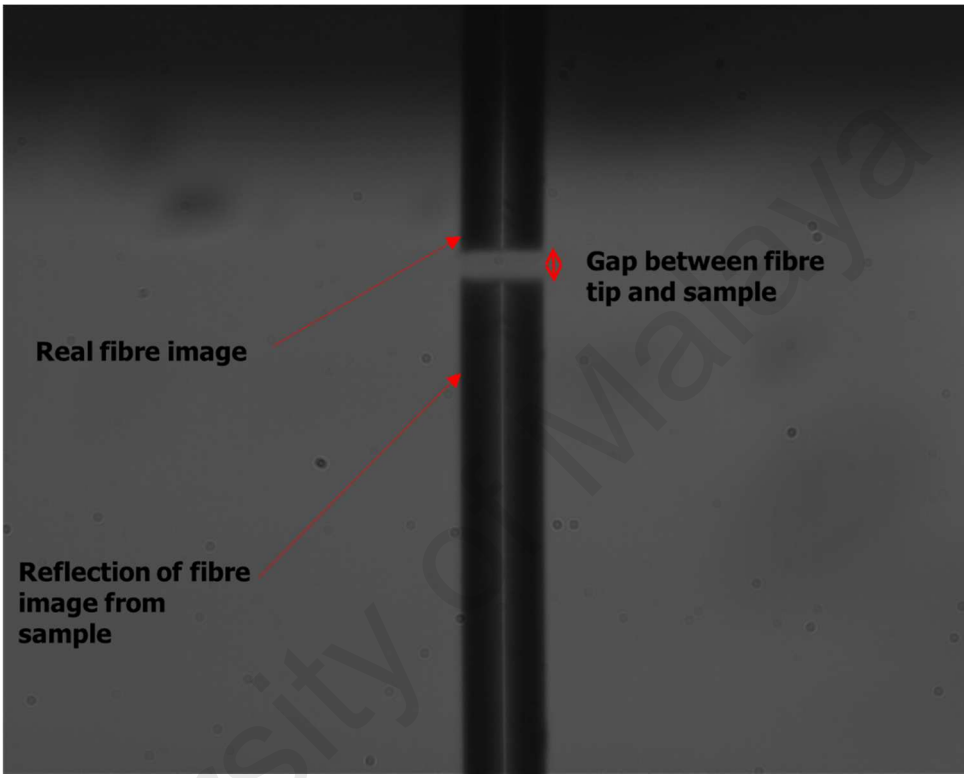

Figure A.3: Real time CCD image of the direct writing system.

LabVIEW Stage Motion Control

The motion of the Suruga stage is fully controlled by a LabVIEW program. It takes some time to develop this program due to the microsecond delay in command transmission between the computer - Sugura controller and the stepper motor. In the most direct control (absolute position method), subsequent command line will only be sent to the Sugura stepper motor followed by the stepper motor after the stepper motor has completed its current translation command where the motor already reached the given coordinate. This method gives very high accuracy in positioning. However, the data querying and command time is in the microsecond range. Having laser exposure on a same point for

an extra few microseconds will create larger width (exposure area) as shown in Figure A.4a. This “dot” is detrimental to the waveguide characteristics. As a result, a second method was used - time variation. Instead of instructing the motor to move to an absolute position, the LabVIEW will instead query from the motor on its speed without telling it the position to stop. The stepper will travel until the LabVIEW program send out a “stop” command. The delay in command transmission in this case is smaller and the “dot” issue were not observable. The disadvantage using this method is position mismatch, especially in Y-branch and directional coupler design as shown in Figure A.4b. However, since the LabVIEW program has the full control of time, subsequent command can be sent to the Suruga controller before it reaches the desired position. As a result, the next command will reach the stepper motor exactly when the motor completed the current travelling. In other words, position mismatch can be compensated by controlling the timing of sending subsequent command to the controller. Figure A.4c shows a good overlapped Y-branch waveguide written using the time-variation method with timing offset.

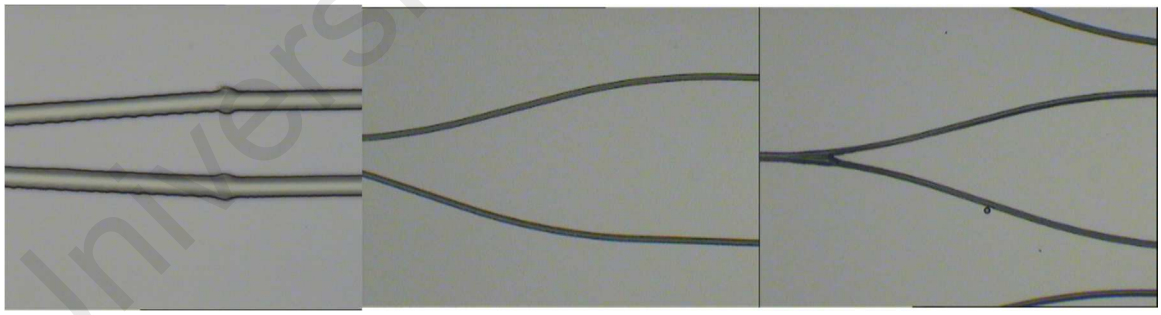

a) b) c)

Figure A.4: Some example of direct written waveguide.

A Comparison Between Photolithographically and Direct Written Waveguide

The direct written waveguide has poorer waveguide profile. A perfect square profile can be achieved via photolithography technique, while in direct laser writing, the cross section profile was rounded at the edges. Besides, occasionally there is some unknown vibration in the writing stage, which maybe due to resonance frequency or stepper motor vibration. As a result, jagged line is sometimes obtained as shown in Figure A.5. As a result, the optical propagation loss for direct writing waveguide is usually higher by up to 1 dB as compared to photolithographically patterned waveguide using the optimum process parameters.

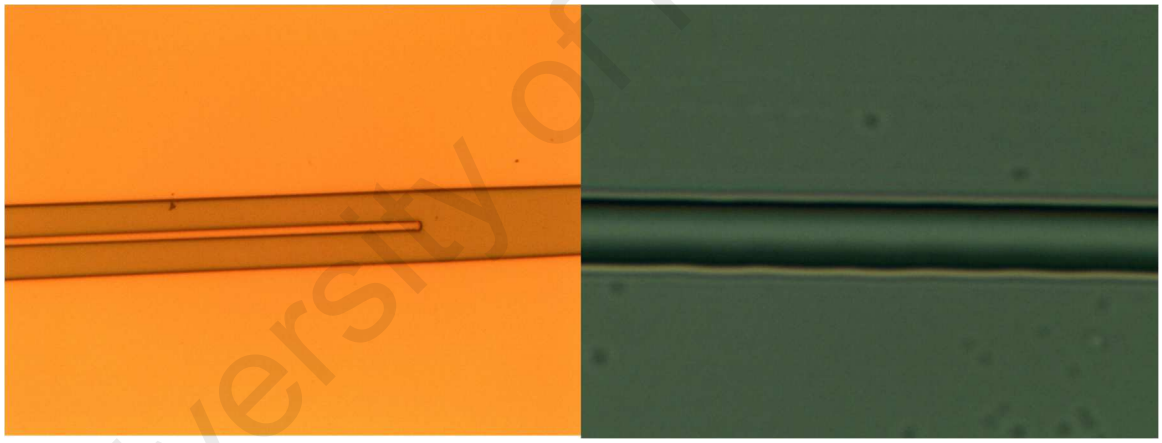

a) b)

Figure A.5: a) Photolithographically waveguide and b) direct written waveguides. Jagged occurred in direct written waveguide.

The repeatability of the writing is also relatively poor. For example, when the same pattern is repeated on the same substrate using the same laser fluence and writing program, the gap between the first and last directional coupler can be varied by up to 0.5 μm. The cause of low repeatability on a same substrate is due to the relatively slow writing speed (300 μm/min). During the course of writing process, the “freshness” of the

photoresists film when the first circuits is written compared to the last circuits is written will change – due to the relatively long duration for the whole writing process to be completed.

Most of the time in this work, direct laser writing was used to fabricate the photomask, which will then be used to produce SU-8 waveguides using photolithography method. It was found that the fabrication of photomask using laser direct writing is easier as the photoresist layer thickness required (AZ 1512) only about 1 μm (less than half the thickness of SU-8 waveguide).

References

1. Pearson, M., *FTTx Technologies: Planar Lightwave Circuits Revolutionize photonics.*, in *Laser Focus World*. 2007.

2. Calvo, M.L. and V. Lakshminarayanan, *Optical Waveguides:From Theory to Applied Technologies*. 2007, Boca Raton: CRC Press Taylor & Francis Group.

3. Olivero, M., et al., *Direct UV Writing speeds up the exploitation of integrated optics in stellar interferometry.* SPIE Newsroom, 2006.

4. Olivero, M. and M. Svalgaard, *UV-written Integrated Optical 1xN Splitters.* Optics Express, 2006. **14**(1): p. 162-170.

5. Olivero, M. and M. Svalgaard, *Direct UV-written broadband directional planar waveguide couplers.* Optics Express, 2005. **13**(21): p. 8390-8399.

6. Fernandes, L.A., et al., *Femtosecond laser writing of waveguide retarders in fused silica for polarization control in optical circuits.* Optics Express, 2011. **19**(19): p. 18294-18301.

7. Gattass, R.R. and E. Mazur, *Femtosecond laser micromachining in transparent materials.* Nat Photon, 2008. **2**(4): p. 219-225.

8. Wang, S., V. Vaidyanathan, and B. Borden, *Polymer optical channel waveguide components fabricated by using a laser-direct writing system.* Journal of Applied Science & Engineering Technology, 2009. **3**: p. 47-52.

9. Reznikova, E.F., J. Mohr, and H. Hein, *Deep photo-lithography characterization of SU-8 resist layers.* Microsystem Technologies, 2005. **11**(4-5): p. 282-291.

10. Stephan, K., et al., *Processing of thin SU-8 films.* Journal of Micromechanics and Microengineering, 2008. **18**(12): p. 125020.

11. *SU-8 2002 Processing Guides*. MicroChem: MicroChem, http://www.microchem.com/pdf/SU-82000DataSheet2000_5thru2015Ver4.pdf.